Search for Higgs Bosons using the L3 Detector at LEP

Andreas Kopp

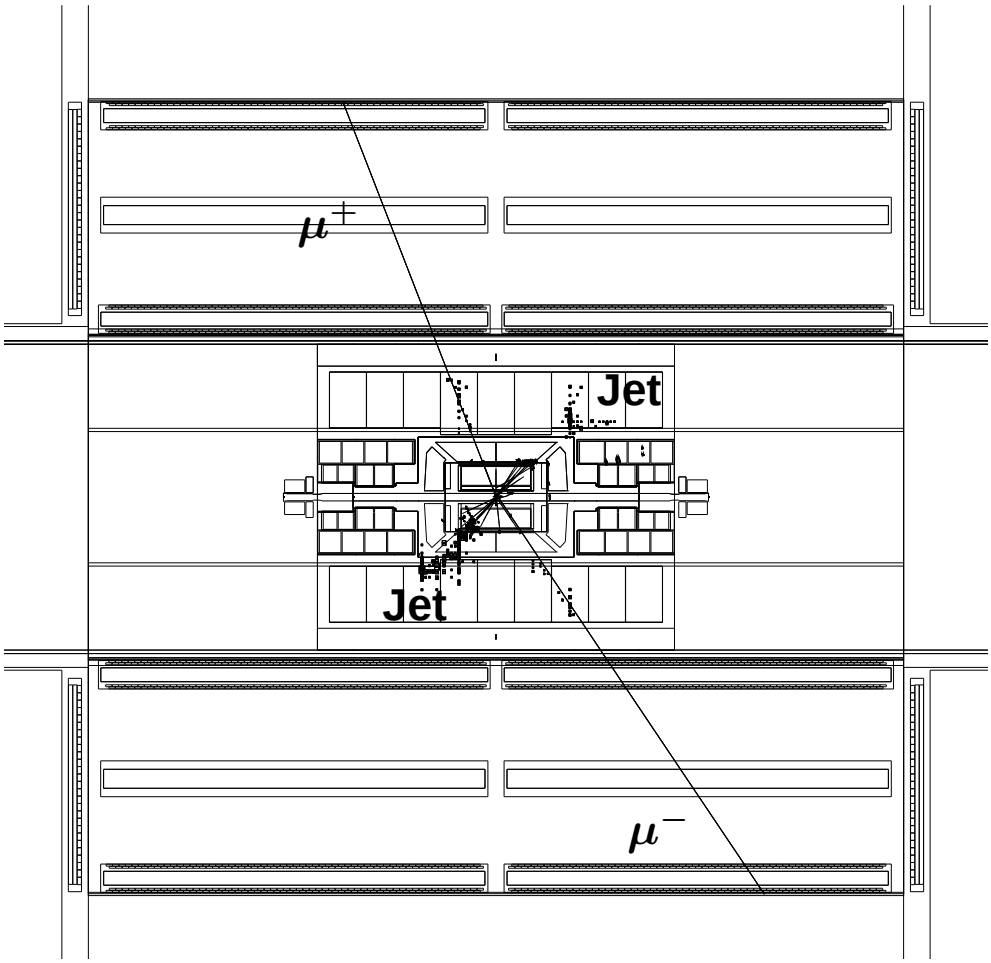

Search for Higgs Bosons using the L3 Detector at LEP

D i s s e r t a t i o n

zur Erlangung des akademischen Grades

d o c t o r r e r u m n a t u r a l i u m

(Dr. rer. nat.)

im Fach Physik

eingereicht an der

Mathematisch-Naturwissenschaftlichen Fakultät I

der Humboldt-Universität zu Berlin

von

Andreas Kopp

geboren am 14. April 1970 in Rathenow

Präsident der Humboldt-Universität zu Berlin
Prof. Dr. Dr. h.c. Hans Meyer

Dekan der Mathematisch-Naturwissenschaftlichen Fakultät I
Prof. Dr. Jürgen Rabe

Gutachter:
1. Prof. Dr. T. Hebbeker
2. Prof. Dr. G. Coignet
3. Prof. Dr. P. Söding

Tag der mündlichen Prüfung: 21. Februar 2000

Zusammenfassung

In dieser Arbeit wird die Suche nach Higgs-Bosonen, die von verschiedenen theoretischen Modellen vorhergesagt werden, beschrieben. Mit Hilfe dieser Teilchen kann die Existenz massiver Bosonen und Fermionen erklärt werden. Die Suche wurde in experimentell verwandten Kanälen, die durch geladene Leptonen im Endzustand gekennzeichnet sind, durchgeführt. Die Analyse erfolgte auf der Grundlage von Daten, die in den Jahren 1996–1998 mit dem L3-Detektor am Elektron-Positron-Speicherring LEP aufgezeichnet wurden.
Die dabei beobachten Kandidaten stimmen mit der Erwartung von Untergrundprozessen, die durch das Standardmodell beschrieben werden, überein. Die Produktion von Higgs-Bosonen konnte nicht nachgewiesen werden. Neue Massengrenzen wurden bestimmt, die den bisherigen Erkenntnisstand signifikant erweitern.
Bei der Suche nach dem Higgs-Boson des Standardmodells wurden die Kanäle $\mathrm{hZ} \to \mathrm{b\bar{b}}\ell^+\ell^-$ $(\ell = \mathrm{e}, \mu, \tau)$ und $\mathrm{hZ} \to \tau^+\tau^-\mathrm{q\bar{q}}$ bei Schwerpunktsenergien zwischen 183 und 189 GeV analysiert. Eine untere Massengrenze von

$$\mathrm{m_h} > 87.5 \ \ \mathrm{GeV}$$

auf dieses Teilchen wurde mit einem Vertrauensniveau von 95% bestimmt. Kombiniert man die in dieser Arbeit analysierten Kanäle mit dem $\mathrm{hZ} \to \mathrm{b\bar{b}q\bar{q}}$ und dem $\mathrm{hZ} \to \mathrm{b\bar{b}}\nu\bar{\nu}$ Kanal, erhält man eine untere Massengrenze von

$$\mathrm{m_h} > 95.3 \ \ \mathrm{GeV}.$$

Für die Interpretation der Ergebnisse im Rahmen der minimal supersymmetrischen Erweiterung des Standardmodells (MSSM) wurden die Standardmodellanalysen durch die Kanäle $\mathrm{hA} \to \mathrm{b\bar{b}}\tau^+\tau^-$ ($\mathrm{hA} \to \tau^+\tau^-\mathrm{b\bar{b}}$) ergänzt. In der Kombination mit dem $\mathrm{hA} \to \mathrm{b\bar{b}b\bar{b}}$ Kanal wurden Massengrenzen als Funktion von $\tan\beta$ abgeleitet. Die unteren Massengrenzen für $\tan\beta > 1$ sind:

$$\begin{aligned} \mathrm{m_h} &> 77.1 \ \ \mathrm{GeV} \\ \mathrm{m_A} &> 77.1 \ \ \mathrm{GeV}. \end{aligned}$$

Für das minimale (maximale) Mischungsszenario im skalaren Topsektor können die Bereiche $0.7 \leq \tan\beta \leq 2.6$ $(0.8 \leq \tan\beta \leq 1.5)$ ausgeschlossen werden.
Nach geladenen Higgs-Bosonen wurde im $\mathrm{H^+H^-} \to \mathrm{c\bar{s}}\tau^-\bar{\nu}_\tau$ Kanal bei Schwerpunktsenergien zwischen 130 und 189 GeV im Rahmen allgemeiner Zwei-Dublett-Modelle gesucht.

Massengrenzen als Funktion des Verzweigungsverhältnisses der geladenen Higgs-Bosonen in den Endzustand $\tau\nu$ werden angegeben. Die Kombination dieses Kanals mit den $H^+H^- \to c\bar{s}\bar{c}s$ und $H^+H^- \to \tau^+\nu_\tau\tau^-\bar{\nu}_\tau$ Kanälen erlaubt es, geladene Higgs-Bosonen mit Massen

$$m_{H^\pm} \leq 65.5 \text{ GeV}$$

unabhängig vom Verzweigungsverhältnis auszuschließen.
Für Schwerpunktsenergien oberhalb von 180 GeV sagt das Standardmodell die resonante Paarproduktion von Z-Bosonen, $e^+e^- \to ZZ$, voraus. Für diesen erstmals experimentell untersuchten Prozeß wurden die folgenden Wirkungsquerschnitte gemessen:

$$\sigma_{ZZ\to q\bar{q}\ell^+\ell^-} = 0.054^{+0.134}_{-0.034} \text{ (stat.)} \pm 0.002 \text{ (sys.) pb bei } 183 \text{ GeV},$$

$$\sigma_{ZZ\to q\bar{q}\ell^+\ell^-} = 0.096^{+0.039}_{-0.033} \text{ (stat.)} \pm 0.003 \text{ (sys.) pb bei } 189 \text{ GeV}.$$

Die Vorhersage des Standardmodells stimmt mit dieser Messung überein.

Abstract

This thesis is devoted to the search for Higgs bosons predicted by various theoretical models. By the introduction of these particles into the theory, the masses of bosons and fermions can be explained. The search is performed in experimentally related channels, which are characterised by charged leptons in the final state. The analysis uses data taken during the years 1996–1998 with the L3 detector at the Large Electron Positron collider LEP.
The observed candidates are consistent with the expectation from Standard Model background processes. Evidence for Higgs boson production could not be found. New mass limits were determined superseding previous mass limits established by L3 and other experiments.
In the search for the Higgs boson of the Standard Model the channels $\mathrm{hZ} \to \mathrm{b\bar{b}}\ell^+\ell^-$ ($\ell = \mathrm{e}, \mu, \tau$) and $\mathrm{hZ} \to \tau^+\tau^-\mathrm{q\bar{q}}$ were analysed at centre-of-mass energies between 183 and 189 GeV. A lower mass limit of

$$\mathrm{m_h} > 87.5 \ \ \mathrm{GeV}$$

is derived at the 95% confidence level. Combining these channels with the $\mathrm{hZ} \to \mathrm{b\bar{b}q\bar{q}}$ and the $\mathrm{hZ} \to \mathrm{b\bar{b}}\nu\bar{\nu}$ channel leads to a lower mass limit of

$$\mathrm{m_h} > 95.3 \ \ \mathrm{GeV}.$$

For the interpretation of the results in the framework of the minimal supersymmetric model (MSSM), the Standard Model analyses are complemented with the channels $\mathrm{hA} \to \mathrm{b\bar{b}}\tau^+\tau^-$ ($\mathrm{hA} \to \tau^+\tau^-\mathrm{b\bar{b}}$). In combination with the $\mathrm{hA} \to \mathrm{b\bar{b}b\bar{b}}$ channel, mass limits as a function of $\tan\beta$ are derived. The lower mass limits for $\tan\beta > 1$ are:

$$\begin{aligned} \mathrm{m_h} &> 77.1 \ \ \mathrm{GeV} \\ \mathrm{m_A} &> 77.1 \ \ \mathrm{GeV}. \end{aligned}$$

For the minimal (maximal) stop mixing scenario, values of $0.7 \leq \tan\beta \leq 2.6$ ($0.8 \leq \tan\beta \leq 1.5$) can be excluded.
A search for charged Higgs bosons is carried out in the $\mathrm{H^+H^-} \to \mathrm{c\bar{s}}\tau^-\bar{\nu}_\tau$ channel at centre-of-mass energies between 130 and 189 GeV within the framework of general two doublet models. Mass limits as a function of the branching ratio of the charged Higgs bosons into $\tau\nu$ are derived. The combination of this channel with the $\mathrm{H^+H^-} \to \tau^+\nu_\tau\tau^-\bar{\nu}_\tau$

and the $H^+H^- \to c\bar{s}\bar{c}s$ channel makes it possible to exclude charged Higgs bosons with masses below

$$m_{H^\pm} \leq 65.5 \text{ GeV}$$

independent of the branching ratio.
For centre-of-mass energies larger than 180 GeV the Standard Model predicts the resonant pair production of Z bosons, $e^+e^- \to ZZ$. For this process, which is experimentally accessible for the first time, the following cross sections have been measured:

$$\sigma_{ZZ\to q\bar{q}\ell^+\ell^-} = 0.054^{+0.134}_{-0.034} \text{ (stat.)} \pm 0.002 \text{ (sys.) pb at 183 GeV},$$

$$\sigma_{ZZ\to q\bar{q}\ell^+\ell^-} = 0.096^{+0.039}_{-0.033} \text{ (stat.)} \pm 0.003 \text{ (sys.) pb at 189 GeV}.$$

The prediction of the Standard Model is in agreement with this measurement.

Der Mensch muß bei dem Glauben verharren,
daß das Unbegreifliche begreiflich sei;
er würde sonst nicht forschen.

(Johann Wolfgang von Goethe)

Contents

1 Introduction **1**

2 The Theory **3**
2.1 Symmetry and Gauge Invariance 3
2.2 The Electroweak Standard Model 4
2.3 The Higgs Mechanism 6
2.3.1 Spontaneous Symmetry Breaking 6
2.3.2 The Higgs Boson in the Standard Model 7
2.3.3 Two Doublet Models 11
2.4 Higgs Production at LEP 15
2.4.1 Production of the Standard Model Higgs Boson 15
2.4.2 Production of Neutral Higgs Bosons in the MSSM 16
2.4.3 Production of Charged Higgs Bosons 17
2.5 Higgs Boson Decay 19
2.5.1 Decay of the Standard Model Higgs Boson 19
2.5.2 Decay of h and A in the MSSM 21
2.5.3 Decay of Charged Higgs Bosons 21
2.6 Restrictions on Higgs Boson Masses 21
2.6.1 Theoretical Bounds 22
2.6.2 Limits from Indirect Searches 23
2.6.3 Limits from Direct Searches 25

3 The Experiment **27**
3.1 The e^+e^-Collider LEP 27
3.2 The L3 Detector 28
3.2.1 The Silicon Microvertex Detector 29
3.2.2 The Central Tracking Chambers 31
3.2.3 The Electromagnetic Calorimeter 32
3.2.4 The Scintillators 33
3.2.5 The Hadron Calorimeter 33
3.2.6 The Muon Detector 34
3.2.7 The Luminosity Monitor 34
3.2.8 The Trigger System 35

4 Data Sample and Monte Carlo Simulation **37**
4.1 Data Sample . . . 37
4.2 Physics Processes at LEP2 Energies . . . 38
4.3 Simulation and Reconstruction . . . 40

5 Search for the Standard Model Higgs Boson **41**
5.1 Analysis Method . . . 41
5.1.1 Lepton Identification . . . 42
5.1.2 B-tagging . . . 45
5.1.3 The DURHAM Jet Clustering Algorithm . . . 46
5.1.4 Kinematic Fits . . . 48
5.1.5 The Discriminant Variable . . . 48
5.2 The hZ $\rightarrow b\bar{b}e^+e^-$ Channel . . . 50
5.3 The hZ $\rightarrow b\bar{b}\mu^+\mu^-$ Channel . . . 54
5.4 The hZ $\rightarrow b\bar{b}\tau^+\tau^-$ and the hZ $\rightarrow \tau^+\tau^-q\bar{q}$ Channels . . . 57
5.5 Analysis Performance and Cross Efficiencies . . . 60
5.6 Systematic Errors . . . 62
5.7 The Other Channels . . . 64

6 Search for Neutral Higgs Bosons in the MSSM **69**
6.1 The hA $\rightarrow b\bar{b}\tau^+\tau^-$ Channel . . . 69
6.2 The hA $\rightarrow b\bar{b}b\bar{b}$ Channel . . . 74
6.3 The hZ $\rightarrow AAf\bar{f}$ Channel . . . 74

7 Search for Charged Higgs Bosons **77**
7.1 The $H^+H^- \rightarrow c\bar{s}\tau^-\bar{\nu}_\tau$ Channel . . . 77
7.2 The Other Channels . . . 81

8 Interpretation **83**
8.1 Confidence Level Calculation . . . 83
8.2 Mass Limit in the Standard Model . . . 85
8.3 Mass Limits in the MSSM . . . 87
8.4 Mass Limits for Charged Higgs Bosons . . . 90

9 Observation of Resonant ZZ Production **93**
9.1 Signal Definition . . . 93
9.2 The ZZ $\rightarrow q\bar{q}\ell^+\ell^-$ Channel . . . 93
9.3 The ZZ Cross Section . . . 96
9.4 Systematic Errors . . . 97

10 Conclusions **99**
10.1 Higgs Searches . . . 99
10.2 ZZ Production . . . 100
10.3 Perspectives on Further Searches . . . 101

A SM Higgs at 183 GeV **105**

B MSSM Higgs at 183 GeV **107**

C Charged Higgs between 130 and 183 GeV **109**

D ZZ Production at 183 GeV **112**

E Selection of Reference Samples **114**

Bibliography **117**

Acknowledgements **125**

Chapter 1

Introduction

Particle physics investigates and explores the fundamental constituents and forces of our world. Starting from studying blocks of matter and discovering the atomic structure, physicists have gone deeper and deeper to find the fundamental components of our matter and are still occupied with structuring the objects and their interactions which were found during this very fruitful exploration. Experiment and theory go hereby hand in hand pushing each other further. Theories have been developed to describe experimental observations making suggestions on further investigations which usually result in setting up new experiments. As the understanding of the fundamental particles requires very high energies, those experiments are carried out at particle accelerators. One of these accelerators is the Large Electron Positron Collider (LEP) at the European Centre for Particle Physics CERN near Geneva. It is today the biggest electron positron collider in the world allowing collisions at energies close to 200 GeV.
The minimal theory, which can accurately describe the observations made at LEP and other accelerators, is referred to as the Standard Model [1]. The Standard Model describes strong and electroweak interactions starting from a fundamental principal, which is the requirement to conserve certain physical quantities in space and time. This naturally introduces the interactions of fermions (Spin$-\frac{1}{2}$ particles) by the exchange of bosons (Spin-1 particles). The fascinating result of this approach was the prediction of the heavy gauge bosons $W^{\pm}$ and Z, which were later observed by the UA1 experiment at CERN [2]. The introduction of heavy gauge bosons in the theory is non-trivial and is realised in a very specific way by introducing one more particle, the Higgs boson. The gauge bosons and also the fermions acquire mass through their coupling to this particle. The theory makes predictions on the production and the decay of the Higgs boson as a function of its mass, but the mass itself remains a free parameter. One of the main tasks of the experiments at LEP is to probe the existence of the Higgs boson.
The introduction of massive gauge bosons and fermions requires in the minimal version of the Standard Model one weak Higgs field isospin doublet which manifests itself as one physical particle. But clearly, theoretically the masses can also be generated by introducing more complicated Higgs models. Especially, if one tries to understand the particle interactions from a more fundamental point of view, the Higgs sector needs to be extended. There is some common belief among many physicists that the strong, the electroweak and the gravitational force can be unified at an energy scale of $\approx 10^{19}$ GeV.

One of the most favoured theories to achieve this goal is supersymmetry. Supersymmetry establishes a symmetry between bosons and fermions by at least doubling the particle spectrum. The Higgs sector must contain at least two Higgs field doublets, which lead to 5 physical Higgs bosons: a pair of charged Higgs bosons and three neutral ones.
The Standard Model and the more general two doublet models with and without supersymmetry make specific predictions on how Higgs bosons should be produced and detected at LEP energies.
This thesis is devoted to the search for the Higgs boson in the Standard Model, the lightest neutral Higgs bosons of the minimal supersymmetric extension of the Standard Model and to the search for charged Higgs bosons in general two doublet models. The search is performed in experimentally related search channels, where charged leptons are predicted in the final state resulting either from Higgs decays or from the decay of the Z boson which is produced together with the Higgs boson in the case of the Standard Model. The results are then combined with other search channels. The thesis is complemented with a cross section measurement of resonant ZZ production, which is the most difficult background source in the case of the Standard Model Higgs boson.

Chapter 2

The Theory

Theoretical physics is the attempt to understand and to explain observations, to structure physical objects and interactions, to draw conclusions and to make predictions which can be verified by experiments. The strategy herein is to start from fundamental principles and to derive a self-contained theory. The value of this theory is then measured on how accurately it describes the experimental facts.

2.1 Symmetry and Gauge Invariance

A successful approach in describing the interactions of elementary particles is given by gauge theories. Gauge theories are guided by the idea of symmetry. Requiring the invariance of physical properties under local gauge transformations naturally introduces the interaction of fermions (Spin $-\frac{1}{2}$ particles) by the exchange of gauge bosons (Spin -1 particles).

Particles in quantum field theory are represented as fields with a certain amplitude $\Psi(\vec{\mathrm{x}},\mathrm{t})$ in space and time. A phase transformation

$$\Psi(\vec{\mathrm{x}},\mathrm{t}) \rightarrow \Psi^{'}(\vec{\mathrm{x}},\mathrm{t}) = \mathrm{e}^{\mathrm{i}\chi(\vec{\mathrm{x}},\mathrm{t})}\Psi(\vec{\mathrm{x}},\mathrm{t}) \tag{2.1}$$

is called a local gauge transformation. However, if one considers, for instance, the Lagrangian of a free fermion with mass m

$$\mathcal{L} = i\bar{\Psi}\gamma^{\mu}\partial_{\mu}\Psi - \mathrm{m}\bar{\Psi}\Psi, \tag{2.2}$$

one realises that it is not invariant under a local gauge transformation given by Equation 2.1. If one introduces a new derivative

$$\mathrm{D}_{\mu} \equiv \partial_{\mu} - i\mathrm{e}\mathrm{A}_{\mu}(\vec{\mathrm{x}},\mathrm{t}), \tag{2.3}$$

where A_{μ} is a vector field which transforms as

$$\mathrm{A}_{\mu} \rightarrow \mathrm{A}_{\mu} + \frac{1}{\mathrm{e}}\partial_{\mu}\chi, \tag{2.4}$$

one arrives at a new Lagrangian

$$\mathcal{L} = i\bar{\Psi}\gamma^{\mu}\mathrm{D}_{\mu}\Psi - \mathrm{m}\bar{\Psi}\Psi, \tag{2.5}$$

that has the desired invariance under a transformation given by Equation 2.1. That means, the requirement of a local gauge invariance has lead to the introduction of a vector particle, the photon, associated to the A_{μ} field. Adding the kinematic part of the photon to the Lagrangian leads to the final Lagrangian of Quantum Electrodynamics (QED):

$$\mathcal{L} = \bar{\Psi}(i\gamma^{\mu}\partial_{\mu} - m)\Psi + \mathrm{e}\bar{\Psi}\gamma^{\mu}\mathrm{A}_{\mu}\Psi - \frac{1}{4}\mathrm{F}_{\mu\nu}\mathrm{F}^{\mu\nu}. \tag{2.6}$$

2.2 The Electroweak Standard Model

The minimal theory, which presently describes the experimental data best, is called Standard Model. It describes the strong and the electroweak interactions of all particles known today. In the following only the electroweak part of the Standard Model is discussed.

The electroweak Standard Model established by Glashow, Salam and Weinberg [1] is a gauge theory which unifies the electromagnetic and the weak force. Its importance is based on the successful description and ordering of particles and their properties which were observed in experiments. One of the most striking and convincing arguments in favour of this theory was the prediction of the heavy gauge bosons $\mathrm{W}^{\pm}$ and Z. The observation of weak neutral current reactions by the Gargamelle Neutrino Collaboration in 1973 can be considered as a milestone for the manifestation of the Glashow-Salam-Weinberg-Model as a standard theory [3]. Eventually, the discovery of $\mathrm{W}^{\pm}$ and Z bosons in 1983 were the breakthrough of the model [2].

The electroweak Standard Model is a non-Abelian theory based on the $\mathrm{SU}(2) \times \mathrm{U}(1)$ group. The generators of the group are the three components of the weak isospin $\vec{\mathrm{T}}$ and the hypercharge Y. They are related to the electromagnetic charge in the following way:

$$\mathrm{Q} = \mathrm{T}_3 + \mathrm{Y}. \tag{2.7}$$

Parity violation is introduced by grouping left-handed and right-handed particles in different weak isospin multiplets. Left-handed fermions are grouped in doublets whereas right-handed fermions are singlets. Table 2.1 summarises the fermions of the Standard Model. Requiring invariance of the Lagrangian under a local $\mathrm{SU}(2) \times \mathrm{U}(1)$ gauge transformation leads to the introduction of four gauge fields $\mathrm{W}^{\mathrm{i}}_{\mu}, \mathrm{i} = 1..3$ and B_{μ} with the covariant derivative:

$$\mathrm{D}_{\mu} = \partial_{\mu} + i\mathrm{g}_1\mathrm{Y}\mathrm{B}_{\mu} + i\mathrm{g}_2\frac{\tau_i}{2}\mathrm{W}^{\mathrm{i}}_{\mu}. \tag{2.8}$$

In this representation the generators of the weak isospin are denoted by the Pauli spin matrices $\vec{\tau} = 2\vec{T}$; g_1 and g_2 are the coupling constants of the interactions. The Lagrangian of the electroweak Standard Model can then be written as the sum of four independent terms:

$$\mathcal{L} = \mathcal{L}_{\mathrm{Fermion}} + \mathcal{L}_{\mathrm{Gauge}} + \mathcal{L}_{\mathrm{Higgs}} + \mathcal{L}_{\mathrm{Yukawa}}, \tag{2.9}$$

	Family 1	2	3	T_3	Y	Q
Leptons	$\begin{pmatrix} \nu_e \\ e \end{pmatrix}_L$	$\begin{pmatrix} \nu_\mu \\ \mu \end{pmatrix}_L$	$\begin{pmatrix} \nu_\tau \\ \tau \end{pmatrix}_L$	$1/2$ $-1/2$	$-1/2$ $-1/2$	0 -1
	e_R	μ_R	τ_R	0	-1	-1
Quarks	$\begin{pmatrix} u \\ d' \end{pmatrix}_L$	$\begin{pmatrix} c \\ s' \end{pmatrix}_L$	$\begin{pmatrix} t \\ b' \end{pmatrix}_L$	$1/2$ $-1/2$	$1/6$ $1/6$	$2/3$ $-1/3$
	u_R	c_R	t_R	0	$2/3$	$2/3$
	d_R	s_R	b_R	0	$-1/3$	$-1/3$

Table 2.1: *Multiplet and quantum number assignments for the fermions in the Standard Model. The prime indicates that the weak eigenstates of the quarks are not their mass eigenstates. The quark mixing is described by the Cabibbo-Kobayashi-Maskawa matrix. The indices L(R) denote left(right)-handed fermions.*

where $\mathcal{L}_{\text{Fermion}}$ describes massless fermion fields and their interaction with the gauge fields:

$$\mathcal{L}_{\text{Fermion}} = i\bar{\Psi}\gamma^\mu D_\mu \Psi. \tag{2.10}$$

The term $\mathcal{L}_{\text{Gauge}}$ contains the kinetic energy of the massless gauge fields B and $\vec{W}$ and the self interaction of the $\vec{W}$ fields:

$$\mathcal{L}_{\text{Gauge}} = -\frac{1}{4}\vec{W}_{\mu\nu}\vec{W}^{\mu\nu} - \frac{1}{4}B_{\mu\nu}B^{\mu\nu}, \tag{2.11}$$

where

$$\vec{W}_{\mu\nu} = \partial_\mu \vec{W}_\nu - \partial_\nu \vec{W}_\mu + g_2 \vec{W}_\mu \times \vec{W}_\nu \tag{2.12}$$

$$B_{\mu\nu} = \partial_\mu B_\nu - \partial_\nu B_\mu. \tag{2.13}$$

The second term in Equation 2.12 is the self interaction of the $\vec{W}$ fields. It arises from the non-abelian character of the SU(2) group (the Pauli spin matrices do not commute). The terms $\mathcal{L}_{\text{Higgs}}$ and $\mathcal{L}_{\text{Yukawa}}$ describe the interaction of the gauge and the fermion fields with a new field, the Higgs, which is introduced to give masses to the gauge bosons. The structure of these terms will be discussed in section 2.3.2.
The mass eigenstates of the W particles are:

$$W^\pm_\mu = \frac{1}{\sqrt{2}}(W^1_\mu \mp iW^2_\mu). \tag{2.14}$$

The photon field A_μ and the field of the Z boson Z_μ are linear combinations of B_μ and W^3_μ:

$$A_\mu = B_\mu \cos\theta_W + W^3_\mu \sin\theta_W \tag{2.15}$$

$$Z_\mu = -B_\mu \sin\theta_W + W^3_\mu \cos\theta_W. \tag{2.16}$$

The weak mixing angle θ_W depends on the coupling constants g_1 and g_2:

$$\sin\theta_W = \frac{g_1}{\sqrt{g_1^2 + g_2^2}} \qquad \cos\theta_W = \frac{g_2}{\sqrt{g_1^2 + g_2^2}}. \tag{2.17}$$

So far, the gauge bosons, which were naturally introduced by requiring SU(2) × U(1) gauge invariance, are massless. However, the Z and $W^{\pm}$ bosons as well as the fermions are massive. Mass terms such as $\frac{1}{2}m^2 B_\mu B^\mu$ for bosons and $m\bar{\Psi}\Psi$ for fermions would destroy the gauge invariance of the Lagrangian. Therefore, the mass is introduced in a very specific way, which is discussed in the next section.

2.3 The Higgs Mechanism

2.3.1 Spontaneous Symmetry Breaking

The Higgs mechanism [4] is introduced to give masses to the $W^{\pm}$ and Z bosons while keeping the invariance under a local SU(2) × U(1) gauge transformation. The same mechanism can be used to generate the fermion masses. In this section the general idea of spontaneous symmetry breaking is discussed.

Assuming one has a scalar field with the potential

$$V(\Phi) = \frac{1}{2}\mu^2\Phi^2 + \frac{1}{4}\lambda\Phi^4 \tag{2.18}$$

with $\mu^2 < 0$ and $\lambda > 0$. A potential, defined in this way, has one maximum at $\Phi = 0$ and two minima at $\Phi = \pm\nu$ where

$$\nu = \sqrt{\frac{-\mu^2}{\lambda}}. \tag{2.19}$$

The ground state ν is called the vacuum state. Such a potential (see Figure 2.1), where the vacuum state does not have the same symmetry as the potential itself, is called spontaneously broken. Or in other words: the symmetry is hidden by the choice of the vacuum state.

Particles are quantum excitations of the vacuum state. Therefore, one can construct the particle spectrum by expanding the field Φ around the vacuum state:

$$\Phi(x) = \nu + h(x). \tag{2.20}$$

The Lagrangian of the scalar Higgs field

$$\mathcal{L} = \frac{1}{2}\partial_\mu\Phi\partial^\mu\Phi - (\frac{1}{2}\mu^2\Phi^2 + \frac{1}{4}\lambda\Phi^4) \tag{2.21}$$

then becomes

$$\mathcal{L} = \frac{1}{2}\partial_\mu h\partial^\mu h - (\lambda\nu^2 h^2 + \lambda\nu h^3 + \frac{1}{4}\lambda h^4) + \text{constant}. \tag{2.22}$$

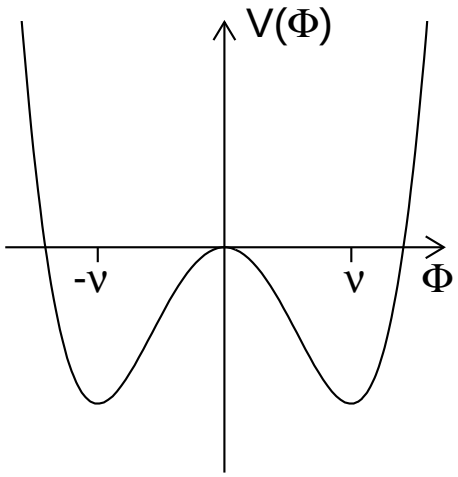

Figure 2.1: *Spontaneously broken potential* $\mathrm{V}(\Phi)$*. The vacuum states do not hold the symmetry of the potential.*

The obvious symmetry $\Phi \rightarrow -\Phi$ of the Lagrangian given by Equation 2.21 is well hidden in Equation 2.22, although the two representations are completely equivalent. The term proportional to h^2 is interpreted as a mass term with

$$\mathrm{m}_\mathrm{h}^2 = 2\lambda\nu^2 = -2\mu^2, \tag{2.23}$$

whereas the higher order terms of h are self-interaction terms of the h field.

2.3.2 The Higgs Boson in the Standard Model

In the last section a mass for a spin-0 particle was created by choosing a non-zero vacuum expectation value, which breaks spontaneously the symmetry of a Lagrangian, that was invariant under a $\Phi \rightarrow -\Phi$ transformation.

In the Standard Model we require the gauge invariance under a local $\mathrm{SU}(2) \times \mathrm{U}(1)$ transformation (see section 2.2). Massive gauge bosons are needed to explain the "weakness" of interactions at low energies. The minimal model which can generate these masses without violating the gauge invariance of the Lagrangian is an one-doublet Higgs model. In this model the Higgs boson is introduced as a weak isospin doublet:

$$\Phi = \begin{pmatrix} \Phi^+ \\ \Phi^0 \end{pmatrix} \tag{2.24}$$

with the complex fields

$$\Phi^+ = \frac{\Phi_1 + i\Phi_2}{\sqrt{2}}, \tag{2.25}$$

$$\Phi^0 = \frac{\Phi_3 + i\Phi_4}{\sqrt{2}}. \tag{2.26}$$

The Higgs potential is now

$$\mathrm{V}(\Phi) = \mu^2\Phi^\dagger\Phi + \lambda(\Phi^\dagger\Phi)^2. \tag{2.27}$$

Remembering, that for keeping the local $\mathrm{SU}(2) \times \mathrm{U}(1)$ gauge invariance, the partial derivative ∂_μ must be replaced by the covariant derivative of Equation 2.8, leads to the Lagrangian

$$\mathcal{L}_{\mathrm{Higgs}} = (\mathrm{D}_\mu\Phi)^\dagger(\mathrm{D}^\mu\Phi) - \mu^2\Phi^\dagger\Phi - \lambda(\Phi^\dagger\Phi)^2. \tag{2.28}$$

The minima of the Higgs potential for $\mu^2 < 0$ are at

$$\Phi^\dagger\Phi = \frac{\Phi_1^2 + \Phi_2^2 + \Phi_3^2 + \Phi_4^2}{2} = \frac{-\mu^2}{2\lambda} = \frac{\nu^2}{2}. \tag{2.29}$$

Choosing one particular ground state $\Phi_3 = \nu, \Phi_1 = \Phi_2 = \Phi_4 = 0$ and expanding around it, leads to

$$\Phi(\mathrm{x}) = \frac{1}{\sqrt{2}} \begin{pmatrix} 0 \\ \nu + \mathrm{h}(\mathrm{x}) \end{pmatrix}. \tag{2.30}$$

One should note, that this choice is not random. Choosing only for Φ^0 a non-zero vacuum expectation value and setting Φ^+ to zero, ensures that the electric charge is conserved. A non-zero vacuum expectation value of Φ^+ would lead to electric charge violation, which is in contradiction to experiment [5].
The O(4) symmetry of Equation 2.29 has been broken down to a O(1) symmetry corresponding to the $\mathrm{U}(1)_{\mathrm{em}}$ group of electromagnetism. Three fields have been "gauged away". They will become the longitudinal polarisation states of the $\mathrm{W}^\pm$ and Z bosons which are needed for massive gauge bosons. Investigating the first term in Equation 2.28 at the vacuum state and inserting $\mathrm{Y} = 1/2$ yields:

$$\begin{aligned} &| \, (i\mathrm{g}_1\mathrm{Y}\mathrm{B}_\mu + i\frac{\mathrm{g}_2}{2}\vec{\tau}\vec{\mathrm{W}}_\mu)\frac{1}{\sqrt{2}} \begin{pmatrix} 0 \\ \nu \end{pmatrix}) \, |^2 \\ &= \frac{1}{8}\nu^2\mathrm{g}_2^2((\mathrm{W}_\mu^1)^2 + (\mathrm{W}_\mu^2)^2) + \frac{1}{8}\nu^2(\mathrm{g}_1\mathrm{B}_\mu - \mathrm{g}_2\mathrm{W}_\mu^3)^2 \\ &= (\frac{1}{2}\nu\mathrm{g}_2)^2\mathrm{W}_\mu^+\mathrm{W}^{-\mu} + \frac{1}{2}(\frac{1}{2}\nu\sqrt{\mathrm{g}_1^2 + \mathrm{g}_2^2})^2\mathrm{Z}_\mu\mathrm{Z}^\mu. \end{aligned} \tag{2.31}$$

For deriving the last line, the identities given by the Equations 2.14, 2.16 and 2.17 were used. For charged bosons one expects a mass term $\mathrm{m}_\mathrm{W}^2\mathrm{W}_\mu^+\mathrm{W}^{-\mu}$ and for the neutral bosons $\frac{1}{2}(\mathrm{Z}_\mu\mathrm{Z}^\mu + \mathrm{A}_\mu\mathrm{A}^\mu)$. Therefore, the masses of the gauge bosons are given by:

$$\boxed{\mathrm{m}_\mathrm{W} = \tfrac{1}{2}\nu\mathrm{g}_2,} \tag{2.32}$$

$$\boxed{\mathrm{m}_\mathrm{Z} = \tfrac{1}{2}\nu\sqrt{\mathrm{g}_1^2 + \mathrm{g}_2^2},} \tag{2.33}$$

		T_3	Y	Q
Gauge Bosons	γ	0	0	0
	Z	0	0	0
	W^+	+1	0	+1
	W^-	−1	0	−1
Higgs	$\Phi = \begin{pmatrix} \Phi^{(+)} \\ \Phi^{(0)} \end{pmatrix}$	+1/2 −1/2	+1/2 +1/2	1 0

Table 2.2: *Quantum number assignments of the bosons in the Standard Model.*

and

$$\boxed{m_\gamma = 0.} \tag{2.34}$$

The last equation is derived from the fact that there is no term of the form $A_\mu A^\mu$ in Equation 2.31. Using Equation 2.17 sets the boson masses in relation to the weak mixing angle:

$$\boxed{\cos\theta_W = \frac{m_W}{m_Z}.} \tag{2.35}$$

A useful quantity which is often referred to is $\rho = m_W/m_Z\cos\theta_W$. As can be seen from Equation 2.35, the Standard Model predicts $\rho = 1$. The experimental values of the m_W, m_Z and $\sin^2\theta_W$ have been precisely measured and yield $\rho = 1$. Any theory making predictions on the mass generation will have to reproduce these measurements.
The Higgs mass is predicted to be:

$$\boxed{m_h = \sqrt{2\lambda}\nu.} \tag{2.36}$$

Since λ is unknown, it remains a free parameter of the theory. The bosons and their quantum number assignments in the Standard Model are summarised in Table 2.2

Fermion Masses

The fermion masses are generated by adding a SU(2) × U(1) gauge invariant interaction term of the Higgs field with the fermion fields to the Lagrangian. For the first lepton family (and similarly for the other lepton flavours) this is:

$$\mathcal{L}_{\text{Yukawa}} = g_e \left[(\bar{\nu}, \bar{e})_L \begin{pmatrix} \Phi^+ \\ \Phi^0 \end{pmatrix} e_R + \bar{e}_R (\Phi^-, \bar{\Phi}^0) \begin{pmatrix} \nu_e \\ e \end{pmatrix}_L \right]. \tag{2.37}$$

After spontaneous symmetry breaking (Equation 2.30), one obtains:

$$\mathcal{L}_{\text{Yukawa}} = \frac{g_e}{\sqrt{2}}\nu(\bar{e}_L e_R + \bar{e}_R e_L) + \frac{g_e}{\sqrt{2}}(\bar{e}_L e_R + \bar{e}_R e_L)h, \tag{2.38}$$

from which we can conclude that the electron mass is:

$$m_e = \frac{g_e \nu}{\sqrt{2}}, \tag{2.39}$$

whereas the neutrino remains massless. One should note, that the coupling constant g_e is not determined by the theory. However from Equation 2.39 it can be seen that it is proportional to the electron mass. Quark masses can be generated similarly. In order to allow masses for up-type quarks the charge-conjugate Higgs doublet is used:

$$\Phi_c = -i\tau_2\Phi^* = \begin{pmatrix} -\bar{\Phi}^0 \\ \Phi^- \end{pmatrix}. \tag{2.40}$$

The Yukawa term then becomes:

$$\begin{aligned}\mathcal{L}_{\text{Yukawa}} = g_d \left[(\bar{u}, \bar{d})_L \begin{pmatrix} \Phi^+ \\ \Phi^0 \end{pmatrix} d_R + \bar{d}_R (\Phi^-, \bar{\Phi}^0) \begin{pmatrix} u \\ d \end{pmatrix}_L \right] \\ + g_u \left[(\bar{u}, \bar{d})_L \begin{pmatrix} -\bar{\Phi}^0 \\ \Phi^- \end{pmatrix} d_R + \bar{d}_R (-\Phi^0, \Phi^+) \begin{pmatrix} u \\ d \end{pmatrix}_L \right].\end{aligned} \tag{2.41}$$

After spontaneous symmetry breakdown this equation yields:

$$\mathcal{L}_{\text{Yukawa}} = \frac{g_d \nu}{\sqrt{2}} \bar{d}d + \frac{g_u \nu}{\sqrt{2}} \bar{u}u + \frac{1}{\sqrt{2}} g_d \bar{d}dh + \frac{1}{\sqrt{2}} g_u \bar{u}uh, \tag{2.42}$$

from where the down and up quark masses $\frac{g_d \nu}{\sqrt{2}}$ and $\frac{g_u \nu}{\sqrt{2}}$ are derived. In general the mass of any given fermion f is proportional to the coupling constant g_f to the Higgs boson:

$$\boxed{m_f = \frac{g_f \nu}{\sqrt{2}}.} \tag{2.43}$$

This proportionality predicts that the Higgs boson prefers to decay to the heavier fermions – a property which is used in presently ongoing searches. This will be discussed in detail in section 2.5.1.

2.3.3 Two Doublet Models

The Higgs sector of the Standard Model is made of one doublet. This is the minimum which is needed to generate the boson and the fermion masses. There is, however, no obvious reason why nature should have chosen the minimal model. There could be more doublets and also singlets. In more general approaches to particle physics such as supersymmetric models, there is in fact even the need for at least two Higgs doublets. The theory gets clearly more complicated, and we will stick in this section to the essentials necessary to understand the analysis and the conclusions which will be discussed in this thesis.

A simple introduction of two doublet models into the theory leads to flavour changing neutral currents (FCNCs) at tree level [6], which are, however, not observed by experiments. One can make the Higgs masses large enough (of order TeV) to suppress sufficiently FCNCs mediated by Higgs bosons to satisfy the experimental limits. In this case, the Higgs bosons were unreachable for the experiments at LEP.
A second possibility is based on a theorem from Glashow and Weinberg [7], which states that tree-level FCNCs are absent if all fermions of a given electric charge couple to no more than one Higgs doublet. There are two ways discussed in the literature to satisfy this requirement. In the first model (type I), the first doublet does not couple at all to fermions and the second doublet behaves like the doublet in the minimal model (see section 2.3.2). In the second case (type II models) the first doublet couples only to down-type quarks and leptons whereas the second couples only to up-type quarks and leptons. The Higgs sector of type II is necessary for supersymmetric models.
The most general potential involving two complex scalar doublet Higgs fields (Φ_1 and Φ_2), which breaks the SU(2) $\times$ U(1) down to $\mathrm{U(1)_{em}}$ is [8]:

$$\begin{aligned} \mathrm{V}(\Phi_1,\Phi_2) &= \lambda_1(\Phi_1^\dagger\Phi_1-\nu_1^2)^2+\lambda_2(\Phi_2^\dagger\Phi_2-\nu_2^2)^2 \\ &\quad +\lambda_3\left[(\Phi_1^\dagger\Phi_1-\nu_1^2)+(\Phi_2^\dagger\Phi_2-\nu_2^2)\right]^2 \\ &\quad +\lambda_4\left[(\Phi_1^\dagger\Phi_1)(\Phi_2^\dagger\Phi_2)-(\Phi_1^\dagger\Phi_2)(\Phi_2^\dagger\Phi_1)\right] \\ &\quad +\lambda_5\left[\mathrm{Re}(\Phi_1^\dagger\Phi_2)-\nu_1\nu_2\cos\xi\right]^2 \\ &\quad +\lambda_6\left[\mathrm{Im}(\Phi_1^\dagger\Phi_2)-\nu_1\nu_2\sin\xi\right]^2 \\ &\quad +\lambda_7\left[\mathrm{Re}\Phi_1^\dagger\Phi_2-\nu_1\nu_2\cos\xi\right]\left[\mathrm{Im}\Phi_1^\dagger\Phi_2-\nu_1\nu_2\sin\xi\right] \\ &\quad +\lambda_8, \end{aligned} \tag{2.44}$$

where the λ_i are real parameters and ν_1 and ν_2 are the vacuum expectation values of the two doublets. The phase ξ introduces CP violation into the Higgs sector. The minimum of the potential is at:

$$<\Phi_1>=\begin{pmatrix}0\\ \nu_1\end{pmatrix} \qquad <\Phi_2>=\begin{pmatrix}0\\ \nu_2 e^{i\xi}\end{pmatrix}. \tag{2.45}$$

A detailed discussion on CP violation in the Higgs sector can be found in Reference [9]. It will not be considered in this thesis, and the phase ξ is set to zero. One of the most important parameters in two doublet models is the ratio of the vacuum expectation values, which is defined as:

$$\boxed{\tan\beta = \frac{\nu_2}{\nu_1}.} \tag{2.46}$$

The particle spectrum consists of five physical Higgs bosons:

a charged pair

$$\mathrm{H}^{\pm} = -\Phi_1^{\pm}\sin\beta + \Phi_2^{\pm}\cos\beta \tag{2.47}$$

with mass squared ${\mathrm{m}_{\mathrm{H}^{\pm}}}^2 = \lambda_4(\nu_1^2 + \nu_2^2)$,

a CP-odd scalar Higgs boson

$$\mathrm{A} = \sqrt{2}(-\mathrm{Im}\Phi_1^0\sin\beta + \mathrm{Im}\Phi_2^0\cos\beta) \tag{2.48}$$

with mass squared ${\mathrm{m}_{\mathrm{A}}}^2 = \lambda_6(\nu_1^2 + \nu_2^2)$ and

two CP-even neutral scalar Higgs bosons

$$\mathrm{H} = \sqrt{2}\left[(\mathrm{Re}\Phi_1^0 - \nu_1)\cos\alpha + (\mathrm{Re}\Phi_2^0 - \nu_2)\sin\alpha\right], \tag{2.49}$$

$$\mathrm{h} = \sqrt{2}\left[-(\mathrm{Re}\Phi_1^0 - \nu_1)\sin\alpha + (\mathrm{Re}\Phi_2^0 - \nu_2)\cos\alpha\right], \tag{2.50}$$

where α is the Higgs mixing angle which depends on the components of the mass matrix of these two scalars:

$$\mathcal{M} = \begin{pmatrix} 4\nu_1^2(\lambda_1+\lambda_3) + \nu_2^2\lambda_5 & (4\lambda_3+\lambda_5)\nu_1\nu_2 \\ (4\lambda_3+\lambda_5)\nu_1\nu_2 & 4\nu_2^2(\lambda_2+\lambda_3) + \nu_1^2\lambda_5 \end{pmatrix}. \tag{2.51}$$

The physical masses of the CP-even Higgs bosons are given by:

$$\mathrm{m}^2_{\mathrm{H,h}} = \frac{1}{2}\left[\mathcal{M}_{11} + \mathcal{M}_{22} \pm \sqrt{(\mathcal{M}_{11}-\mathcal{M}_{22})^2 + 4\mathcal{M}_{12}^2}\right]. \tag{2.52}$$

The mixing angle α is obtained from:

$$\begin{aligned} \sin 2\alpha &= \frac{2\mathcal{M}_{12}}{\sqrt{(\mathcal{M}_{11}-\mathcal{M}_{22})^2 + 4\mathcal{M}_{12}^2}} \\ \cos 2\alpha &= \frac{\mathcal{M}_{11}-\mathcal{M}_{22}}{\sqrt{(\mathcal{M}_{11}-\mathcal{M}_{22})^2 + 4\mathcal{M}_{12}^2}} \end{aligned} \tag{2.53}$$

The gauge bosons acquire mass through their couplings to the Higgs bosons. The generated masses of the gauge bosons depend on the vacuum expectation values and the coupling constants g_1 and g_2 in the following way:

$$m_W = \frac{g_2}{2}\sqrt{\nu_1^2 + \nu_2^2}, \qquad m_Z = \frac{1}{2}\sqrt{(\nu_1^2 + \nu_2^2)(g_1^2 + g_2^2)}, \qquad m_\gamma = 0. \tag{2.54}$$

At current LEP energies the search for the Higgs bosons within two doublet models is as in the case of the one doublet model determined by the Higgs-fermion couplings. These depend on the type of the two doublet model, *i.e.* on how the Higgses are coupled to the fermions. The predicted decay of the neutral Higgs bosons within the minimal supersymmetric extension of the Standard Model (MSSM) is discussed in section 2.5.2. The decay of charged Higgs bosons is reviewed in section 2.5.3.

The Higgs Sector in the MSSM

Supersymmetry introduces a symmetry between fermions and bosons by placing them in multiplets similar to the arrangement of the up- and down-type fermions in the weak isospin space SU(2) or the arrangements of the quarks in colour space SU(3) allowing transformations between them. One of the big attractions in this approach is the possibility of unifying gravity with particle physics at the Planck scale ($\approx 10^{19}$ GeV), which is assumed to be the energy scale where the gravitational interactions of elementary particles become comparable to their strong and electroweak interactions. A most recent review article on supersymmetry can be found in Reference [10].
In the MSSM the particle spectrum is extended by introducing the supersymmetric partners for the SM particles. The supersymmetric partners differ in spin by half a unit to their SM counterparts. The Higgs sector consists of two Higgs doublets of type II defined above. The MSSM is made up of two sectors: a supersymmetry conserving sector and a supersymmetry breaking sector[1].
The supersymmetry conserving sector is parametrised through: (a) g_s, g_2 and g_1 corresponding to the SM gauge couplings of SU(3) × SU(2) × U(1) discussed in section 2.2, (b) a supersymmetry conserving mass parameter μ and (c) the Higgs-fermion Yukawa couplings λ_i.
The parameters of the supersymmetry breaking sector consist of: (a) gaugino Majorana masses M_3, M_2 and M_1 associated with the SU(3), SU(2) and U(1) subgroups of the Standard Model, (b) scalar squared-mass parameters for the squarks and sleptons, (c) Higgs-squark-squark and Higgs-slepton-slepton trilinear interaction terms A_i and (d) three scalar Higgs mass parameters.
It can be shown [11] that the minimum of the Higgs potential V defined in Equation 2.44 and the masses of the scalar Higgs bosons depend only on three parameters, hence introducing mass relations between the Higgs and the gauge bosons derived from Equation 2.52:

$$m_{H,h}{}^2 = \frac{1}{2}\left[m_A^2 + m_Z^2 \pm \sqrt{(m_A{}^2 + m_Z{}^2)^2 - 4m_Z{}^2 m_A{}^2 \cos^2 2\beta}\right]. \tag{2.55}$$

[1] If supersymmetry were an exact symmetry, then the particles and their superpartners would be degenerate in mass. Apparently, they are not, and, therefore, the symmetry is broken.

Furthermore, the relation

$$m_{H^{\pm}}^2 = {m_A}^2 + {m_W}^2 \tag{2.56}$$

can be derived. As can be seen from Equation 2.55 the lightest neutral Higgs boson is bound to be lighter than $m_Z \mid \cos 2\beta \mid$. According to Equation 2.56 the charged Higgs bosons must be heavier than m_W. All relations are given at tree level. The radiative corrections can be quite large, especially for the lightest Higgs boson h. They depend on the top mass and on the scalar top mixing, which also alters slightly the production cross section and the branching ratios as will be discussed in sections 2.4.2 and 2.5.2. There are two extreme mixing scenarios considered, which were suggested in Reference [12] and are referred to as maximal and minimal mixing. Unification assumptions for the sfermions masses m_0, the gaugino masses M_2 and the trilinear Higgs-sfermion couplings A are made at the GUT scale ($\approx 10^{16}$ GeV). These simplifications reduce significantly the number of free parameters, but have practically no impact on the MSSM Higgs phenomenology. In particular, a common scalar fermion mass and trilinear coupling is justified since only the scalar top sector gives important contributions to Higgs boson masses and couplings. This leaves us with 6 independent parameters, which are chosen to be the scalar fermion mass m_0, the gaugino mass parameter M_2, the Higgsino mass parameter μ, the trilinear Higgs-sfermion coupling A, the ratio of the vacuum expectation $\tan\beta$ and the mass of the CP-odd Higgs boson m_A. The parameters m_0 and M_2 are fixed to 1 TeV, which implies that Higgs decays into SUSY particles are kinematically forbidden. This is justified since Higgs decays to those particles are predicted in a parameter space which is well covered by the direct searches [13] and would therefore only be relevant if SUSY particles were discovered. The radiative corrections to the Higgs mass spectrum depend on the mass eigenstates of the scalar fermions. The dominant contribution arises from the non-diagonal entry in the scalar top mass matrix $m_t(A - \mu \cot\beta)$ because of the large top quark mass ($m_t \approx 175$ GeV). It has been shown in Reference [14, 15] that the impact of the scalar top mixing on the Higgs mass spectrum is minimal for vanishing mixing $m_0 \gg A \approx \mid \mu \mid$ and maximal for $m_0 \gg \mid \mu \mid$ and $A = \sqrt{6}$ TeV. It has been agreed among the LEP collaborations to fix the Higgsino parameter μ to -100 GeV. **Minimal mixing** corresponds to setting $A = 0$ and **maximal mixing** occurs at $A = \sqrt{6}$ TeV. After having fixed these parameters, cross sections and Higgs decays are fully determined by $\tan\beta$ and m_A.

2.4 Higgs Production at LEP

After having introduced the principal idea and the properties of Higgs bosons in the Standard Model as well as in more general theories, the possible production scenarios at the e^+e^- collider LEP[2] are discussed in this section.

2.4.1 Production of the Standard Model Higgs Boson

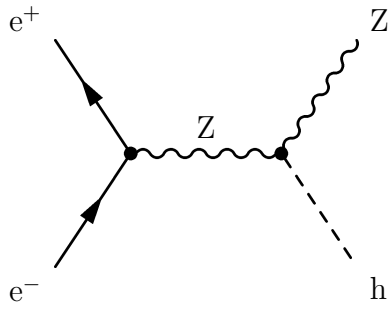

Figure 2.2: *Higgs-strahlung: The Higgs Boson is produced together with a Z Boson*

The main production process of the Standard Model Higgs Boson at LEP energies is the Higgs-strahlung (Figure 2.2). In this process the electron and the positron annihilate into a virtual Z boson which then emits a Higgs boson. The cross section of this process is given by

$$\sigma(e^+e^- \to Zh) = \frac{G_F^2 m_Z^4}{96\pi s}(v_e^2 + a_e^2)\lambda^{\frac{1}{2}} \frac{\lambda + 12m_Z^2/s}{(1 - m_Z^2/s)^2}, \tag{2.57}$$

where $\sqrt{s}$ is the centre-of mass energy, $v_e = -1 + 4\sin^2\theta_W$ and $a_e = -1$ are the neutral current couplings of the electron and $\lambda = (1 - m_h^2/s - m_Z^2/s)^2 - 4m_h^2 m_Z^2/s^2$ is the two-particle phase space function.

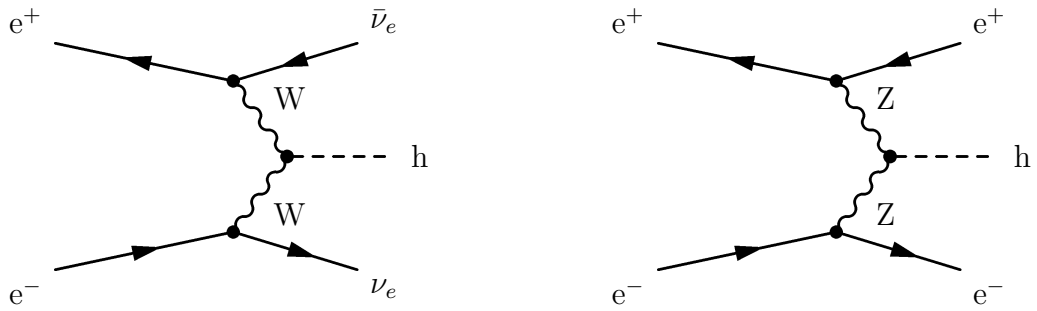

Figure 2.3: *WW and ZZ fusion diagrams: They are suppressed by an additional power of the electroweak coupling with respect to the Higgs-strahlung process.*

By going to higher centre-of-mass energies two more diagrams start to contribute a sizable production rate: the WW and the ZZ fusion diagrams (Figure 2.3). The cross sections for the Higgs-strahlung and the fusion processes are shown as a function of the Higgs mass at $\sqrt{s} = 189$ GeV in Figure 2.4.

[2]The LEP collider is discussed in section 3.1.

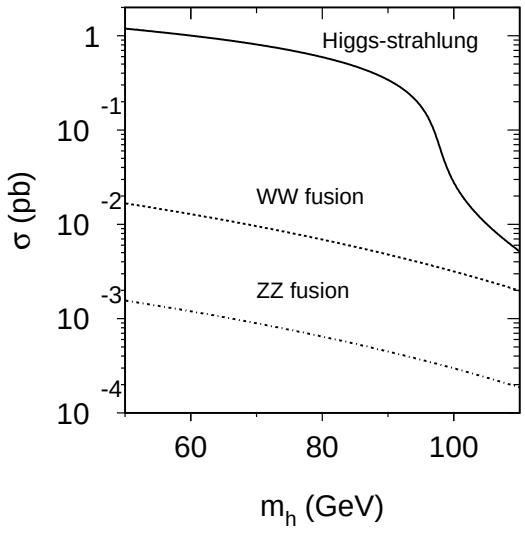

Figure 2.4: *Higgs production cross section at $\sqrt{s} = 189$ GeV. The main production process is the Higgs-strahlung $e^+e^- \rightarrow hZ$.*

2.4.2 Production of Neutral Higgs Bosons in the MSSM

In the MSSM, the Higgs-strahlung process is complemented by the associated pair production $e^+e^- \rightarrow Z \rightarrow hA$ (see Figure 2.5). The CP-odd Higgs boson A can not be pro-

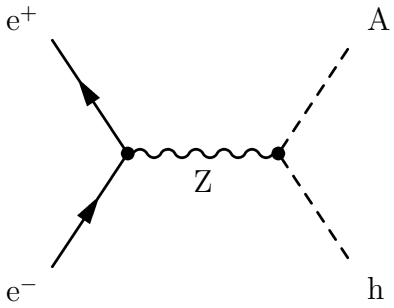

Figure 2.5: *Associated Pair production in the MSSM: The CP-even Higgs boson h is produced together with the CP-odd Higgs boson A*

duced in Higgs-strahlung at tree level [6]. The production of identical bosons via the vertices Zhh and ZAA is forbidden by Bose symmetry. Associated HA production could kinematically occur only in a tiny corner of the parameter space for moderate to large tanβ and with a cross section which is too small to be relevant for the search [16].
The production cross sections for the Higgs-strahlung and the associated pair production can be parametrised in the following way [16]:

$$\begin{aligned} \sigma_{hZ} &= \sin^2(\beta-\alpha)\sigma_{hZ}^{SM} \\ \sigma_{hA} &= \cos^2(\beta-\alpha)\bar{\lambda}\sigma_{hZ}^{SM} \end{aligned} \tag{2.58}$$

where σ_{hZ} is the cross section for the Higgs-strahlung in the Standard Model. The kinematic factor $\bar{\lambda}$ depends on m_h, m_A and $\sqrt{s}$. The range of $\tan\beta$ is expected to lie between $1 \leq \tan\beta \leq m_t/m_b$ [12] (m_t and m_b are the top and bottom quark masses). The upper value of $\tan\beta$ is chosen to keep the bottom Yukawa coupling in the perturbative regime. The lower value results from the fact that the Higgs mass spectrum is symmetric for the

exchange $\tan\beta \longleftrightarrow 1/\tan\beta$ at tree level. However radiative corrections can change this symmetry and values of $\tan\beta$ slightly smaller than one can not be excluded a priori [17]. The cross sections calculated with the HZHA program [18] for two representative $\tan\beta$ values and maximal scalar top mixing are shown in Figure 2.6.

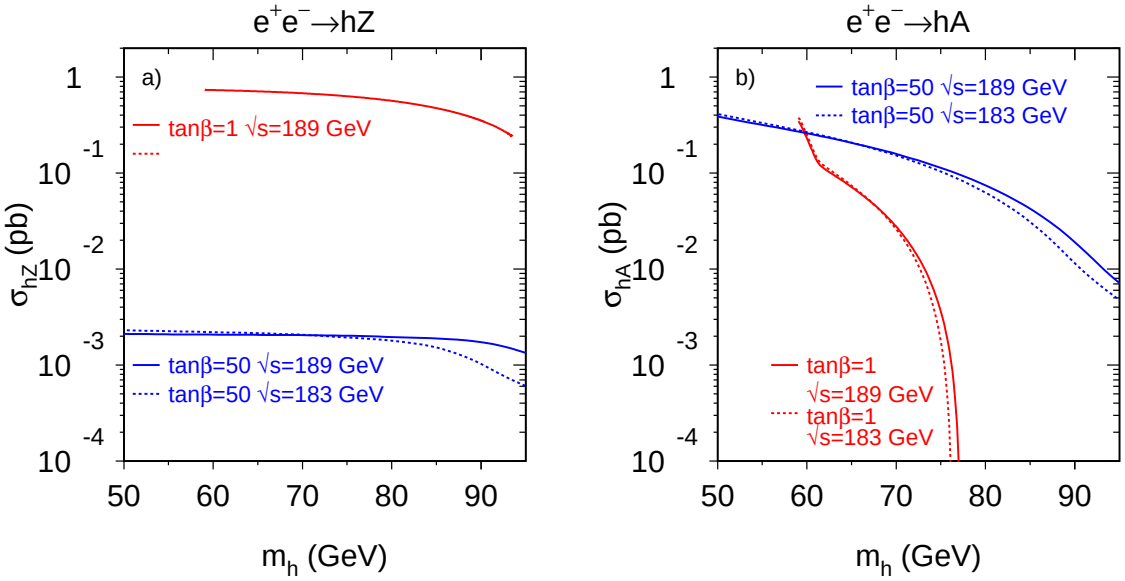

Figure 2.6: *Cross sections for hZ (a) and hA production (b) as a function of the Higgs mass* m_h *for the maximal mixing scenario at* $\sqrt{s} = 183$ *GeV and* $\sqrt{s} = 189$ *GeV. As there are only two free parameters,* m_A *is determined at every* $(m_h, \tan\beta)$ *point. The point* $m_h = 61$ GeV *and* $\tan\beta = 1$ *corresponds to* $m_h + m_A \approx m_Z$*. This causes the sudden change in the hA cross section evolution as for* $m_h \leq 61$ GeV *the hA cross section is dominated by the radiative return to the Z resonance, which can kinematically not contribute beyond this point. For* $\tan\beta = 50$ *this point is at* $m_h \approx 45$ GeV*.*

The influence of the scalar top mixing on the mass of the lightest Higgs boson and on the cross sections is illustrated in Figure 2.7 for two m_A masses. At low $\tan\beta$, where the Higgs-strahlung is the dominant production mode, the differences can become quite large. For high $\tan\beta$ values, the differences in the cross section for the main production mode $e^+e^- \rightarrow hA$ are rather small.

2.4.3 Production of Charged Higgs Bosons

The production of charged Higgs bosons at LEP is possible via s-channel Z and γ exchange (see figure 2.8)[3]. The production cross section at tree level is given by the fol-

[3]In the MSSM the charged Higgs must be heavier than the W boson (see Equation 2.56). There are, in fact, even more stringent lower bounds for general two doublet models of type II from indirect

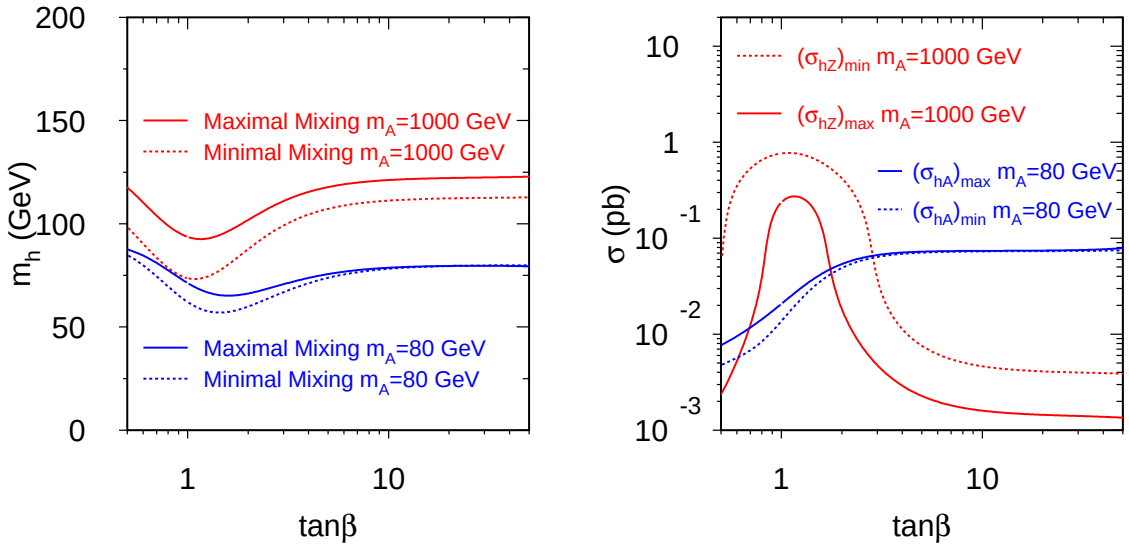

Figure 2.7: *Left: the mass of the lightest Higgs boson as a function of* $\tan\beta$ *for two* m_A *masses and minimal and maximal scalar top mixing. Right: the cross sections* σ_{hZ} *for* $m_A = 1000$ *GeVand* σ_{hA} *for* $m_A = 80$ *GeV.*

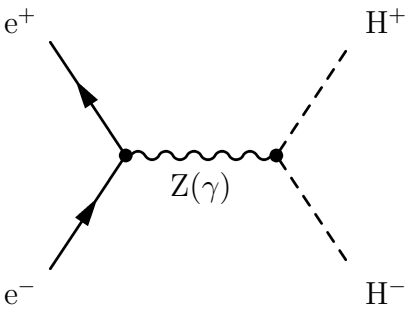

Figure 2.8: *Pair production of charged Higgs bosons at LEP.*

lowing equation [20]:

$$\sigma(e^+e^- \to H^+H^-) = \frac{\pi\alpha^2}{3s}\left[1 - \frac{2\hat{v}_e\hat{v}_H s(s - m_Z^2)}{(s - m_Z{}^2)^2 + m_Z^2\Gamma_Z^2} + \frac{(\hat{a}_e^2 + \hat{v}_e^2)\hat{v}_H^2 s^2}{(s - m_Z^2)^2 + m_Z^2\Gamma_Z^2}\right]\hat{\beta}^3, \quad (2.59)$$

with $\hat{\beta} = (1 - 4m_{H^\pm}^2/s)^{1/2}$, $\hat{v}_e = (1 - 4\sin^2\theta_W)/4\sin\theta_W\cos\theta_W$, $\hat{a}_e = -1/4\sin\theta_W\cos\theta_W$ and $\hat{v}_H = (-1 + 2\sin^2\theta_W)/2\sin\theta_W\cos\theta_W$. As all the parameters apart from the mass of the Higgs boson are well known, the cross section depends only on $m_{H^\pm}$. Figure 2.9 shows the dependence of the cross section on the mass of the charged Higgs calculated with the HZHA program [18] for several centre-of-mass energies.

searches (see section 2.6.2). However, light charged Higgs bosons of type I are possible at LEP energies. If one extends the Higgs sector to more than two doublets, even light charged Higgs bosons of type II could be produced at LEP [19].

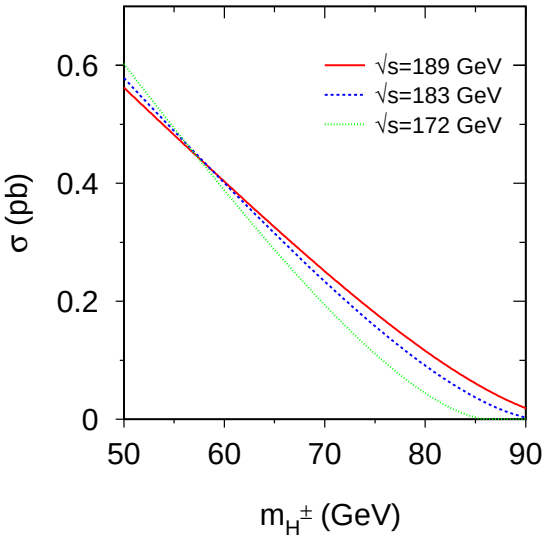

Figure 2.9: *Production cross section for charged Higgs bosons at various centre-of-mass energies. For the calculation the program HZHA [18] was used.*

2.5 Higgs Boson Decay

2.5.1 Decay of the Standard Model Higgs Boson

Once a Higgs boson is produced we need to know how it decays in order to distinguish it from other particles. The Higgs boson is not stable. Its lifetime depends on its mass. The heavier the Higgs boson is, the more decay channels become open. Therefore, the lifetime decreases with increasing mass. The width of the Higgs ($\Gamma = 1/\tau$, τ = lifetime) is predicted to be smaller than 3 MeV for Higgs masses below 100 GeV.

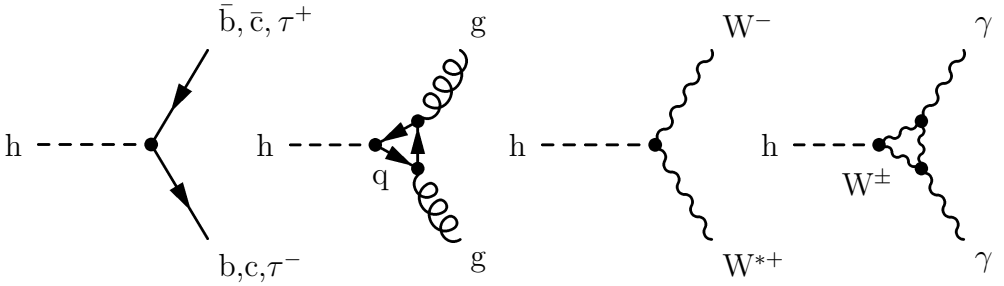

Figure 2.10: *The Higgs decay modes in the LEP2 mass range. The decay into the massless gluons is realised by a heavy quark loop. Higgs decays into photons are possible via quark or $W^{\pm}$ loops.*

Since the Higgs boson generates the masses of the particles through its coupling (Equation 2.31 and 2.43), it decays preferably in the heaviest particles which are kinematically accessible. From the couplings, the partial decay widths of the Higgs can be

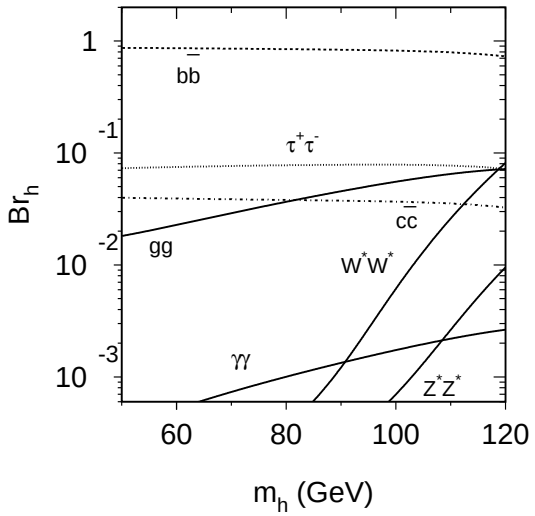

Figure 2.11: *The branching ratios of the Standard Model Higgs Boson with masses accessible at LEP calculated with the HZHA program [18]. The main decay channel is* $\mathrm{h} \to \mathrm{b\bar{b}}$.

derived. The width of the Higgs into leptons is given by [21]:

$$\Gamma_{\mathrm{h}\to\ell^+\ell^-} = \frac{\mathrm{G_F m_\ell^2}}{4\sqrt{2}\pi}\mathrm{m_h}, \tag{2.60}$$

with $\ell = \mathrm{e}, \mu, \tau$. Since the electron and the muon mass are much smaller than the tau mass ($\mathrm{m_e} \approx 0.5$ MeV, $\mathrm{m}_\mu \approx 105$ MeV, $\mathrm{m}_\tau \approx 1777$ MeV), the decay of the Higgs into muons is suppressed by a factor 3×10^{-3} with respect to the decay into tau leptons and the electron decay by a factor 8×10^{-8}.
For the Higgs decay into quarks, the colour factor ($\mathrm{N_C} = 3$) and QCD corrections have to be taken into account [22]:

$$\Gamma_{\mathrm{q\bar{q}}} = \frac{3\mathrm{G_F}}{4\sqrt{2}\pi}\mathrm{m_q^2(m_h)m_h} \cdot \delta(\alpha_\mathrm{s}, \mathrm{m_h}, \mathrm{m_t}, \mathrm{m_q}). \tag{2.61}$$

Here, δ is a function of the strong interaction constant α_s, the quark mass $\mathrm{m_q}$, and the top mass $\mathrm{m_t}$, all to be taken at the mass scale $\mathrm{m_h}$. Due to the colour factor three and the larger b-quark mass the Higgs decay into $\mathrm{b\bar{b}}$ is enhanced by about one order of magnitude with respect to the $\mathrm{h} \to \tau^+\tau^-$ decay. The decay into $\mathrm{c\bar{c}}$ is smaller at currently investigated Higgs masses due to the relatively small mass $\mathrm{m_c}$ of about 0.6 GeV at a scale of 100 GeV [16, 23].
At high masses the Higgs can decay into WW* and ZZ*, however, with a very small branching fraction due to the heaviness of the gauge bosons. The Higgs decay width into virtual W bosons is given by the following equation [16]:

$$\Gamma(\mathrm{h} \to \mathrm{WW^*}) = \frac{3\mathrm{G_F^2 m_W^4}}{16\pi^3}\mathrm{m_h R(x)}, \tag{2.62}$$

where R(x) is a function which depends on the ratio $\mathrm{x} = \mathrm{m_W^2/m_h^2}$. The decay into ZZ* is further suppressed due the mass of the Z boson and the reduced neutral current

couplings with respect to the charged couplings.
At tree level decays into massless gluons or photons are not possible. However, these decays can proceed at one loop level as indicated in Figure 2.10. The branching fractions of the Higgs boson as a function of the Higgs mass are shown in Figure 2.11.

2.5.2 Decay of h and A in the MSSM

As in the case of the SM Higgs, the main decay modes are the decays into $b\bar{b}$ and $\tau^+\tau^-$. For $m_A < 30$ GeV the decay $h \to AA$ is dominant. For the MSSM parameter set discussed here, these masses have been previously excluded [24]. At high $\tan\beta$ the decay of h and A is almost independent of the mixing scenario, whereas at low $\tan\beta$, differences between minimal and maximal scalar top mixing of about 2-5 % are observed.

2.5.3 Decay of Charged Higgs Bosons

The dominant decay modes for charged Higgs bosons with masses accessible at LEP are $H^\pm \to cs$ and $H^\pm \to \tau\nu_\tau$. The decay rate depends on the Higgs-fermion couplings and thus on the type of the underlying model.
For type I models the branching ratios ($Br(H^\pm \to cs)$ and $Br(H^\pm \to \tau\nu)$) are independent of $\tan\beta$ with $Br(H^\pm \to cs) \approx 0.65$ and $Br(H^\pm \to \tau\nu) \approx 0.33$. The remaining branching fraction is made up of the Cabibbo suppressed cb decay [19].
For type II models, the branching fractions depend on $\tan\beta$. The partial decay widths are given by the following equations:

$$\Gamma_{H^\pm \to \tau\nu} = \frac{G_F m_\tau^2 m_{H^\pm} \tan^2\beta}{4\pi\sqrt{2}} \tag{2.63}$$

$$\Gamma_{H^\pm \to cs} = \frac{3 G_F m_{H^\pm} \mid V_{cs} \mid^2}{4\pi\sqrt{2}} \left[m_s^2 \tan^2\beta + m_c^2 \cot^2\beta \right] \tag{2.64}$$

The branching ratios as a function of $\tan\beta$ are illustrated in Figure 2.12.

For Higgs masses above the W-mass, the decay channels $H^\pm \to W^\pm h$ and $H^\pm \to W^\pm A$ are allowed, which, correspondingly, reduce the branching fractions into cs and $\tau\nu$. As we are not yet sensitive to these high masses, these channels have not been considered here.

2.6 Restrictions on Higgs Boson Masses

In this section restrictions on the possible mass ranges of the Higgs bosons, which will be investigated in this thesis, are discussed.

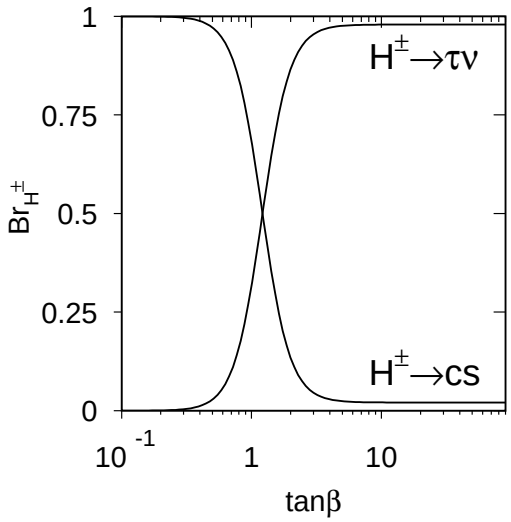

Figure 2.12: *The dependence of the branching ratio of charged Higgs bosons of type II on* $\tan\beta$.

2.6.1 Theoretical Bounds

If the mass of the SM Higgs becomes too large, the couplings to itself and to the gauge bosons become also very large. If one requires that these couplings remain weak enough that perturbation theory can be applied, this implies that $m_h \leq 1$ TeV [25]. This is, however, no absolute bound. Though, there is a more stringent upper limit which arises from the fact that a scalar field theory used to describe the Higgs self-interactions can only be an effective theory (valid over a limited range of energies) if the Higgs self-coupling and hence the Higgs mass is finite [26]. An upper bound of 770 GeV is obtained [27].
Clearly, these limits have practically no impact on the Higgs search at LEP.
A lower bound on the mass of the SM Higgs is obtained by requiring that our universe is in the true minimum of the Higgs potential [28]. If the Higgs mass were very small, then the vacuum state, which is fixed by m_W (see Equation 2.32), could not be the true ground state of the theory [29]. This bound depends upon the scale Λ to which the Standard Model remains valid. This scale must be at least 1 TeV, resulting in the constraint $m_h > 52\ \text{GeV} + 0.64(m_{top} - 175\ \text{GeV})$ [30], which is lower than the existing limits from direct measurements (see section 2.6.3). However, the bound increases monotonically with increasing scale Λ.
In the MSSM the mass m_h is restricted at tree level to be smaller than m_Z, which is altered by radiative corrections. Figure 2.13 shows the theoretically excluded regions for minimal and maximal scalar top mixing in the $\tan\beta$-m_h plane. The lower bound on m_h corresponds to $m_A = 0$.

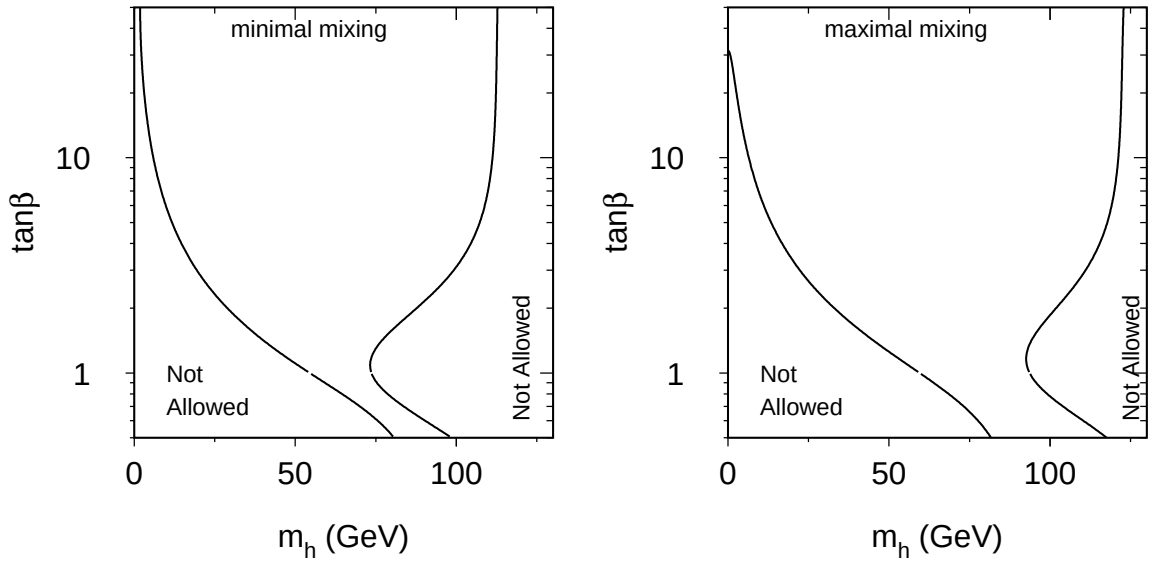

Figure 2.13: *Theoretically inaccessible areas in the* $\tan\beta$-$\mathrm{m_h}$ *plane for minimal and maximal scalar top mixing.*

2.6.2 Limits from Indirect Searches

The electroweak precision measurements performed at LEP and elsewhere can be used to predict the SM Higgs boson mass. This is achieved by fitting the electroweak observables and taking the Higgs as radiative correction into account. The dependence on the Higgs mass is in first order logarithmic which results in a rather large error on the Higgs boson mass. The error on the fit result is currently dominated by the uncertainty on $\alpha(\mathrm{m_Z}^2)$ which arises from the uncertainty of the light quark contribution to the photon vacuum polarisation $\Delta^{(5)}_{\mathrm{had}}(\mathrm{m_Z^2})$ [31]:

$$\alpha(\mathrm{m_Z^2}) = \frac{\alpha(0)}{1 - \Delta\alpha_\ell(\mathrm{m_Z^2}) - \Delta\alpha^{(5)}_{\mathrm{had}}(\mathrm{m_Z^2}) - \Delta\alpha_{\mathrm{top}}(\mathrm{m_Z^2})} \tag{2.65}$$

A serious problem for the determination of $\Delta^{(5)}_{\mathrm{had}}(\mathrm{m_Z^2})$ is the low energy contribution of the five light quarks u, d, s, c and b which cannot be reliably calculated using perturbative QCD. In a first approach, this is solved by an integration of the experimentally measured hadronic cross section of $\mathrm{e^+e^-}$ data and yields $\Delta\alpha^{(5)}_{\mathrm{had}} = 0.02804 \pm 0.00065$ [32]. In a second approach, the cross section of the process $\mathrm{e^+e^-} \rightarrow$ hadrons in non-resonant regions is parametrised using QCD predictions. In the low energy part, additional input from hadronic τ decays is used. This yields $\Delta\alpha^{(5)}_{\mathrm{had}} = 0.02784 \pm 0.00026$ [33].
If one fits now the electroweak data measured by the experiments at LEP and by the SLD collaboration [34] combined with the measurements of $\mathrm{m_W}$ from UA2 [35], CDF [36] and D0 [37], the top quark measurements from CDF [38] and D0 [39] and with the measurements of the neutrino-nucleon neutral to charged current ratios from CCFR and

NuTeV [40], one obtains [41] using $\Delta\alpha^{(5)}_{\rm had} = 0.02804 \pm 0.00065$:

$$\begin{aligned} \log m_h &= 1.96^{+0.27}_{-0.29} \\ m_h &= 92^{+78}_{-45}\ \text{GeV} \end{aligned} \tag{2.66}$$

and using $\Delta\alpha^{(5)}_{\rm had} = 0.02784 \pm 0.00026$:

$$\begin{aligned} \log m_h &= 2.04^{+0.21}_{-0.22} \\ m_h &= 109^{+67}_{-44}\ \text{GeV} \end{aligned} \tag{2.67}$$

This is graphically illustrated in Figure 2.14. The electroweak data clearly prefer a light Higgs which could be well in the reach of LEP. The one-sided 95% confidence upper limit is 245 GeV.

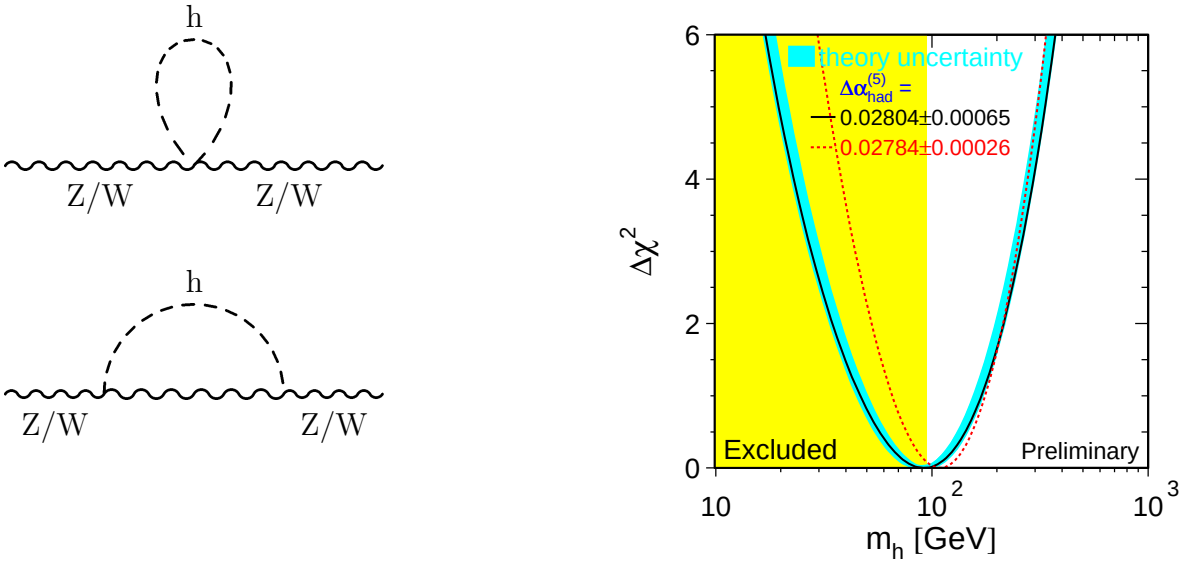

Figure 2.14: *The Higgs enters via loop corrections into the electroweak fits. The Higgs mass can be derived fitting the electroweak observables measured at LEP and at other accelerators.*

There are also constraints from indirect measurements on the mass of the charged Higgs boson. The most stringent constraint on the mass of the charged Higgs boson with Higgs-fermion couplings of type II come from a precision measurement of the process $b \to s\gamma$ performed by the CLEO collaboration at the Cornell Electron Storage Ring (CESR) [42]. Charged Higgs bosons with masses smaller than $m_H^{\pm} = (244 + 63/\tan\beta)$GeV would violate the measured value of the branching ratio of $b \to s\gamma$ via loop corrections. One should note, however, that this bound holds only

for the hypothesis of the SM particle spectrum extended by a two doublet Higgs sector. Once SUSY particles enter, the bound ceases due to cancellations in the loop corrections [43].

Clearly, despite of all the interesting arguments made by theorists or derived from measurements taking into account some underlying theory, the direct measurement remains the most convincing step to confirm or to rule out the existence of Higgs bosons.

2.6.3 Limits from Direct Searches

Before this thesis was started, there was a lower limit on the mass of the Standard Model Higgs boson of 77.5 GeV, which was obtained by the combination of the search results from the 4 LEP experiments [44] up to a centre-of-mass energy of 172 GeV.
In the search for neutral Higgs bosons within the MSSM, individual lower mass limits existed from ALEPH ($m_h, m_A > 62.5$ GeV for $\tan\beta > 1$ [45]), from DELPHI ($m_h > 59.5$ GeV, $m_A > 51.0$ GeV for $\tan\beta > 1$ [46]) and OPAL ($m_h > 59.0$ GeV, $m_A > 59.5$ GeV for $\tan\beta > 1$ [47]), who all exploited data up to a centre-of-mass energy of 172 GeV. L3 had used Z peak data and achieved a limit of $m_h > 42$ GeV for $\tan\beta > 1$ [48]. The CDF collaboration at the $p\bar{p}$ collider TEVATRON at Fermilab (Chicago) recently reported exclusion limits obtained from $p\bar{p} \to b\bar{b}X \to b\bar{b}b\bar{b}$ [49]. They set limits on m_h for $\tan\beta \geq 30$, which go beyond the sensitivity of LEP.
In the search for charged Higgs bosons, ALEPH set a limit at $m_{H^\pm} > 52$ GeV [50], DELPHI at $m_{H^\pm} > 51.5$ GeV for $Br(H^\pm \to \tau\nu) > 0.2$ [46] and OPAL at $m_H^\pm > 52$ GeV [51] all using data up to a centre-of-mass energy of 172 GeV. L3 had used only data at the Z peak and set a limit at $m_H^\pm > 41$ GeV [48][4].
The experiments CDF and D0 at the TEVATRON have searched for charged Higgs bosons in top decays. They set limits in the plane $m_H^\pm$ versus $\tan\beta$. The limits highly depend on the cross section of $t\bar{t}$ production and the top quark mass. The analyses are sensitive for low $\tan\beta$ (< 1) and high $\tan\beta$ (> 40). A detailed discussion can be found in Reference [52].

[4]Note, that the other LEP collaborations have by now updated results exploiting almost all data available at the moment, which will be compared to the L3 results in chapter 10.

Chapter 3

The Experiment

3.1 The e^+e^- Collider LEP

The Large Electron Positron Collider LEP (Figure 3.1), situated at the European Laboratory for Particle Physics (CERN) near Geneva, was constructed to measure electroweak interactions up to a centre-of-mass energy of 200 GeV. LEP has a circumference of about 27 km. Electrons and positrons are accelerated in opposite directions. They are forced to collide in four interaction regions. In these interaction regions the experiments ALEPH [53], DELPHI [54], L3 [55–65] and OPAL [66] are located which allow the registration and the energy and momentum measurement of the particles which arise from the annihilation of the initial e^+e^-pair.
In the first phase (1989-1995), LEP was running at a centre-of-mass energy close to the mass of the neutral heavy gauge boson ($m_Z = 91.187$ GeV). The data collected were used for precise measurements of Standard Model parameters as well as for the search for new particles.
Starting from autumn 1995, the centre-of-mass energy was continuously increased. In 1996 a centre-of-mass energy above the threshold of $W^{\pm}$-pair production was reached, which allowed the precise determination of important parameters such as mass, couplings and branching fractions of the $W^{\pm}$ bosons.
There are two different acceleration schemes used. In the first, electrons and positrons are arranged in 2×4 bunches along the LEP ring. The distance between two bunches, *i.e.* the time difference between two potential collisions is 22 μs. In the second scheme, the so called bunch train regime, the bunches are replaced by trains of up to 4 smaller bunchlets, which have a distance of 250 ns in time. Therefore, collisions may occur more frequently than in the first scheme. For the operation of LEP at the Z peak, the bunch train scheme leads to an increase in luminosity. For running at higher energies, there are usually only 4 bunches used per beam which contain, however, a much higher current. The total current at high energies amounts about 5 to 6 mA at the beginning of a fill. The largest amount of luminosity was delivered by LEP in 1998 at a centre-of-mass energy of 189 GeV. Figure 3.2 shows the averaged integrated luminosity that LEP delivered to the experiments in the years from 1989 to 1998.

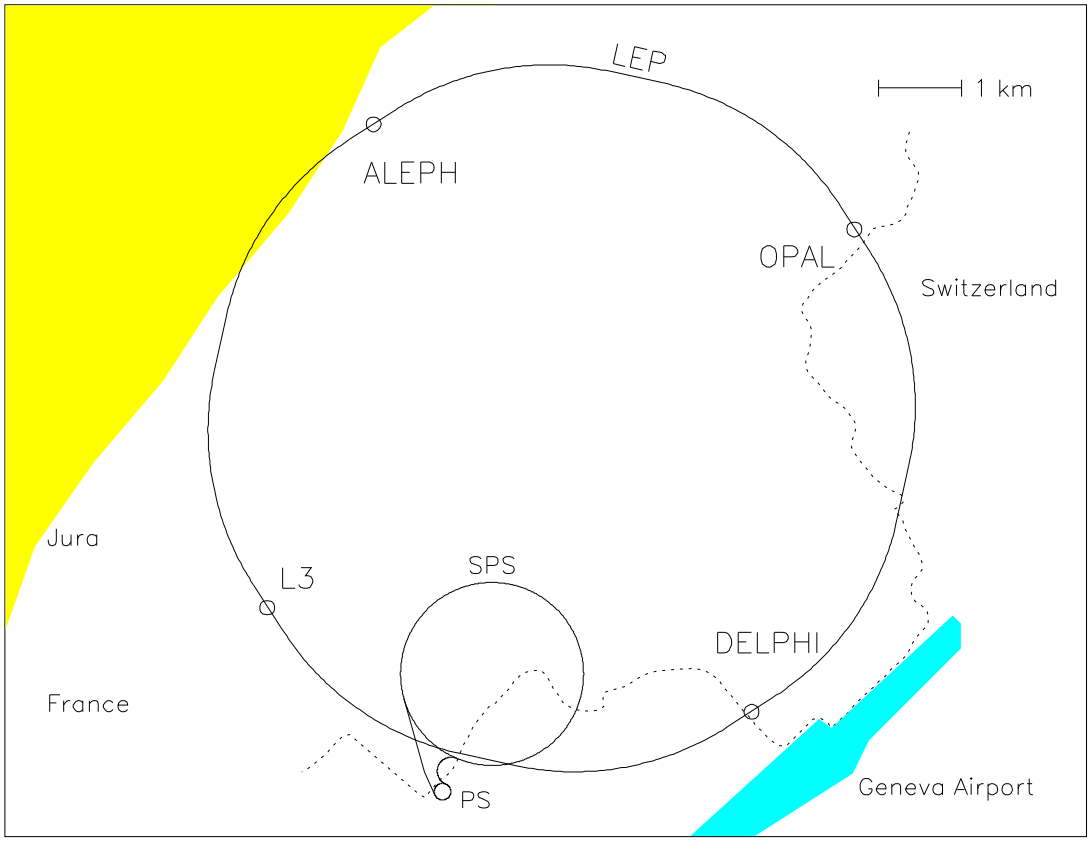

,

Figure 3.1: *The LEP storage ring.*

3.2 The L3 Detector

The L3 detector (Figure 3.3) is a general purpose detector with special emphasis on the precise energy measurement of photons, electrons and muons. The whole detector is installed in a 12 m inner diameter solenoidal magnet, which provides an uniform magnetic field of 0.5 T along the beam axis. The major components of the detector are the following:

- the Silicon Microvertex Detector (SMD)
- the Central Tracking Chambers consisting of a time expansion chamber (TEC) and the z chambers
- the Electromagnetic Calorimeter (BGO)
- the Scintillators

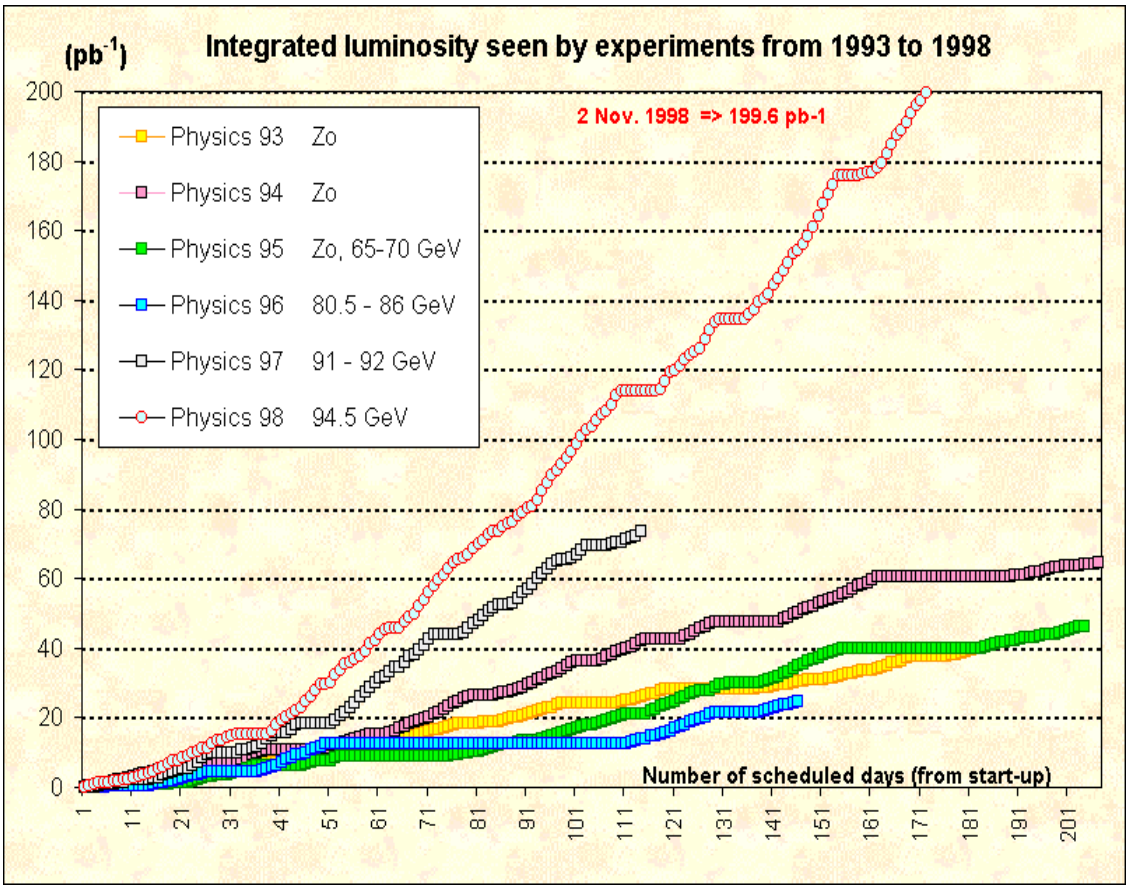

Figure 3.2: *The averaged integrated luminosity delivered by LEP from 1989 to 1998.*

- the Hadron Calorimeter (HCAL)
- the Muon Chambers

The origin of the right-handed coordinate system is in the geometric centre of the detector. The positive z-axis coincides with the direction of the electron beam. The y-axis points vertically upwards and the x-axis towards the centre of the LEP ring. The distance between a point in the x-y plane and the geometric centre of the detector is the radius r. The azimuthal angle between the radius vector $\vec{r}$ and the positive x-axis is denoted with ϕ. The polar angle between the direction of a particle and the electron direction is called θ.

3.2.1 The Silicon Microvertex Detector

The Silicon Microvertex Detector (SMD) [61] is directly attached to the beryllium beam pipe of LEP which has a radius of 5.3 cm. This detector is used to measure charged

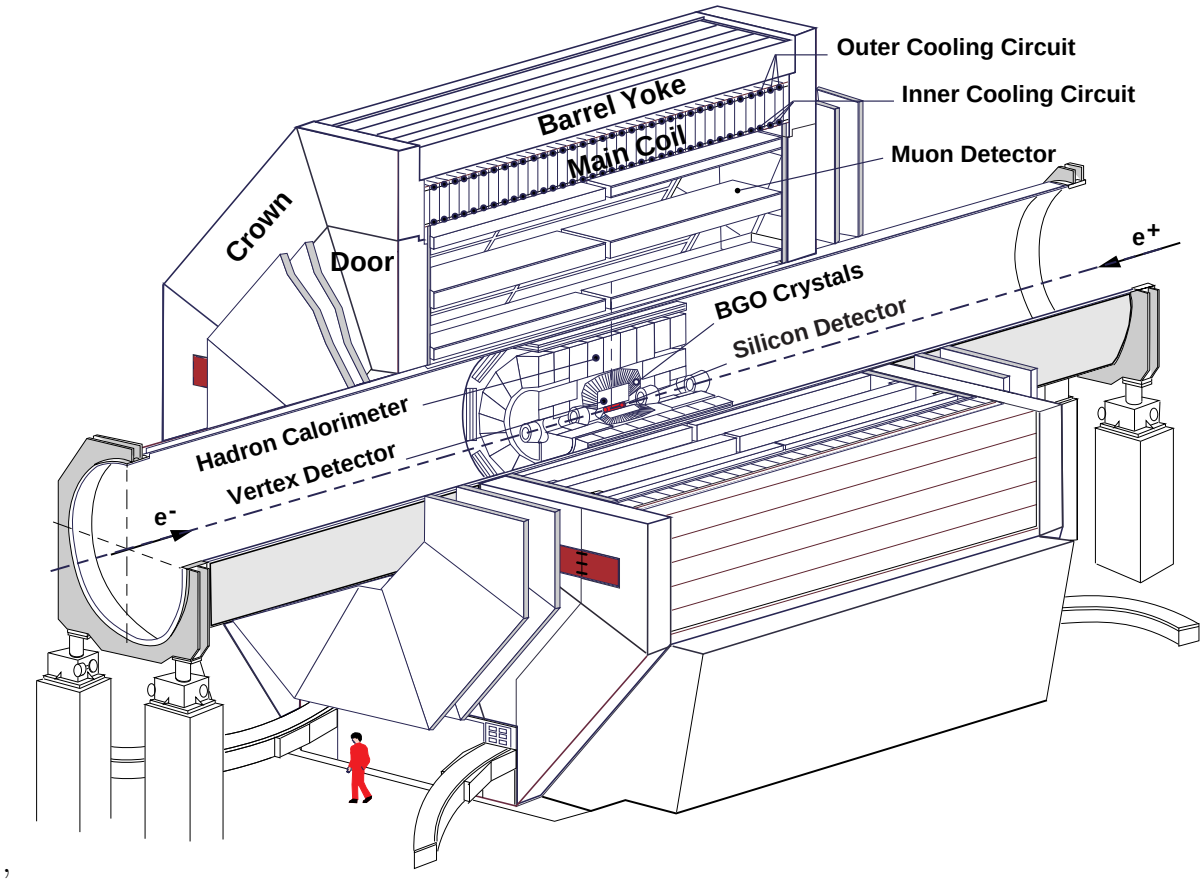

,

Figure 3.3: *The L3 detector at LEP.*

particles at a close distance to the interaction point to resolve possible secondary vertices which arise from the decay of short-lived particles such as hadrons containing b quarks. The SMD is made up of two cylindrical layers. The mean radius of the cylinders amounts 6 cm and 8 cm, respectively. The length of the SMD is 30 cm which yields a polar angle coverage of $22° \leq \theta \leq 158°$. Each of the layers has 12 modules (ladders) which are made up of two electrically independent half-ladders. The half-ladders consist of two double-sided silicon sensors. Each of these sensors is 70 mm long, 40 mm wide and made from 300 μm thick high purity n-type silicon. On one side (junction side) of the sensors there are implantation strips every 25 μm with a readout pitch of 50 μm. They run parallel to the beam axis and allow therefore the determination of the r-ϕ coordinate. On the other side the implantation strips are arranged perpendicular to the junction side strips with a pitch of 50 μm. The readout pitch is 200 μm for $0.53 \leq |\cos\theta| \leq 0.93$ and 150 μm for $|\cos\theta| \leq 0.53$. These strips are used for the z measurement. A resolution of 7.5 μm in r-ϕ and 14.3 μm in z is obtained [67].

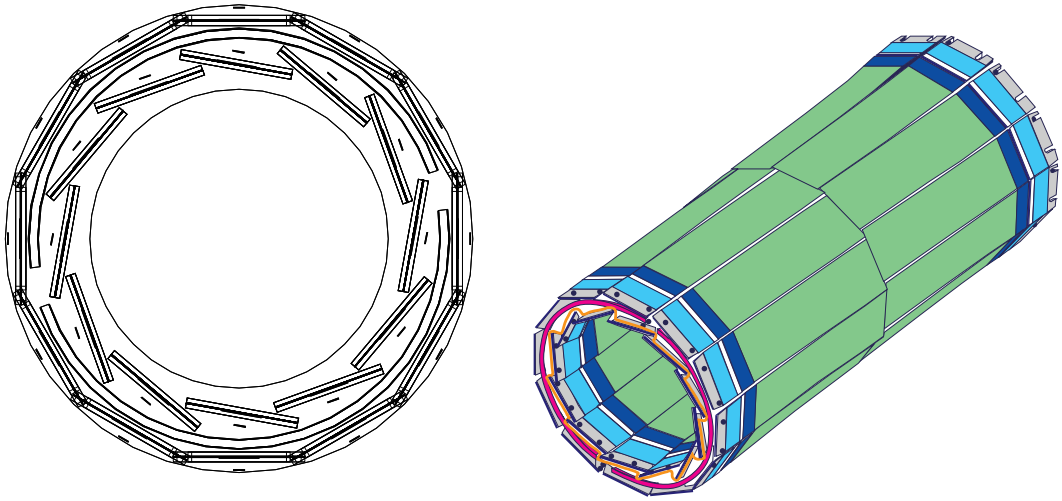

Figure 3.4: *The Silicon Microvertex detector.*

3.2.2 The Central Tracking Chambers

The central tracking chambers allow the reconstruction of charged tracks in r-ϕ and z. For the r-ϕ measurement two concentric drift chambers are used which operate in a time expansion mode. The drift chambers are subdivided into sectors. The anode and cathode wires are drawn in the z direction. The inner drift chamber consists of 12 sectors with 8 anode wires each. The outer drift chamber is subdivided into 24 sectors with 54 wires each. The inner and the outer radius of the TEC is 9.15 cm and 45.6 cm respectively. The length is 126 cm.

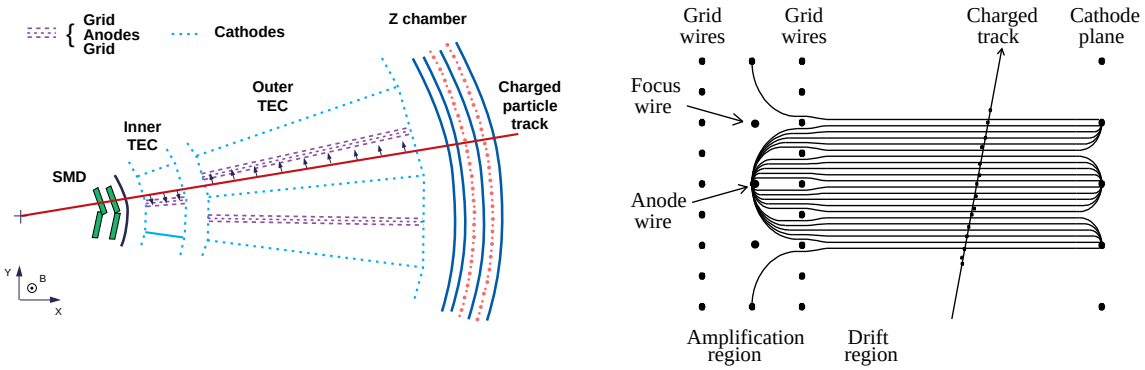

Figure 3.5: *Left: r-Φ view of the central tracker consisting of SMD, TEC and the Z detector. Right: drift field in the TEC.*

The anode planes are surrounded by grid planes which divide the drift regions in areas of different field strength. The small field strength between the cathode and the

grid plane leads to a small drift velocity which results in a very good spatial resolution. In the region of high field strength gas amplification occurs and the electron avalanche is detected by the anodes. In order to resolve the left right ambiguity additional wires in the grid plane are read out. The gas mixture consists of 80 % CO_2 and 20 % Isobutan. The drift velocity is 6 μm/ns. In r-ϕ a resolution of (50-60) μm is obtained. Some anode wires are read out on both sides. These signals are used to obtain a rough z coordinate (resolution some cm) by means of the charge division principle.
Particles with a polar angle between 42° and 138° will pass through the Z chamber [59]. This detector supplements the measurements of TEC and SMD with a z coordinate at r = 50 cm. It consists of two multiwire proportional chambers with cathode readout. The anode wires are aligned in z direction. The two chambers contain two cathode layers each. The cathode layers are made of 240 strips with a pitch of 4.45 mm. The strips of two of the layers are arranged perpendicular to the z direction (z layer) and the strips of the other two layers run under a stereo angle of ±69°. The gas mixture consists of 80 % Argon, 16 % CO_2 and 4 % Isobutan. A charged particle traversing the chamber ionises the gas. The resulting electron avalanche around the anode wire induces image charges on the cathode layers. The relative amount of the signal measured on the individual cathode strips is used for the coordinate determination. The ϕ component of the stereo layer allows the matching of the cluster with a TEC track. The z layers are used for the measurement of the z coordinate. The resolution varies depending on the polar angle. At $\cos\theta = 0$ the resolution is about 200 μm whereas at $|\cos\theta| = 0.74$ the resolution is 1000 μm. The special design of the readout electronics can be used to tag the interacting bunchlet when LEP is operating in the bunch train mode [68].

3.2.3 The Electromagnetic Calorimeter

The electromagnetic calorimeter (BGO) allows the very precise measurement of electrons and photons with energies between 100 MeV and 100 GeV. It consists of bismuth germanate ($Bi_4Ge_3O_{12}$) crystals pointing to the interaction region. The crystals have a length of 24 cm, a front face of 2×2 cm^2 and a rear face of 3×3 cm^2. In the central part of the detector (barrel) there are 7680 crystals. They cover the polar angle $42° \leq \theta \leq 138°$. In the forward-backward region (endcap) of the detector there are 2×1527 BGO crystals which cover the angles $11.6° \leq \theta \leq 38°$ and $142° \leq \theta \leq 168.4°$. The scintillation light of the BGO crystals is collected by two photodiodes which are mounted at the rear face of the crystals. The energy resolution is 5 % at 100 MeV and less than 2 % at energies larger than 1 GeV [69].

The gaps between the barrel and the endcap BGO crystals are filled with lead-scintillating fibre calorimeters (SPACAL) [62]. They consists of 24 modules (bricks) containing a lead structure filled with scintillating fibres. The scintillation light is collected by phototriodes glued on the rear site of the bricks. The resolution of the SPACAL is 15 % at 45 GeV.

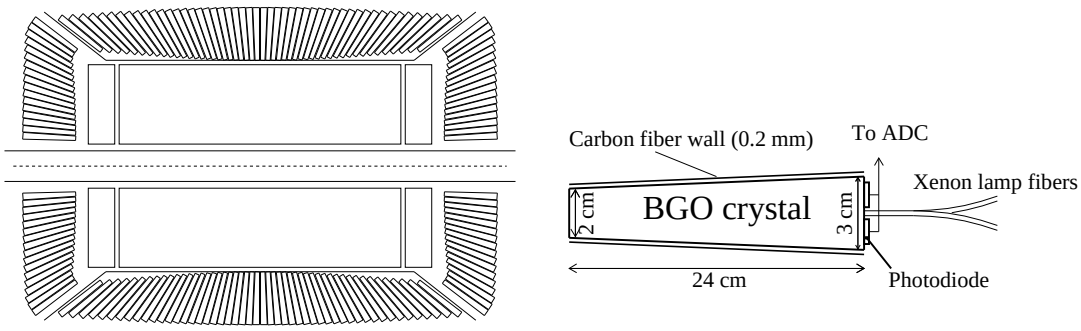

Figure 3.6: *Left: the arrangement of the BGO crystals. The front faces of* 2×2 *cm*^{2} *point to the interaction point. Right: a BGO crystal. The scintillation light is collected by two photodiodes on the rear face.*

3.2.4 The Scintillators

The scintillator system [64] consists of 30 single plastic counters in the barrel and 2×16 in the endcaps. They are located between the electromagnetic and the hadron calorimeter. The time resolution is about 800 ps in the barrel and 1.9 ns in the endcaps. The scintillators therefore allow the discrimination of cosmic muons. If LEP operates in the bunch train mode they are used to tag the bunchlet.

3.2.5 The Hadron Calorimeter

The energy of hadrons is measured in the hadron calorimeter [57]. As in the case of the BGO, it also consists of a barrel and two endcap parts. The barrel calorimeter allows the energy measurement within $35° \leq \theta \leq 145°$ whereas the endcap calorimeters cover the angles $5.5° \leq \theta \leq 35°$ and $145° \leq \theta \leq 174.5°$ in the forward-backward region of the detector.

The central part of the hadron calorimeter contains 9 rings with 16 modules. These modules consist of uranium absorber plates with a width of 5.5 mm interspersed with proportional wire chambers. There are in total 7968 chambers in the barrel part. The two endcaps are each built up of one outer and two inner rings. Each of these rings contains 12 modules.
The material, which a particle arising from the interaction point, has to traverse depends on the polar angle and varies between 6 and 7 nuclear absorption lengths. A muon filter, mounted on the inside wall of the support tube, adds an additional absorption length which suppresses the flow of secondary particles produced in the hadron calorimeter into the muon chambers. The hadron jet energy resolution of the calorimeter is $(55/\sqrt{\mathrm{E}}+8)\%$, where E is measured in GeV. The direction of the jet axis can be measured with a resolution of about 2.5°.

3.2.6 The Muon Detector

The muon chamber system is the largest detector in the L3 experiment [58, 65]. It envelopes all other detector components. It was designed to measure muon momenta with very high precision. The barrel part of the detector covers the polar angle range from 44° to 136°. It consists of two halves with a gap at z=0. Each of the halves is subdivided into octants. As illustrated in Figure 3.7 (left) each octant consists

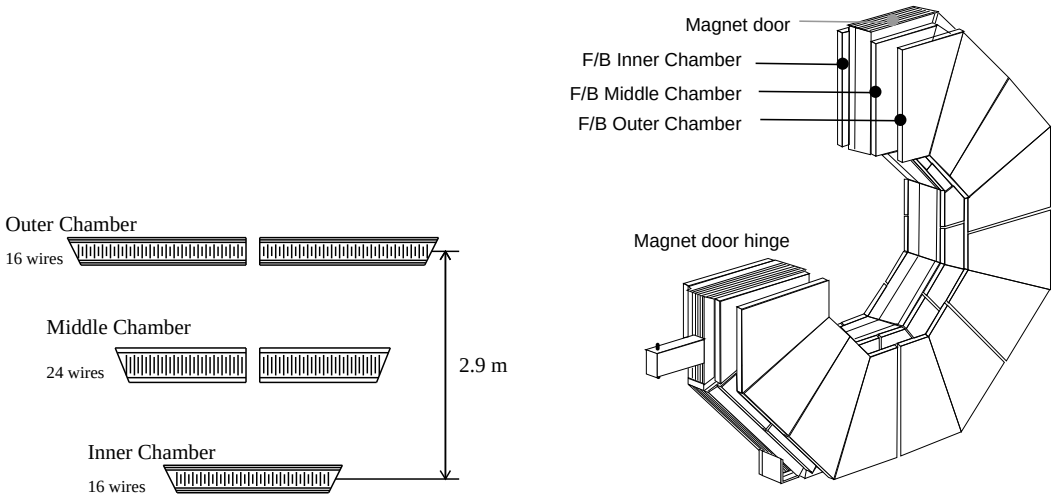

Figure 3.7: *Left: the structure of a muon octant in the barrel. Right: The forward-backward muon chambers.*

of five precision drift chambers (P-chambers) which are arranged in three layers. The outer and inner chambers contain 16 wires each whereas the middle chambers are equipped with 24 wires. In order to determine the z-coordinate of a muon track, there is a set of Z-chambers mounted on the top and the bottom of the inner and the outer layer. The design resolution for muons measured in all 3 layers is $\sigma_{\mathrm{p}}/\mathrm{p} \approx 2.5\%$ at 45 GeV.
The barrel part of the muon detector is complemented with a forward backward spectrometer covering the polar angles $24° \leq \theta \leq 44°$ and $136° \leq \theta \leq 156°$. Three rings consisting of 16 drift chambers are attached to the magnet doors as shown in Figure 3.7. They are triggered by Resistive Plate Counters (RPCs) which are mounted at the rings. The magnet doors are wrapped up with coils producing a toroidal magnetic field of 1.2 T. The resolution depends on the polar angle or, more precisely, whether the inner and middle layers of the barrel detector were also hit by the muon. The momentum resolution varies from 6% at $\theta = 43°$ to 35% at $\theta = 28°$ [70].

3.2.7 The Luminosity Monitor

A precise knowledge of the luminosity is very important for most of the measurements made at LEP. This is achieved by measuring low-angle Bhabha scattering and comparing the measured rate with a precise theoretical calculation [71]. The L3 luminosity

monitor [63] consists of two electromagnetic calorimeters complemented with two silicon trackers (SLUM). These two sets are located at z = ±2.7 m (Figure 3.8) and cover the polar angles 24.93 mrad ≤ θ ≤ 69.94 mrad.

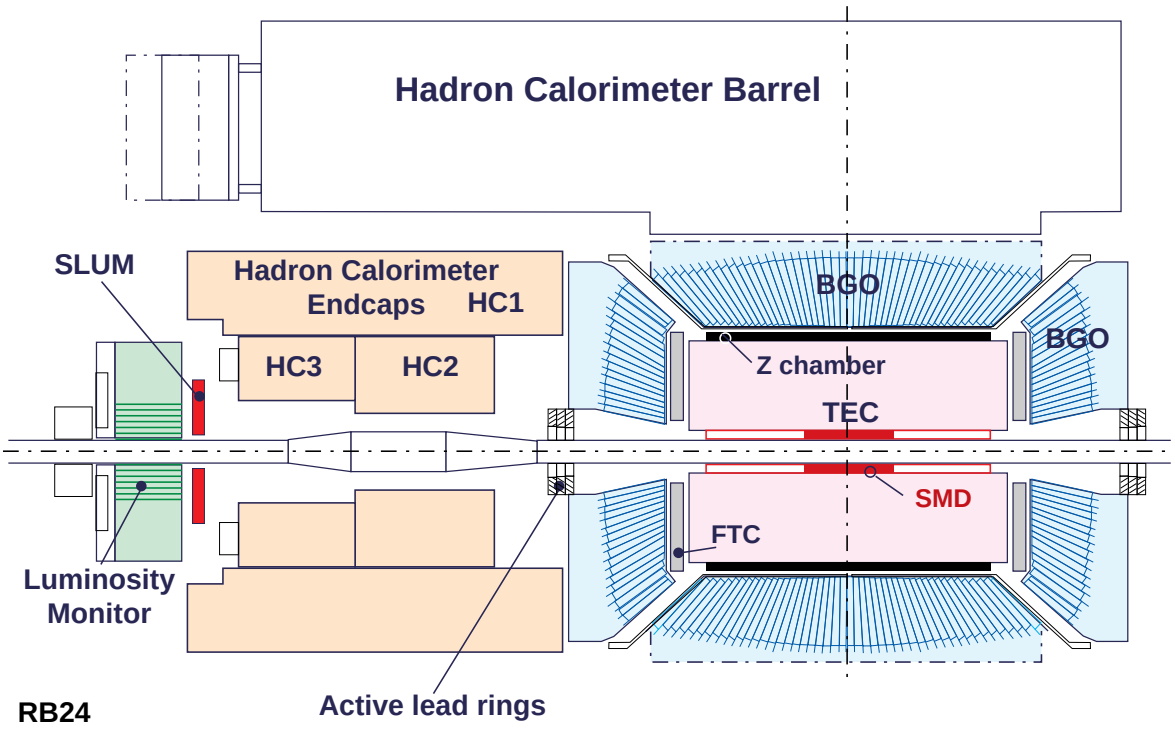

Figure 3.8: *The luminosity is measured by using low angle Bhabha scattering.*

3.2.8 The Trigger System

An efficient trigger system is needed to separate interesting physics events from those events which just contain energy deposits caused by beam-gas, beam-wall interactions, synchrotron radiation or detector noise. All subdetectors are prepared for data taking by the beam crossing signal (≈ 1.7 μs before the electron and positron bunches are expected to collide).
The number of events written to tape is reduced in 3 steps. The first step (level-1 trigger) takes individual information from the subdetectors into account. These are track information from the TEC (inner and outer TEC triggers), energy deposits in the calorimeters (energy trigger), scintillator hits (scintillator trigger), energy deposits in the luminosity monitor (luminosity trigger) and tracks in the muon chamber (muon trigger). If one of these triggers has fired, the event is passed to the level-2 trigger, where more time is available to make a first cross check between the individual triggers. This removes already a large fraction of the background events mentioned above. If an event was ac-

cepted by more than one trigger, the event is not rejected. At the trigger level-3 the full information of an event is available. The correlation between the individual subdetector information is exploited and tighter requirements on the individual decisions can be made. Events with multiple positive decisions on trigger level-1 or with luminosity trigger are not rejected. All events passing the trigger level-3 decision are written to tape.

Chapter 4

Data Sample and Monte Carlo Simulation

In chapter 2 the production and decay of the various kinds of Higgs bosons were discussed. The world of particle physics is, however, much richer. There are many physics processes resulting from e^+e^-annihilations. These processes (background) have to be considered in the search for our signal if they either have the same or a similar signature.
This chapter describes the data sample, the most relevant background sources and the main strategy, which is used by experimental high energy physicists to understand what kind of physics they have in their data sample.

4.1 Data Sample

Since autumn 1995, LEP has operated at energies above the Z-peak. This data taking period is referred to as LEP2. Table 4.1 summarises the centre-of-mass energies at which LEP was operated in the years from 1995 to 1998 and quotes the integrated luminosities taken by L3. For the search for charged Higgs bosons all data listed in Table 4.1

Year	$\sqrt{s}$ (GeV)	$\mathcal{L}$ (pb^{-1})
1995 + 1997	130.1	6.1
1995 + 1997	136.1	5.9
1996	161.3	10.8
1996	172.1	10.2
1997	182.7	55.3
1998	188.6	176.4

Table 4.1: *Centre-of-mass energies at LEP2 [72] and integrated luminosities taken by L3 until 1998. The error on the energy is below 50 MeV and the luminosity error is well below 1%.*

were exploited, whereas for the search for neutral Higgs bosons only the data taken

at 182.7 GeV and 188.6 GeV were used. The other centre-of-mass energies were already covered by previous L3 analyses and do not contribute to Higgs masses that are currently probed.

4.2 Physics Processes at LEP2 Energies

At LEP2 energies we have many interesting physics processes, as for instance, the two-fermion interactions $e^+e^- \to e^+e^-(\gamma)$, $e^+e^- \to \mu^+\mu^-(\gamma)$, $e^+e^- \to \tau^+\tau^-(\gamma)$ and $e^+e^- \to q\bar{q}(\gamma)$. The measurements of their cross sections and asymmetries are used for the verification of Standard Model parameters, but are also interpreted within more general models. For the analyses described in this thesis, these processes are background. The di-lepton production can be easily rejected by making requirements on the multiplicity of the events, *i.e.* requiring a minimum number of tracks and/or calorimetric clusters. The process $e^+e^- \to q\bar{q}(\gamma)$ (Figure 4.1) remains, however, a relevant background source. After the annihilation of an electron and a positron into a virtual Z or

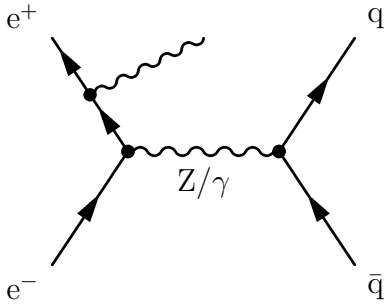

Figure 4.1: *The background process* $e^+e^- \to q\bar{q}(\gamma)$ *. In the case of initial state radiation the event is unbalanced if the photon escapes unobserved the detector.*

γ, a quark and an antiquark arise. They hadronise and we observe usually two jets in the detector. The radiation of gluons by the quark or antiquark can lead to additional jets. It is also possible, in the case of b or c quarks, that we have inclusive leptons from the b- or c-hadron decay. In the case, where the initial state electron and/or the positron radiate photons, it is possible to reduce the effective centre-of-mass energy in such a way that a real Z boson is produced instead of a virtual. This is called the **radiative return to the Z**. The photons escape undetected, in most of these cases, down the beam pipe. Therefore, these events are characterised by an energy imbalance where the missing momentum vector points along the beam direction. For the generation of $e^+e^- \to q\bar{q}(\gamma)$ events the Monte Carlo program PYTHIA [73] was used.
The production of W-pair events is realised in lowest order by three Feynman diagrams, the s-channel γ and Z boson and the t-channel ν_e exchange (see Figure 4.2). The W bosons can decay into a quark-antiquark pair, for example $W^+ \to u\bar{d}$ or $c\bar{s}$ or into a lepton-antilepton pair, $W^- \to \ell^-\nu_\ell$ ($\ell = e, \mu, \tau$)[1]. For the generation of the WW background the Monte Carlo generator KORALW [74] was used which takes the three Feynman diagrams presented in Figure 4.2 into account. Contributions from other diagrams are small, which is verified using the four-fermion generator EXCALIBUR [75].

[1]The charge conjugated decays are also possible.

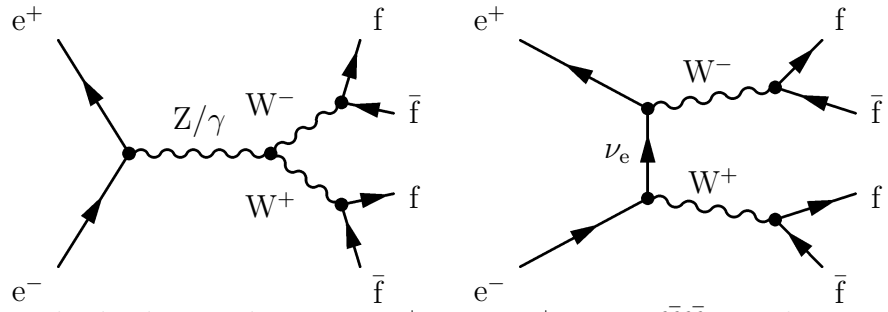

Figure 4.2: *The background process* $e^+e^- \to W^+W^- \to f\bar{f}f\bar{f}$ *. In lowest order three diagrams contribute to the cross section.*

Neutral current four-fermion reactions can also be generated using EXCALIBUR. This program is used for the measurement of the resonant ZZ production cross section which will be described in chapter 9. For the background modelling in the Higgs search PYTHIA was used taking into account the NC02 approximation (in the following referred to as ZZ) and single Z production (in the following called Zee). ZZ background is especially severe for the SM Higgs search as it may lead to the same final states as hZ production and is kinematically very similar (see Figure 4.3). There is one more relevant

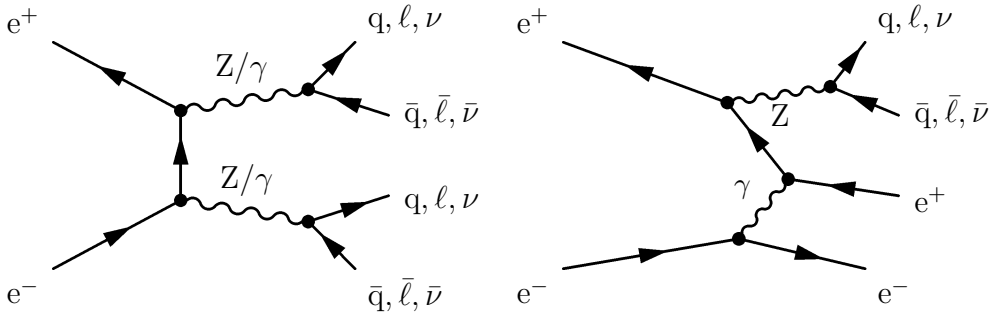

Figure 4.3: *Examples for ZZ and Zee production.*

four-fermion process, which is referred to as the two photon interaction because of the virtual exchange of two photons (Figure 4.4). This process has the highest cross section at current LEP energies, but has only little impact on the Higgs search. The electron and positron get slightly scattered in this process loosing only a small fraction of their initial energy before they vanish undetected through the beampipe. The fermion pair which is observed in the detector has, therefore, a small energy and can be easily separated from the Higgs signal. For the generation of two photon events the program PHOJET [76] was used. Table 4.2 shows the cross sections of the background processes at a centre-of-mass energy of 189 GeV.

Higgs production cross sections and branching ratios were calculated using the HZHA program (examples are shown in chapter 2). The efficiency studies were performed using

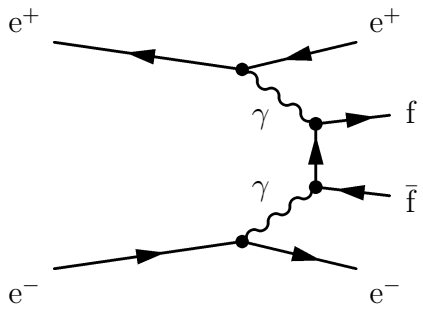

Figure 4.4: *Two photon interaction*

SM processes	cross section (pb)	Generator	Events
$e^+e^- \to e^+e^-q\bar{q}$	15.6×10^3	PHOJET	5.94×10^6
$e^+e^- \to q\bar{q}(\gamma)$	98.3	PYTHIA	2.93×10^6
$e^+e^- \to WW$	16.5	KORALW	2.95×10^5
$e^+e^- \to Zee$	3.35	PYTHIA	2.95×10^4
$e^+e^- \to ZZ$	0.973	PYTHIA	1.96×10^5

Table 4.2: *Standard Model processes, cross sections, generators, and number of generated events, at $\sqrt{s}$ =189 GeV, used in the analysis.*

the PYTHIA generator.

4.3 Simulation and Reconstruction

As already discussed in the previous section, the physics processes are modelled using Monte Carlo event generators. At the end of the Monte Carlo event generation, we have a number of particles with their energy-momentum vectors. In the next step the detector response on these particles is simulated using the GEANT and the GHEISHA programs [77] which take into account the effects of multiple scattering, energy loss and showering in the detector as well as the interaction with the magnetic field. At the end of the simulation, the events are available in the same format as the real data recorded in the detector. This is the digitised information of the detector response for the individual subdetectors.
Simulated and real data events are then reconstructed using the same reconstruction code which combines the individual subdetector information, such as wire hits or crystal amplitudes into tracks and energy clusters. For the simulated events, time-dependent imperfections such as dead wires or crystals are taken into account in order to make the simulation as realistic as possible.

Chapter 5

Search for the Standard Model Higgs Boson

In chapter 2 the production and the decay of the Standard Model Higgs boson at LEP2 energies was discussed in detail. In this thesis the following channels have been analysed:

- the $hZ \to b\bar{b}e^+e^-$ channel
- the $hZ \to b\bar{b}\mu^+\mu^-$ channel
- the $hZ \to b\bar{b}\tau^+\tau^-$ and the $hZ \to \tau^+\tau^- q\bar{q}$ channels

For each of these channels a dedicated selection has been performed putting emphasis on the particular signature of the given final state. However, there is a main strategy which was followed for all the investigated channels. The general analysis procedure and special analysis techniques are described in section 5.1. After that, the individual selections are described. They are the same for the 183 GeV and the 189 GeV data. The numbers and figures shown refer to the data taken at $\sqrt{s} = 189$ GeV. The results of the analysis of the 183 GeV data are presented in appendix A.

5.1 Analysis Method

The analyses are performed in 3 steps: first a selection based on lepton identification and kinematic variables is performed. The kinematic variables and their cut values are chosen in such a way that they allow large sensitivity over a wide Higgs mass range (typically from 50 GeV up to the kinematic limit). Then, a kinematic fit is performed which takes into account energy and momentum conservation as well as the constraint that the lepton pair (jet pair in the case of the $hZ \to \tau^+\tau^- q\bar{q}$ channel) arises from a Z decay. The reconstructed Higgs mass m_{rec} obtained from this fit is finally combined with the b-tag information (except for the $hZ \to \tau^+\tau^- q\bar{q}$ channel, where m_{rec} is directly used) into a discriminant variable which is used to test a given Higgs mass hypothesis. The discriminant variable is described in detail in section 5.1.5. The advantage of using a mass dependent variable rather than comparing the total number of observed candidates

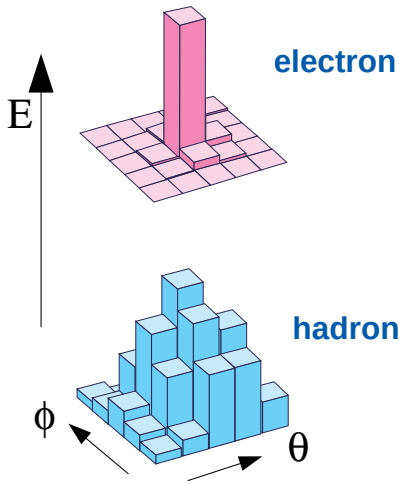

Figure 5.1: *The typical shower shapes of electrons(photons) and hadrons in the BGO*

to the total number of expected background and signal events relies on the very good mass resolution of m_{rec} (typically 1.8 to 3.5 GeV depending on the decay channel). Although, the total number of expected background events can be rather large, only a small number will effect a given Higgs mass hypothesis. The analysis performance, *i.e.* the expected signal-to-background ratio depends on the separation power of the final discriminant variable between signal and background.

5.1.1 Lepton Identification

Electrons

Electrons[1] (and photons) are identified by a narrow electromagnetic shower in the BGO. The energy is deposited in only a small number of adjacent BGO crystals around the impact point of the particle. Hadrons cause a much wider shower shape (see Figure 5.1). The coordinate of the particle (bump) is calculated using a centre-of-gravity method which takes the energy deposition of adjacent crystals into account. In order to evaluate the electromagnetic origin of the energy deposition, two parameters are introduced, $E_{9/25}$ and χ^2_{em}. $E_{9/25}$ is the ratio of the energy sums of a 3×3 and a 5×5 crystal map around the central crystal of the bump. In order to account for the energy leakage of an electromagnetic shower, the measured values of E_9 and E_{25} are corrected:

$$\begin{aligned} E_{9cor} &= \frac{E_9}{b_0 \cdot E_1/E_9 + b_1} \\ E_{25cor} &= \frac{E_{25}}{c_0 \cdot E_1/E_{25} + c_1}, \end{aligned} \tag{5.1}$$

where E_1 is the energy of the central crystal and b_0, b_1 , c_0 , c_1 are correction constants which depend on the different regions in the BGO. For electrons and photons the ratio

[1] In the text, electrons are taken to refer to both electrons and positrons.

E_{9cor}/E_{25cor} is close to one. For hadrons it is usually much smaller.
The second parameter is χ^2_{em}, which is also a measure of the electron(photon)-likeness of the energy deposition. It is calculated taking into account the shower profile in a 3×3 crystal map around the most energetic crystal and comparing it to an electron reference profile obtained in test beam measurements.
Photons and electrons look alike in the BGO. Since electrons, however, interact with the gas in the central tracking chambers because of their electric charge, they are characterised by tracks which point to the bump measured in the BGO. The matching of the track and the bump can be used to distinguish between electrons and photons.
The strategy in this thesis is to find a good balance between lepton identification and kinematic cuts in order to keep the signal efficiency high while suppressing the background by a large factor. If an electron impacts on a non-homogeneous region of the detector, the shower shape may deviate from a typical electromagnetic one. Furthermore, we may loose the track due to mismatches in the reconstruction or due to insensitivity of the TEC for tracks which are produced at small angles with respect to the beampipe.
In order to minimise the sensitivity loss due to badly reconstructed electrons, two electron definitions are used: a) a good electron (category I) and b) a loose electron (category II). The two definitions will be used in the different selections depending on the particular background conditions of the investigated channel.

Category I electron:
Electrons of this category must fulfil tight requirements on the electromagnetic shower shape in the BGO, on bump-track matching and on isolation.
The energy ratio E_{9cor}/E_{25cor} must be at least 0.98 and χ^2_{em} must be smaller than 35. The energy measured in the HCAL behind the bump should not exceed 20% of the bump energy measured in the BGO (in the following referred to as E_{HCAL}/E_{BGO}). There is a track required to be matched to the bump within 20 mrad in ϕ and 200 mrad in θ. As isolation criteria no additional tracks are allowed within a 100 mrad cone and no additional energy deposition in excess of 5 GeV within a 10 degree cone around the bump. Distributions for E_{9cor}/E_{25cor} and the track-bump matching in $\Delta\phi$ are shown in Figure 5.16 (a-b) for a reference sample $e^+e^- \to e^+e^-$.

Category II electron:
Two types of objects qualify for this category: a) those with an electromagnetic shower shape fulfilling $E_{9cor}/E_{25cor} \geq 0.93$ and $E_{HCAL}/E_{BGO} \leq 0.2$ (no requirements on χ^2_{em}, matching and isolation are made) and b) objects with energy depositions of at least 2 GeV in the calorimeters where the bulk of the energy is concentrated in a 10 degree cone and exactly 1 track matched within a 10 degree cone around the centre of the energy deposition.
Clearly, these loose requirements open a gate for background processes such as radiative $q\bar{q}(\gamma)$ and $WW \to qq\ell\nu$ ($\ell = e, \tau$). As will be shown in section 5.2 these processes can be suppressed by kinematic cuts, mass information and b-tagging.

Muons

Besides neutrinos, muons are the only particles which can penetrate the whole detector. They are characterised by tracks in the TEC and the muon chambers matching a minimum ionising signature in the calorimeters. The typical energy loss of muons in the BGO is about 200 to 300 MeV and in the hadron calorimeter about 2-3 GeV [78]. This energy is localised in a very narrow cone involving only a small number of contiguous clusters.
As in the case of the electrons, two categories of muons are used in the analysis.

Category I muons:
Muons of this category are observed by a track in the muon chambers. When this track is traced back to the interaction point it should match a track in the TEC within 100 mrad in ϕ. The matching requirements for θ depend on the z information which is included in the TEC track fit. For tracks with SMD and TEC-Z chamber information, it is 50 mrad, and for tracks that contain only SMD information, 100 mrad. Otherwise, a matching of 200 mrad is required. The closest approach of the TEC track to the interaction point in the plane perpendicular to the beam pipe should not exceed 10 mm in order to suppress cosmic ray contamination. Figures 5.16 c) and d) show the energy distributions in the barrel for triplets (the muon was detected in all 3 muon chamber layers) and doublets (the muon was detected in only 2 layers).

Category II muons:
Muons that fail the above requirements can still be selected if the energy deposition in the calorimeters can be interpreted as arising from a minimum ionising particle (MIP). An object is accepted for this category if the energy is contained in a small number of clusters, matched to exactly one TEC track within a 10 degree cone. The calorimetric energy deposited between 10 and 30 degrees around the reconstructed direction is not allowed to exceed 10% of the energy deposited within a 10 degree cone.

Taus

Tau leptons are short living particles with a lifetime of about 2.9×10^{-13} s, which corresponds to a flight length of ≈ 2 mm. Hence, only the visible decay products are observed in the detector. They carry part of the initial tau energy. The other part goes into one or more neutrinos which escape undetected. Tau leptons decay in $\approx 85\%$ of the cases into one charged particle accompanied by neutral decay products (1-prong decay) and in 15 % of the cases in three charged particles (3-prong decay). The branching ratios $\tau \rightarrow e\nu\nu$ and $\tau \rightarrow \mu\nu\nu$ amount to $\approx 18\%$ each [79][2].
Tau leptons are identified as category I electrons or muons defined above or as low multiplicity jets with 1 or 3 tracks and unit charge. The charge is defined by summing up the signs of the track curvature assuming unit charge for a track. Only tracks within a 10 de-

[2]These decays introduce cross efficiencies between the electron and the tau channels and the muon and the tau channels. The cross efficiencies are taken into account as described in section 5.5.

gree cone are considered. The multiplicity of the jet is defined by limiting the number of calorimetric clusters between 0 and 10 degree to 8 and between 10 and 30 degree to 5. Furthermore, the ratio of the calorimetric energy deposited between 10 and 30 degree must not be larger than 30% of the energy observed between 0 and 10 degree around the reconstructed direction of the decay particles. This energy ratio is referred to as E_{30}/E_{10}. Figures 5.16 e) and f) show the number of tracks in a 10 degree cone and the energy ratio E_{30}/E_{10} for a reference sample $e^+e^- \to \tau^+\tau^-$.

5.1.2 B-tagging

Higgs bosons with masses $m_h < 2 \cdot m_W$ decay predominantly into a pair of b-quarks. Therefore, one of the most important analysis steps in the search for Higgs bosons in

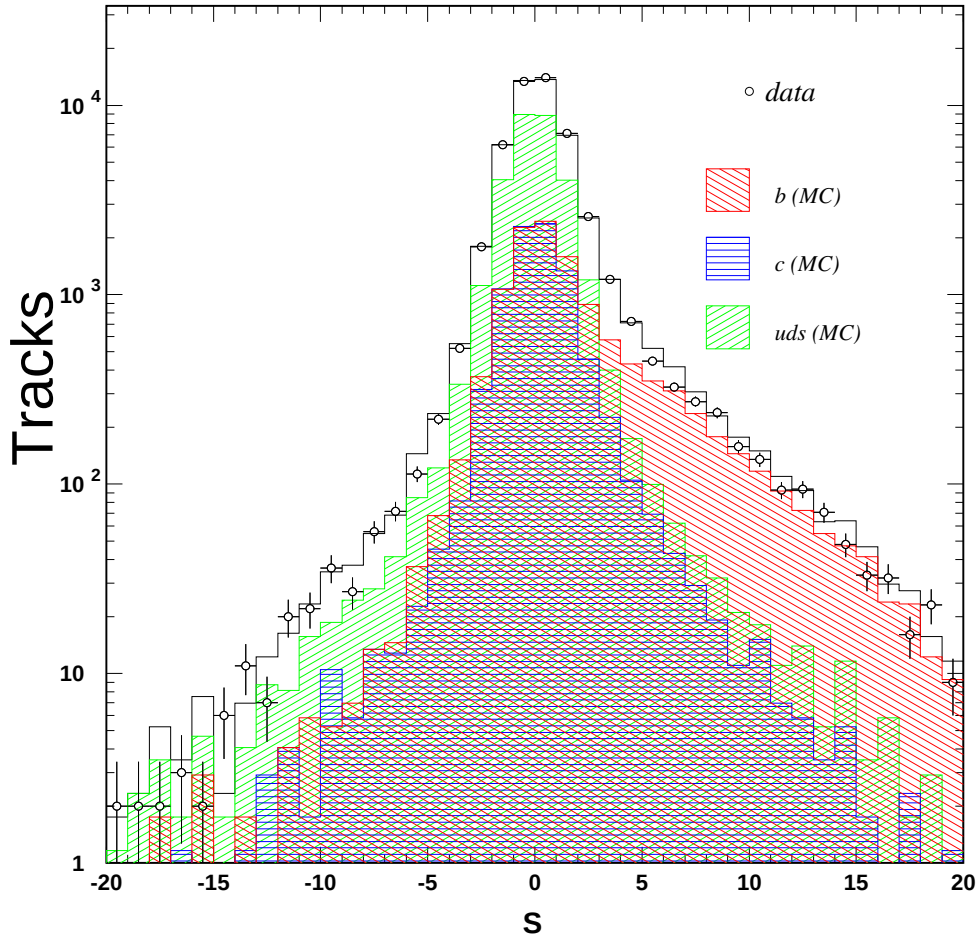

Figure 5.2: *The decay length significance for tracks [80].*

this mass range is the tagging of b-quarks. B-tagging is mainly based on the lifetime information, that jets containing b-quarks, carry. The typical lifetime of hadrons containing b-quarks is about 1.5×10^{-12} s [79]. Hadrons without b-quarks live either shorter (c-hadrons $\approx 0.5 \times 10^{-12}$ s) or longer (uds-hadrons $> 10^{-8}$ s). The latter decay far away from the interaction point. Apart from the lifetime, there are other variables which can be used to distinguish b-hadrons from others. Those are the charged particle multiplicity and the mass at the decay point, tertiary decay vertices from cascade decays, different jet shapes and prompt leptons from semileptonic b decays. The L3 b-tagging technique takes advantage of all these characteristics. A detailed description of the b-tagging procedure can be found in References [81] and [80].
The potential lifetime information of jets is evaluated by checking the compatibility that all tracks originate from the primary vertex. This is achieved by calculating first the crossing point of every track with the jet axis. The distance between this point and the primary vertex is denoted as decay length L. This decay length is signed with the convention that it is accounted positive if the crossing point lies along the jet-axis in the supposed direction of flight of the original b-quark. Otherwise, it is accounted negative. If one plots the significance $S = L/\sigma_L$ for all tracks, one expects an asymmetric distribution for events with b-quarks. The positive side of the distribution is enhanced due to the fact that not all tracks originate from the primary vertex (see Figure 5.2). The negative side of the distribution is fitted with an arbitrary function. The resolution function R(s) obtained from this fit is then used to calculate track probabilities P(S) for the positive side. The probability that a track with a significance larger than s originates from the primary vertex is then:

$$P(s) = \frac{\int_s^\infty R(s')ds'}{\int_0^\infty R(s')ds'}. \tag{5.2}$$

The individual track probabilities are weighted depending on the decay length resolution and their momenta and are finally combined into a weighted probability P_n^w, where n denotes the number of tracks which are included. A detailed discussion on the derivation of this quantity can be found in Reference [80]. Jets with b-quarks will have low values in P_n^w. The region near zero is therefore expanded by defining a discriminant:

$$B_n^w = -\log P_n^w. \tag{5.3}$$

To further improve the b-tag performance, a neural network [82] is used. It uses apart from the discriminant above (which is the most powerful variable), information about possibly reconstructed secondary vertices and their track multiplicity, the invariant masses at the primary and secondary vertices, momenta of inclusive leptons and jet shape variables such as the boost and the sphericity [83]. The neural network output spectrum for calibration data taken at the Z peak in 1997 can be seen in Figure 5.3.

5.1.3 The DURHAM Jet Clustering Algorithm

Cluster algorithms are used to combine energy deposits in the detector into larger units in order to reveal the physical origin of an event. In L3 we have access to the momenta of

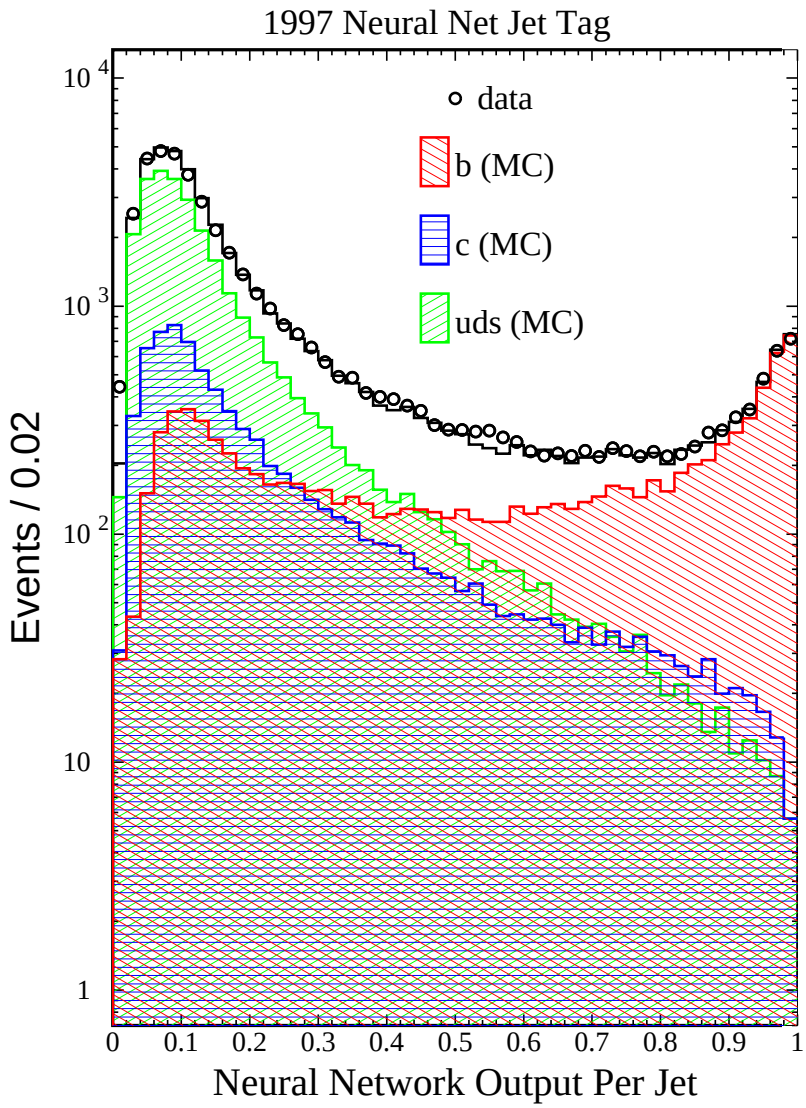

Figure 5.3: *The output of the neural network jet tag in 1997 Z peak data and Monte Carlo [80].*

the tracks measured in the TEC and SMD, to the clusters of calorimetric energy and to the muon momenta measured in the muon chambers. Individual particles are combined into pseudo-particles by using the DURHAM algorithm [84]. Two particles, i and j, are combined into a pseudo-particle if the parameter

$$y_{ij} = 2\frac{\min(E_i^2, E_j^2)}{E_{vis}^2}(1 - \cos\theta_{ij}) < y_{cut} \tag{5.4}$$

is below some predefined cutoff value y_{cut}, where E_i and E_j are the energies of the particles, θ_{ij} is the opening angle between them and E_{vis} is the total visible energy in the event. The algorithm loops over all possible combinations and combines the particles

with the smallest y_{ij} first. After having combined all particles, we have a new pseudo-particle list which is then again subject to Equation 5.4.
Proceeding in this way one can cluster the event into a certain number of pseudo-particles (jets) by adjusting the cutoff parameter y_{cut}. The y_{cut} parameter where the event changes from the four-jet to the three-jet topology is called Y_{34}. It evaluates the four-jet-likeness of an event.

5.1.4 Kinematic Fits

Kinematic fits are applied to improve the mass resolution of the reconstructed particles. This is achieved by varying the four momenta of the reconstructed objects within their resolution under constraints. These constraints are energy and momentum conservation and requirements on the di-jet and/or di-lepton masses.
In the analyses considered, we have three measured parameters for electrons and muons, namely the energy (momentum in the case of the muons) and the two angles ϕ and θ which determine their flight direction[3]. For the hadronic jets, the energy, the jet mass and the angles are available. The number of free parameters for the jets is also restricted to three, since it is expected that the jet mass will scale approximately as the size of the jet energy. The parameters are chosen to be the energy and the angles ϕ and θ. In total, we have therefore twelve measured parameters. They are not independent, but must obey at least energy and momentum conservation: ($\sum_{i=1}^{4} E_i = \sqrt{s}$, $\sum_{i=1}^{4} \vec{p}_i = \vec{0}$), where E_i is the energy of the jets (leptons) and $\vec{p}_i$ is their momentum. Further constraints can be introduced depending on the expected event topology. In the SM Higgs search, this is the Z mass constraint, where the invariant mass of the lepton pair (jet pair in the case of the $hZ \to \tau^+\tau^- q\bar{q}$ channel) is constrained to be equal to m_Z. For the charged Higgs search and the measurement of ZZ production, an equal mass constraint for the mother particles is used. The procedure is described in Reference [85]. The fit minimises a χ^2 function, which depends on the measured quantities and their errors and takes the constraints into account using the method of Lagrange multipliers.

5.1.5 The Discriminant Variable

After the selection, the most important variables are combined into one final discriminant, which is then used to evaluate the existence of a signal. This variable is constructed using a binned likelihood technique [86].
For each event class $j = (WW, qq, ZZ, Zee, hZ)$, probability density functions f_j^i are derived from Monte Carlo, where i denotes certain variables, which have discriminating power between the signal class and the background classes. In the case of the SM analyses, these are the neural network output variables for the b-tag of the two hadronic jets and the reconstructed mass.
The probability of an event to belong to the event class j, based solely on the value of

[3]For tau leptons the same fit routine is used with the approximation that the flight direction of the taus coincides with the direction of the visible decay products. As the tau energy is not known, infinite resolution is assumed.

the variable i, is then defined as

$$p_j^i = \frac{f_j^i}{\sum_k f_k^i}. \tag{5.5}$$

Finally, the individual probabilities are combined into a likelihood. The likelihood that an event belongs to the signal class F_{hZ} is given by the following equation:

$$F_{hZ} = \frac{\Pi_i p_{hZ}^i}{\sum_k \Pi_i p_k^i}, \tag{5.6}$$

where k runs over all event classes and i over all variables considered. The denominator in Equation 5.6 ensures that the value of F_{hZ} lies between zero and one. By including the mass information, this final discriminant becomes mass dependent and needs to be recalculated for every Higgs mass hypothesis that is made.

5.2 The $\mathbf{hZ \to b\bar{b}e^+e^-}$ Channel

The $hZ \to b\bar{b}e^+e^-$ channel is characterised by two high energetic electrons originating from a Z decay accompanied by two hadronic jets. Since the electrons result from the decay of a Z boson, their invariant mass is expected to be close to m_Z. The jets originate from the decay of the Higgs boson and usually contain b-quarks.
The main background source is $ZZ \to q\bar{q}e^+e^-$, which is kinematically very similar. This background becomes especially severe for Higgs mass hypotheses near the mass of the Z boson. The decay mode $ZZ \to b\bar{b}e^+e^-$ is irreducible. Other background sources are Zee, $q\bar{q}(\gamma)$ and WW production. The latter two have a different signature from the signal, but can contribute a sizable fraction to the background in the case of misidentified electrons.

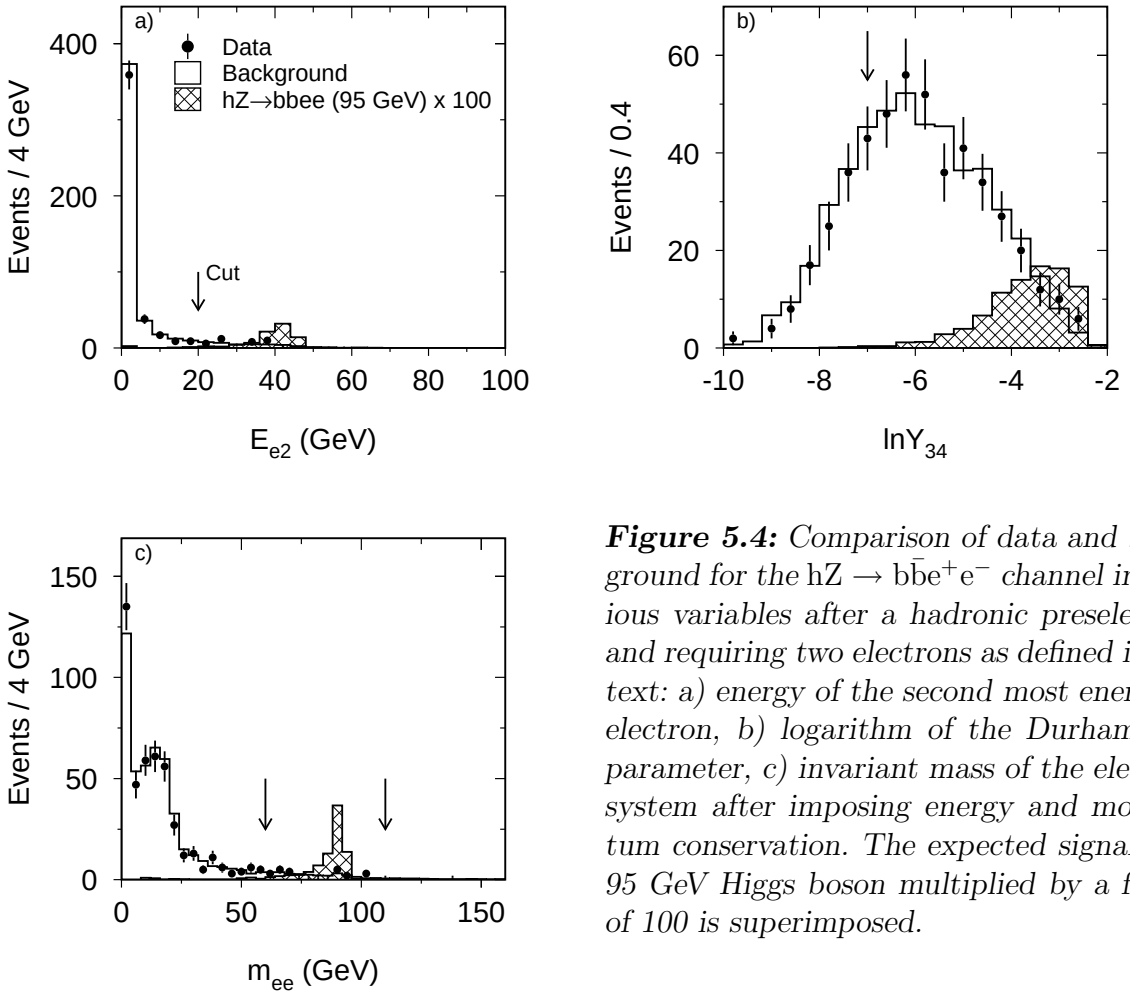

Figure 5.4: *Comparison of data and background for the* $hZ \to b\bar{b}e^+e^-$ *channel in various variables after a hadronic preselection and requiring two electrons as defined in the text: a) energy of the second most energetic electron, b) logarithm of the Durham* Y_{34} *parameter, c) invariant mass of the electron system after imposing energy and momentum conservation. The expected signal of a 95 GeV Higgs boson multiplied by a factor of 100 is superimposed.*

High multiplicity events are selected requiring at least 5 charged tracks and 15 calorimetric clusters. The visible energy must be larger than $0.4\sqrt{s}$. In the next step two electrons

are required. One of those has to pass the high quality criteria of category I. The second can be either category I or II. If there are more than two electron candidates in an event, the pair, where the invariant mass is closer to m_Z, is chosen. The two electrons are subtracted from the event, and the remaining objects are clustered into two jets using the Durham algorithm [84]. After this, 478 events remain in the data, where 490 events are expected from SM background processes. The signal efficiency for a 95 GeV Higgs boson is, at this point of the analysis, 84%. Figure 5.4 compares the observed data with the background expectation for the energy of the second most energetic electron, the logarithm of the Y_{34} Durham parameter and the invariant mass of the electron system after performing a kinematic fit which imposes energy and momentum conservation.
Soft cuts are placed to further reduce WW $\rightarrow$ qqeν and q$\bar{\text{q}}(\gamma)$ events while keeping the signal efficiency at a high level. Mass dependent cuts such as the opening angle of the electron pair (α_{ee}) and the opening angle of the jet pair (α_{qq}) are chosen in such a way that they allow a good sensitivity over a mass range from 50 to 100 GeV. As pointed out earlier, background events at low masses will not affect a high Higgs mass hypothesis because they are suppressed by the mass information which enters the final discriminant variable[4]. The full set of cuts and their effect on reducing the data sample can be found in Table 5.1. After the selection, 15 candidates are observed with a background expecta-

Selection step	Background	Data	Efficiency (%)
$N_{tracks} \geq 5, N_{Cluster} \geq 15,$			
$E_{vis}/\sqrt{s} \geq 0.4$, 2 electrons	489.7	478	84.0
$E_{e2} \geq 20$ GeV	40.3	46	79.2
$\ln Y_{34} \geq -7$	28.8	34	78.7
$\alpha_{ee} \geq 100°$, $\alpha_{qq} \geq 50°$	19.7	23	78.6
$E_{vis}/\sqrt{s} \geq 0.7$	18.0	19	78.0
$p_T^{miss}/E_{vis} \leq 0.2$	15.4	17	77.5
$60 \leq m_{ee}/$ GeV ≤ 110	13.2	15	77.0

Table 5.1: *Selection steps of the* $hZ \rightarrow b\bar{b}e^+e^-$ *channel for which data and expectations from SM background processes are compared. The signal efficiency is given for a 95 GeV Higgs boson. The abbreviations have the following meaning:* N_{tracks} *is the number of tracks,* $N_{Cluster}$ *the number of calorimetric clusters,* E_{vis} *the visible energy and* p_T^{miss} *the missing transverse momentum. The other abbreviations are explained in the text.*

tion of 13.2 events. The background is dominated by ZZ (40%) and Zee (27%). Smaller contributions come from q$\bar{\text{q}}(\gamma)$ (17%) and WW (16%). A typical candidate is shown in Figure 5.7. The signal efficiencies for various Higgs masses are shown in Table 5.4.
The background expectation is still large, but the most important variables, namely the b-tags of the hadronic jets and the Higgs mass information have not yet been exploited. Figure 5.5 shows the b-tag distributions and the reconstructed Higgs mass distributions

[4]Performance at very low Higgs masses is not a major issue for the interpretation of the results which will be done in this thesis. However, for future interpretations in more general Higgs models with lower expected signal cross sections the analysis presented here, can be reused.

after constraining the electron pair to m_Z.

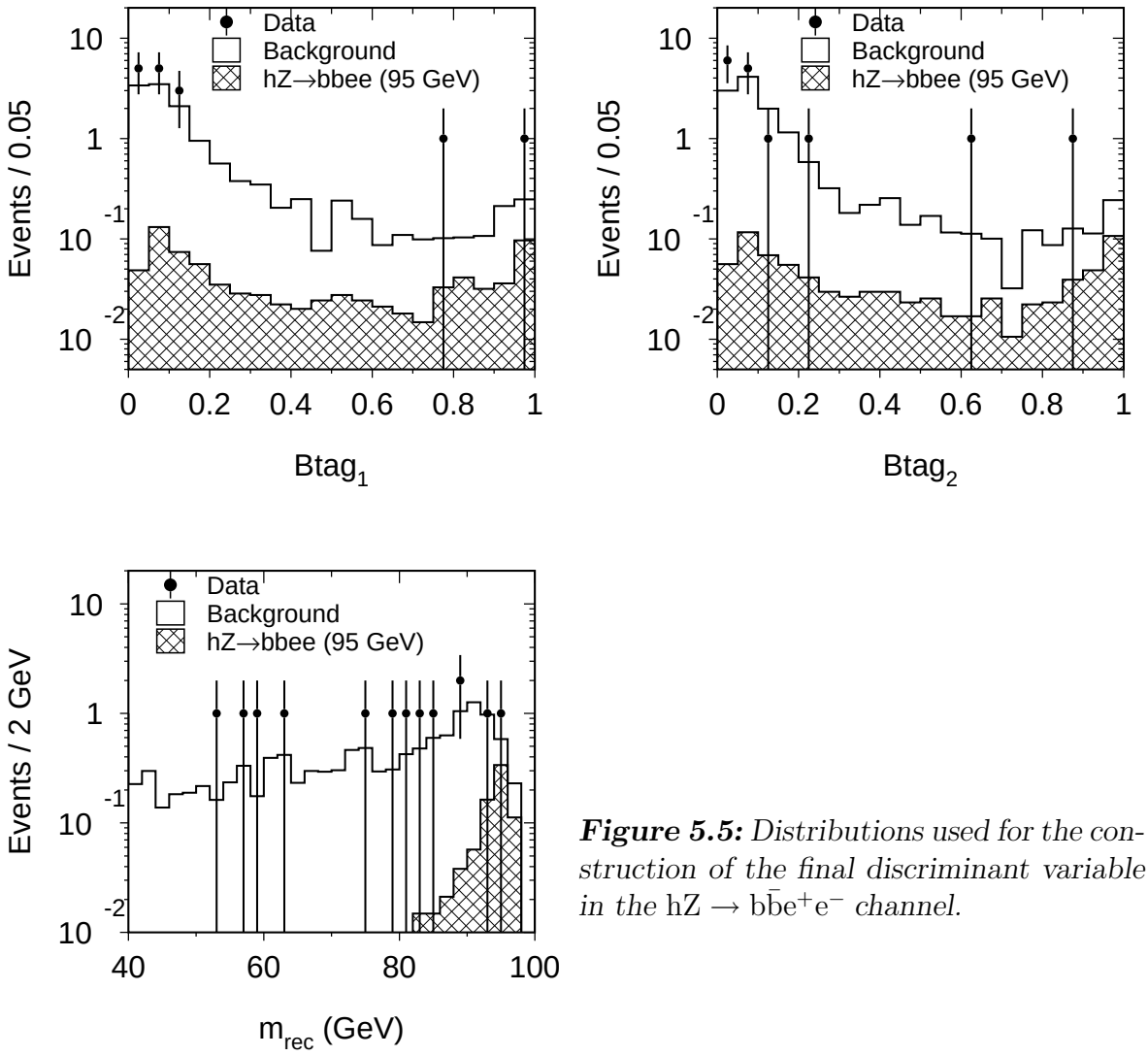

Figure 5.5: *Distributions used for the construction of the final discriminant variable in the* $\mathrm{hZ \to b\bar{b}e^+e^-}$ *channel.*

These variables are combined into one discriminating variable using the technique described in section 5.1.5. The result of this combination is shown in Figure 5.6 for a 95 GeV Higgs mass hypothesis. If one integrates the discriminant from right to left, one gets an impression of the analysis performance as can be seen on the right-hand side of Figure 5.6. The discriminant variable is recalculated for every Higgs mass hypothesis in steps of 100 MeV for Higgs masses between 70 and 100 GeV and in steps of 1 GeV for Higgs masses between 50 and 70 GeV. No deviation from the background expectation is observed. The discriminants are used in the limit calculation in combination with the other channels to be described in chapter 8.

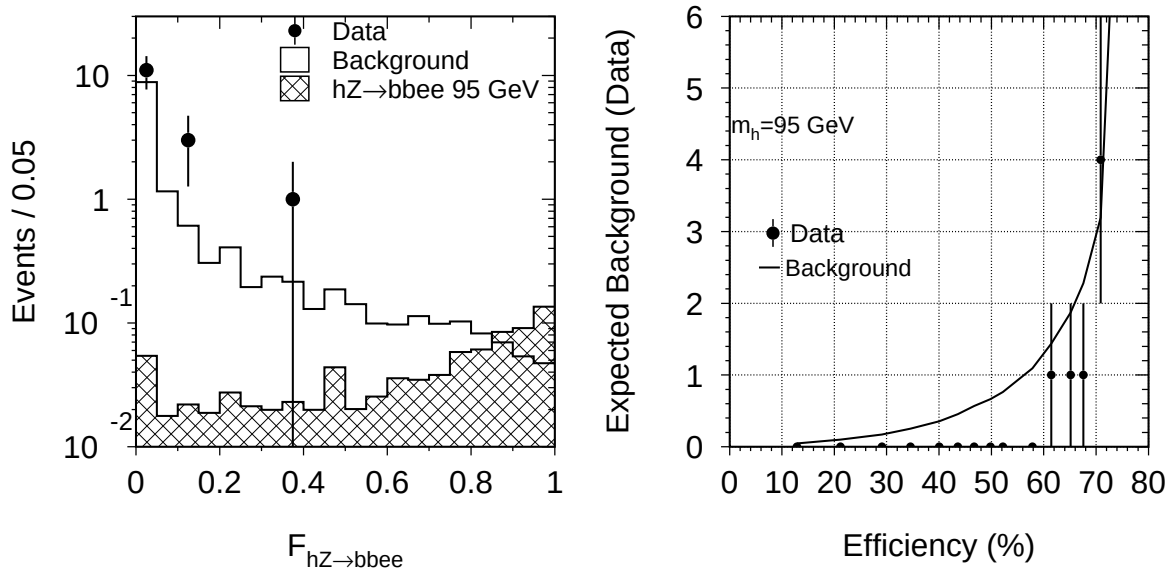

Figure 5.6: *Left: Comparison of data, background and signal for the* $\mathrm{hZ} \rightarrow \mathrm{b\bar{b}e^+e^-}$ *channel in the final discriminant variable at* $\mathrm{m_h} = 95$ *GeV. Right: Expected background versus signal efficiency obtained by integrating the discriminant variable from right to left.*

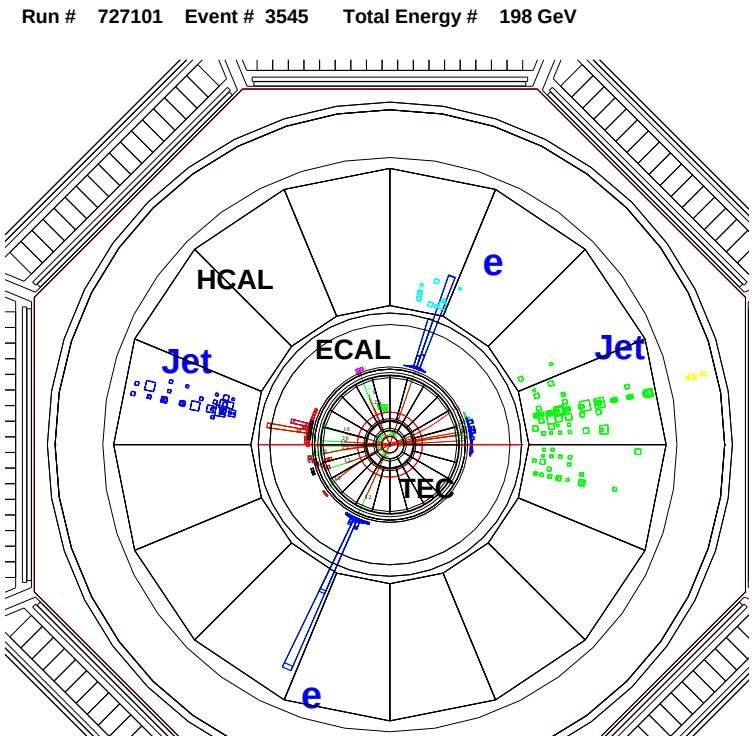

Figure 5.7: *Kinematically accepted candidate for the* $\mathrm{hZ} \rightarrow \mathrm{b\bar{b}e^+e^-}$ *channel. The invariant mass of the electron system is 91.2 GeV and for the jet system 85.3 GeV. The neural net b-tag for the most energetic jet is 0.01 and for the second most energetic jet 0.03. The candidate is consistent with the expectation from* $\mathrm{ZZ} \rightarrow \mathrm{q\bar{q}e^+e^-}$.

5.3 The $\mathbf{hZ \to b\bar{b}\mu^+\mu^-}$ Channel

The $hZ \to b\bar{b}\mu^+\mu^-$ channel is very similar to the $hZ \to b\bar{b}e^+e^-$ channel. The Z boson decays into a pair of muons whereas the Higgs should be observed by two hadronic jets with lifetime information.
As in the electron analysis high multiplicity events are selected with at least 5 tracks, 15 calorimetric clusters and a visible energy of at least $0.4\sqrt{s}$. Then, two muons are required: one of which should be identified in the muon chambers (category I) and the other can be a MIP (category II). After these requirements, 46 events remain in the data whereas 43.7 are expected from SM background processes. The signal efficiency for a 95 GeV Higgs boson is 64.4%. At this stage, there is still a large contribution from $q\bar{q}$ events, where leakage from high energetic jets fake a muon signal in the muon chamber (punchthroughs). This background is reduced by requiring a minimal energy on the muons of category I and taking advantage of the "four-jet likeness" of the expected signal by putting a soft cut on $\ln Y_{34}$. Background from $WW \to qq\mu\nu$ is characterised by a transverse imbalance due to the neutrino. The signal, however, is balanced in momentum (see Figure 5.8). An upper cut on the transverse imbalance is therefore placed. The full

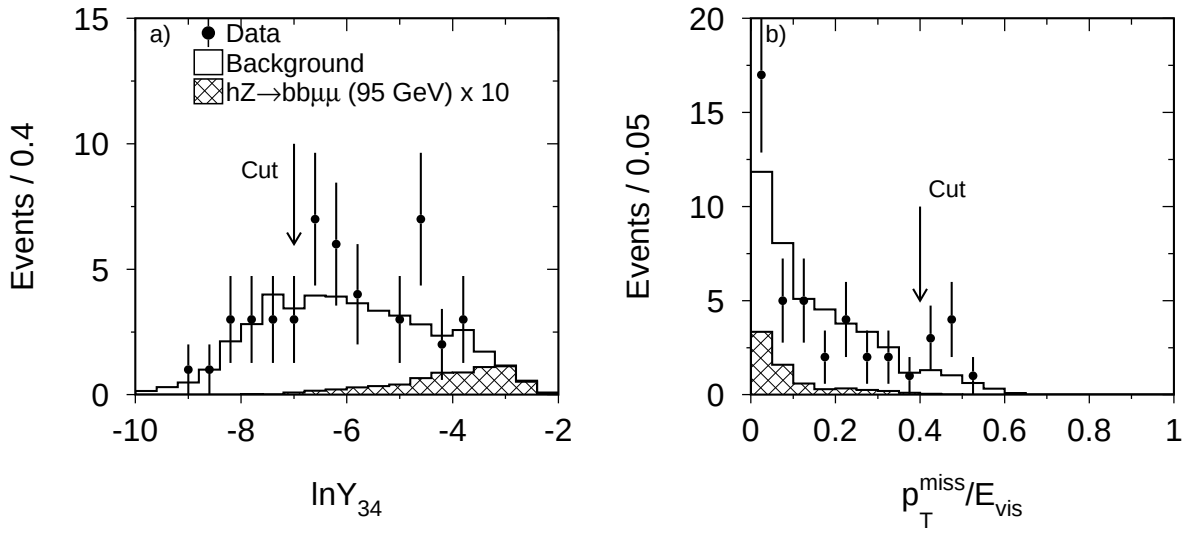

Figure 5.8: *Comparison of data, background and signal for the* $hZ \to b\bar{b}\mu^+\mu^-$ *channel after a hadronic preselection and requiring two muons as described in the text. The distributions shown are a) the logarithm of the* Y_{34} *Durham parameter and b) the transverse imbalance* (p_T^{miss}/E_{vis})*. The signal expectation is multiplied by a factor of 10.*

set of cuts can be found in Table 5.2. After the selection there are 5 events in the data with a background expectation of 5.5 events and a signal efficiency of 57% at 95 GeV. The background is dominated by ZZ production (82%). Smaller contributions come from WW (13%) and $q\bar{q}$(5%). The efficiencies for other Higgs mass hypotheses are shown in Table 5.4.

Selection step	Background	Data	Efficiency (%)
$N_{tracks} \geq 5, N_{Cluster} \geq 15,$			
$E_{vis}/\sqrt{s} \geq 0.4$, 2 muons	43.7	46	64.4
$E_{\mu} \geq 15$ GeV	15.5	13	62.0
$\ln Y_{34} \geq -7$	11.6	9	61.6
$\alpha_{\mu\mu} \geq 90°$	7.5	6	61.1
$p_T^{miss}/E_{vis} \leq 0.4$	7.1	5	60.4
$50 \leq m_{\mu\mu}/$ GeV ≤ 125	5.5	5	57.0

Table 5.2: *Selection steps of the* $hZ \to b\bar{b}\mu^+\mu^-$ *channel for which data and expectations from SM background processes are compared. The signal efficiency is given for a 95 GeV Higgs boson.*

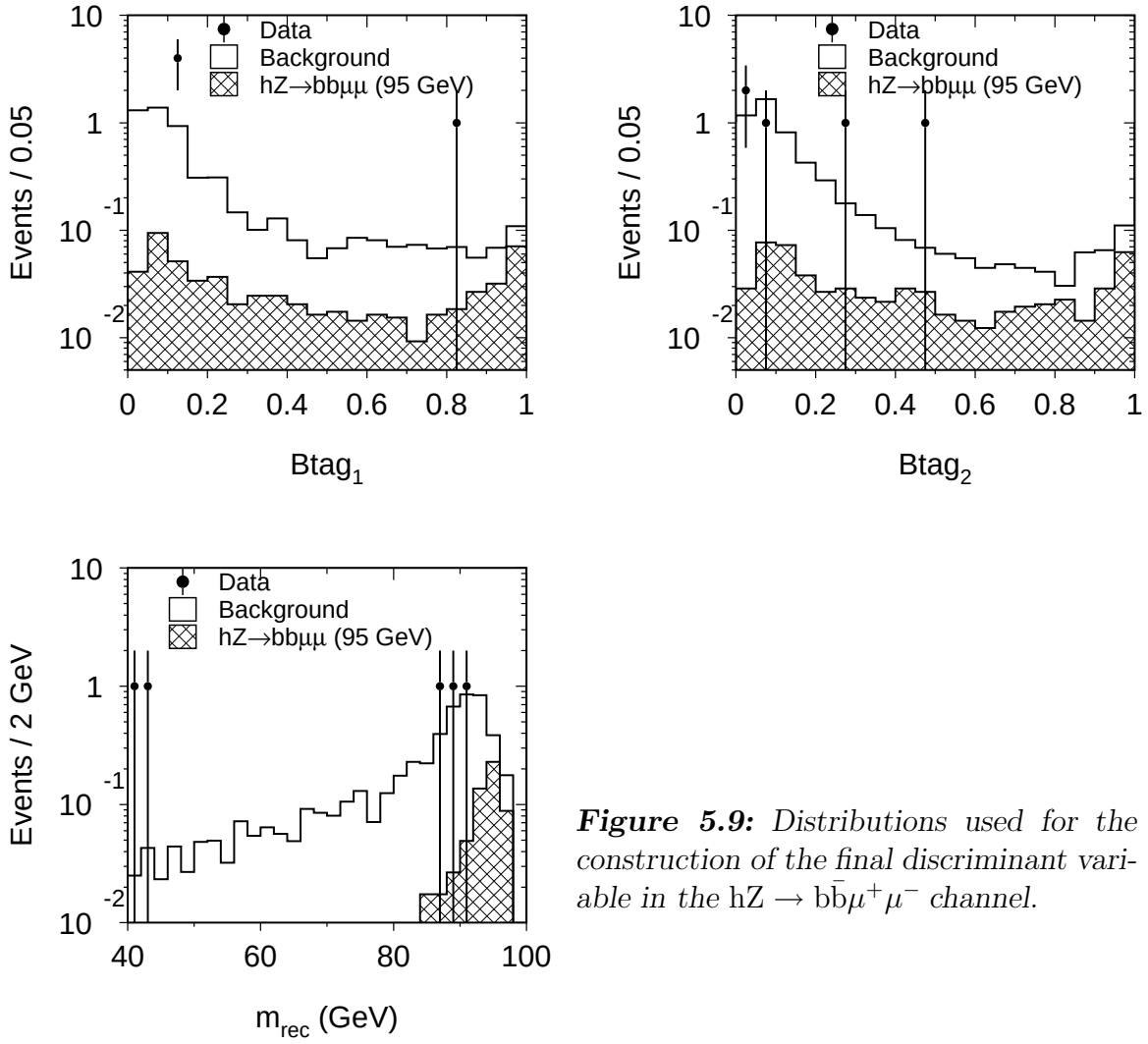

Figure 5.9: *Distributions used for the construction of the final discriminant variable in the* $hZ \to b\bar{b}\mu^+\mu^-$ *channel.*

As in the case of the $hZ \to b\bar{b}e^+e^-$ channel, the most discriminating variables (Figure 5.9) are combined into the final variable which is shown for a 95 GeV Higgs mass hypothesis in Figure 5.10. No indication for a signal is found in this channel.

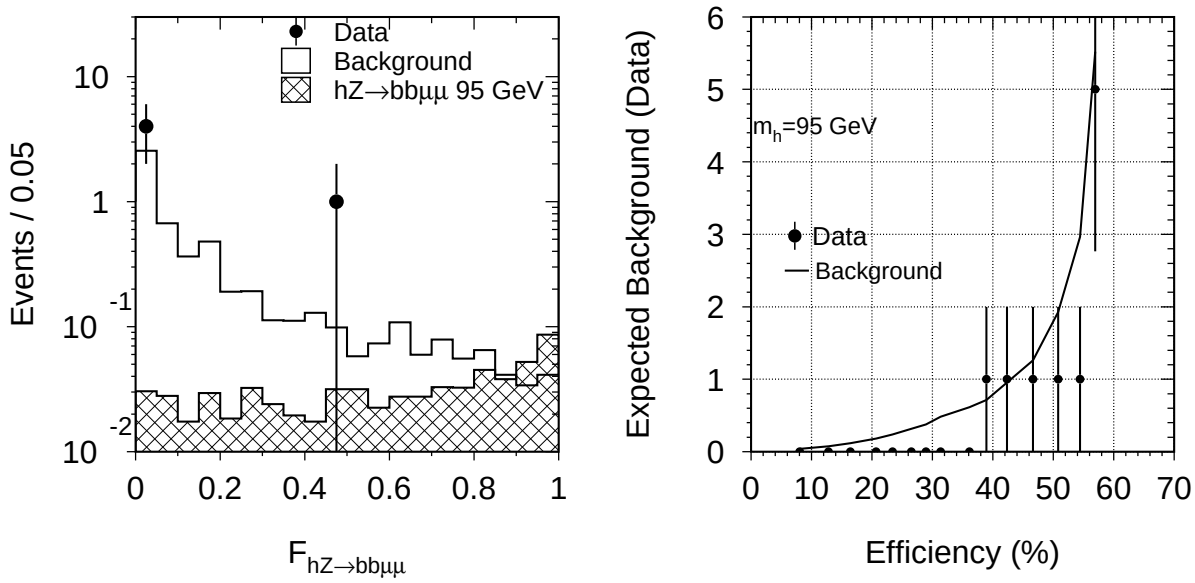

Figure 5.10: *Left: Comparison of data, background and signal for the* $hZ \to b\bar{b}\mu^+\mu^-$ *channel in the final discriminant variable at* $m_h = 95$ *GeV. Right: Expected background versus signal efficiency obtained by integrating the discriminant variable from right to left.*

5.4 The hZ → $b\bar{b}\tau^+\tau^-$ and the hZ → $\tau^+\tau^-q\bar{q}$ Channels

The hZ → $b\bar{b}\tau^+\tau^-$ and hZ → $\tau^+\tau^-q\bar{q}$ final states are very similar and can be distinguished only with mass and b-tag information. The semileptonic W- and Z-pair decays are the most significant background sources.
A selection based on a strict τ identification leads to a clean sample, however, with a rather low signal efficiency. Taking into account that one can still exploit the reconstructed Higgs mass after the selection (and in the case of the hZ → $b\bar{b}\tau^+\tau^-$ channel also the b-tag information) allows one to perform a less stringent selection. This will lead to an overall increase in background, which is expected to spread evenly over the entire mass spectrum. The increase in the signal efficiency is, however, localised around the particular Higgs mass hypothesis, if the event was correctly reconstructed.
Two inclusive selections are performed, one based on a tau identification (particle-based selection) and one relying more on the event kinematics (jet-based selection). Events are accepted if they pass either of the two selections. First, a common preselection is applied, requiring more than 4 charged tracks, more than 14 clusters and a visible energy of more than $0.4\sqrt{s}$. The events are subject to the DURHAM algorithm, keeping only those with $\ln Y_{34}$ larger than -6. Background from $q\bar{q}(\gamma)$ is reduced by rejecting events containing photons with energies greater than 40 GeV. The contribution of WW → $qq\ell\nu$ ($\ell = e, \mu$) is reduced by requiring the energy of electrons and muons to be smaller than 40 GeV.
In the particle-based selection, tau leptons are identified via their decay into electrons or muons, or as an isolated low-multiplicity jet with 1 or 3 tracks and unit charge as described in section 5.1.1. In the jet-based selection, the event is forced into four jets using the DURHAM algorithm. Two of the jets must each have less than 4 tracks. These jets are considered as tau candidates, but at least one of them must coincide with a tau candidate defined in the particle-based selection within a 3° cone. The taus must be separated from the hadronic jets by at least 25°. In both selections background contamination from fully hadronic WW decays is reduced by rejecting events where both taus decay into 3 charged particles. The visible energy must be smaller than $0.95\sqrt{s}$ for the particle-based and smaller than $0.9\sqrt{s}$ for the jet-based selection. Moreover, in the jet-based selection, the polar angle of the missing momentum vector, θ_{miss}, must satisfy $|\cos\theta_{\mathrm{miss}}| \leq 0.95$ in order to reduce $q\bar{q}(\gamma)$ contamination. The invariant masses of the tau-tau and the jet-jet systems are obtained from a kinematic fit which imposes 4-momentum conservation[5]. An event qualifies for the hZ → $b\bar{b}\tau^+\tau^-$ channel if the invariant mass of the tau-tau system is consistent with the mass of the Z boson by lying between 70 GeV and 125 GeV. Similarly, an event qualifies for the hZ → $\tau^+\tau^-q\bar{q}$ channel if the jet-jet mass fulfils this same requirement. Furthermore, the opening angle of the particles or jets assigned to the Higgs boson must be larger than 70° and those assigned to the Z must be at least 100° apart. The complete analysis flow is shown in Figure 5.11.
Table 5.3 compares the number of background events with the observed candidates

[5] As the energy of τs is unknown, the direction of the τs is fixed to the direction of the decay particles, and infinite resolution is assumed for the τ energy in the fit.

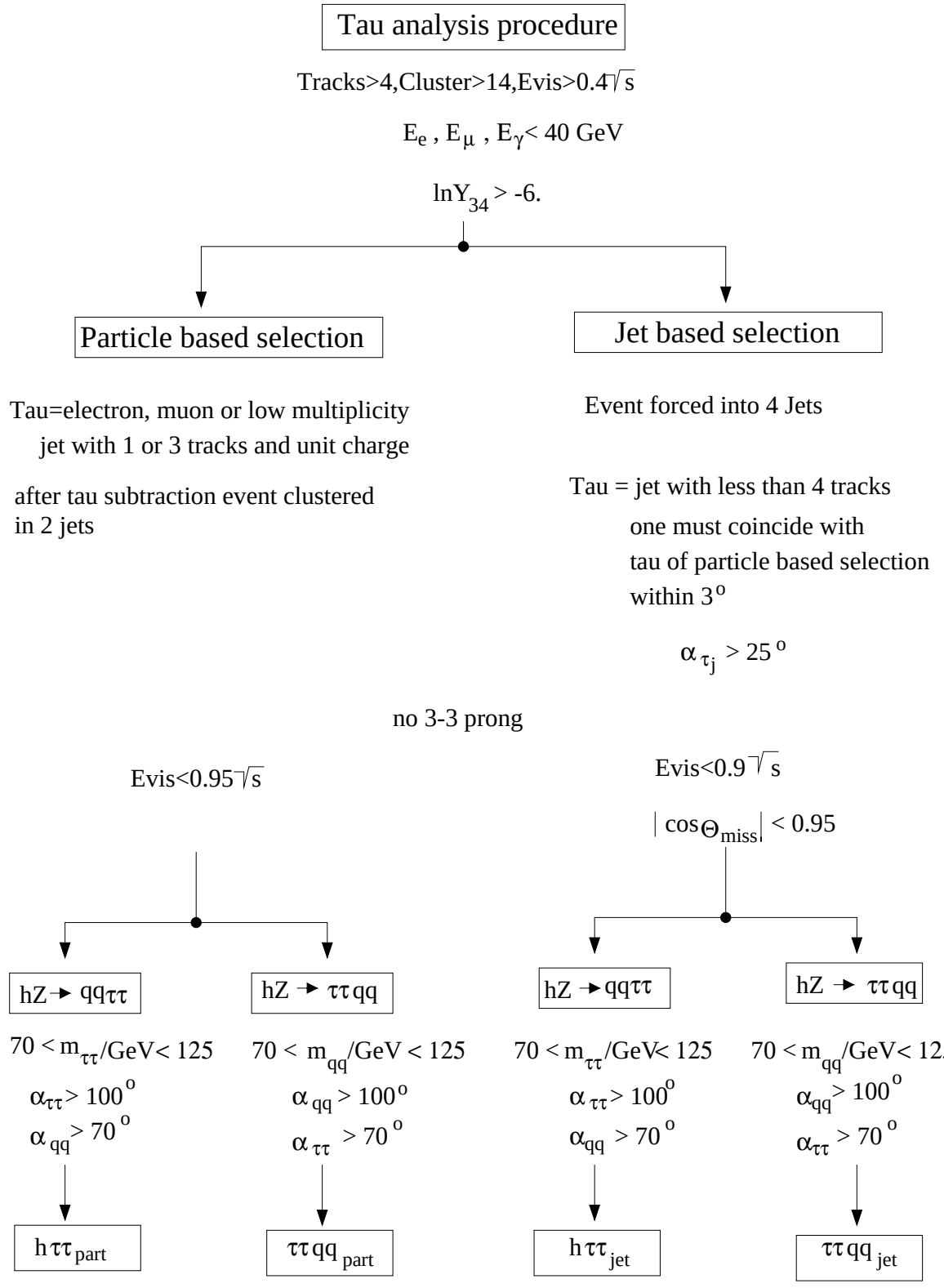

Figure 5.11: *Tau analysis flow in the SM Higgs search.*

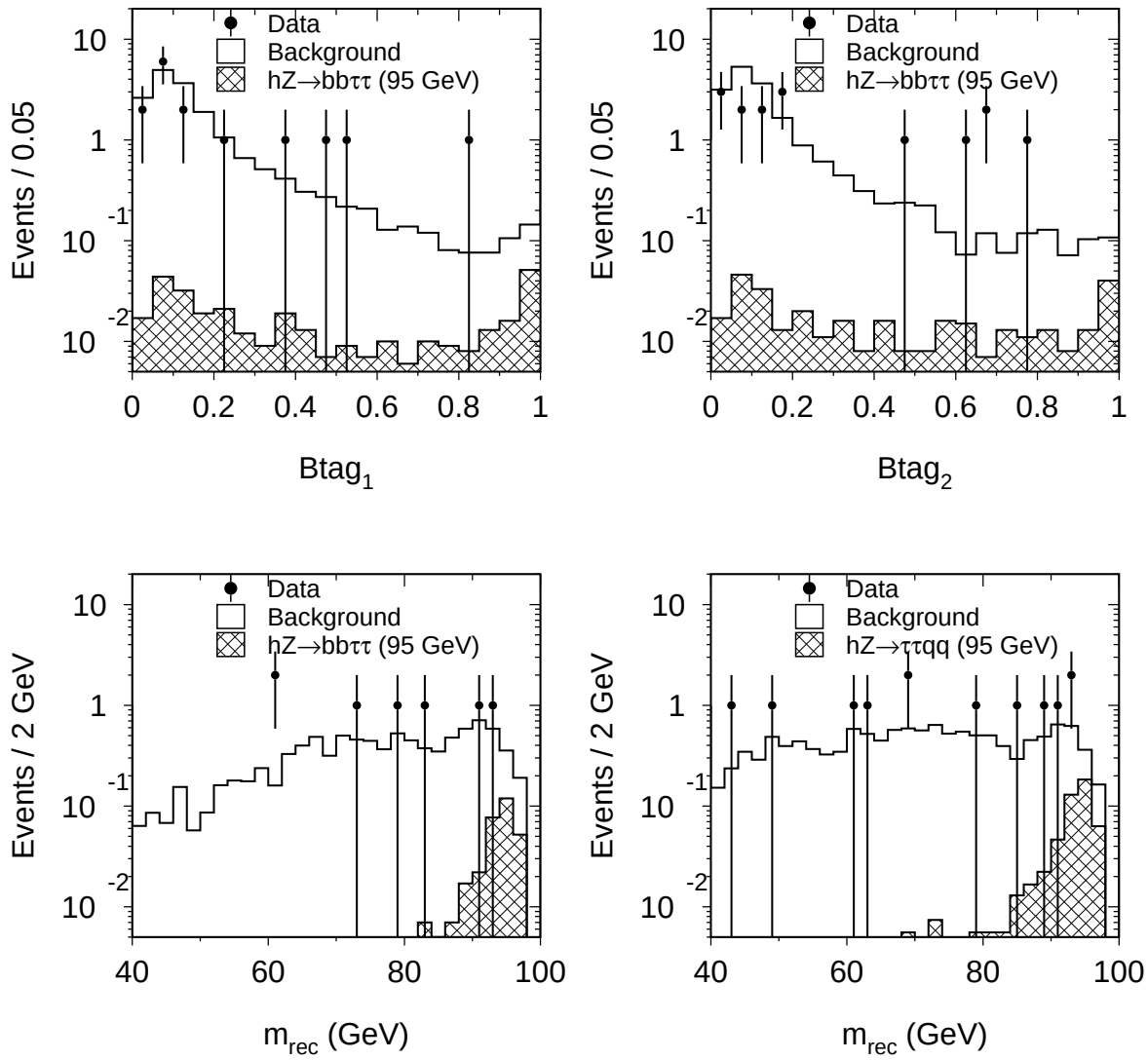

Figure 5.12: *Top: b-tag variables for the two hadronic jets. The events have passed the particle-based or the jet-based selection. The* $\mathrm{hZ} \to \mathrm{b\bar{b}}\tau^+\tau^-$ *signal is superimposed. Bottom: reconstructed Higgs mass after imposing energy and momentum conservation and constraining the invariant mass of the tau pair (left) or the jet pair (right) to* $\mathrm{m_Z}$*. The events have passed the particle- or the jet-based selection for the* $\mathrm{hZ} \to \mathrm{b\bar{b}}\tau^+\tau^-$ *channel (left) and the* $\mathrm{hZ} \to \tau^+\tau^-\mathrm{q\bar{q}}$ *channel (right).*

and the obtained signal efficiencies of a 95 GeV Higgs boson for the various selections and their combinations. The background composition is also shown. Figure 5.12 shows the b-tag distributions, where the events have passed any of the tau selections and the reconstructed Higgs masses after having constrained the invariant mass of the taus ($\mathrm{hZ} \to \mathrm{b\bar{b}}\tau^+\tau^-$ selection) and the invariant mass of the jets ($\mathrm{hZ} \to \tau^+\tau^-\mathrm{q\bar{q}}$ selection) to $\mathrm{m_Z}$. A selected candidate, where the tau leptons are identified by their decay in an

Selection	$\epsilon^{95}_{H\tau\tau}$ (%)	$\epsilon^{95}_{\tau\tau qq}$ (%)	WW	qq	ZZ	Zee	Total	Data
I) $H\tau\tau_{part}$	15.6	17.5	1.5	0.2	1.3	0.2	3.2	4
II) $H\tau\tau_{jet}$	23.4	21.1	4.2	1.0	1.8	0.2	7.2	4
III) I or II	29.9	30.0	5.6	1.2	2.4	0.3	9.5	7
IV) $\tau\tau qq_{part}$	16.5	18.8	2.6	0.5	1.8	0.4	5.3	5
V) $\tau\tau qq_{jet}$	23.6	19.7	6.2	1.1	2.1	0.3	9.7	8
VI) IV or V	30.3	30.2	8.6	1.6	3.0	0.6	13.8	12
VII) III or VI	31.5	32.2	11.3	2.3	3.3	0.7	17.6	15

Table 5.3: *Background expectations and observed candidates for the τ selections. The signal efficiencies are for a Higgs mass of 95 GeV.*

isolated electron and muon respectively, is shown in Figure 5.13.

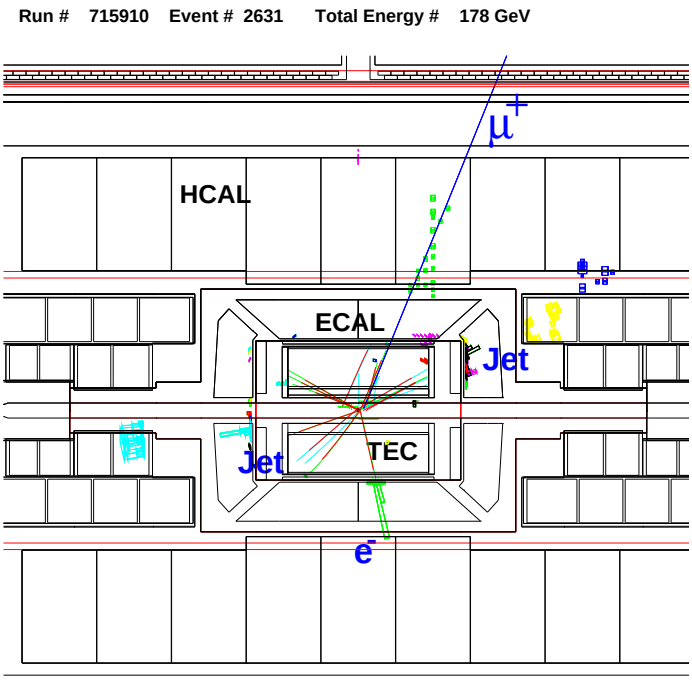

Figure 5.13: *Kinematically accepted candidate for the* $hZ \rightarrow b\bar{b}\tau^+\tau^-$ *and the* $hZ \rightarrow \tau^+\tau^-q\bar{q}$ *channel. The τ leptons are identified by their decay into an electron and a muon. The invariant mass of the tau system after imposing energy and momentum conservation is 84.4 GeV and for the jet system 95.1 GeV. The neural net b-tag for the most energetic jet is 0.02 and for the second most energetic jet 0.11. The candidate is consistent with the expectation from* $ZZ \rightarrow q\bar{q}\tau^+\tau^-$.

5.5 Analysis Performance and Cross Efficiencies

The selection efficiencies for the various Higgs masses in the different channels are summarised in Table 5.4. Good sensitivity is obtained over the entire mass range under consideration. The next question, that needs to be addressed, is the event overlap between the selections. Significant overlaps are expected between the $hZ \rightarrow b\bar{b}\tau^+\tau^-$ and $hZ \rightarrow \tau^+\tau^-q\bar{q}$ channel, but also between the tau selections and the $hZ \rightarrow b\bar{b}e^+e^-$ and the $hZ \rightarrow b\bar{b}\mu^+\mu^-$ selections. Table 5.5 shows the cross efficiencies between the different

Selection of process	Efficiency (%) on m_h = (GeV)							
	50	60	70	80	85	90	95	100
$hZ \to b\bar{b}e^+e^-$	73.9	78.2	77.2	76.4	77.8	75.7	77.0	66.7
$hZ \to b\bar{b}\mu^+\mu^-$	52.4	53.6	54.7	57.4	59.5	58.2	56.9	54.7
$hZ \to b\bar{b}\tau^+\tau^-$	27.8	30.8	28.5	31.3	29.8	31.8	29.9	24.2
$hZ \to \tau^+\tau^-q\bar{q}$	27.5	30.5	30.2	34.1	36.0	32.6	30.2	26.0

Table 5.4: *Selection efficiencies for various Higgs masses in the Standard Model at* $\sqrt{s} = 189$ *GeV.*

Selection of Process $hZ \to$	Efficiency (%) on $hZ \to$			
	$b\bar{b}e^+e^-$	$b\bar{b}\mu^+\mu^-$	$b\bar{b}\tau^+\tau^-$	$\tau^+\tau^-q\bar{q}$
$b\bar{b}e^+e^-$	77.0	0.0	0.9	1.7
$b\bar{b}\mu^+\mu^-$	0.0	56.9	1.0	1.8
$b\bar{b}\tau^+\tau^-$	1.4	2.4	29.9	30.0
$\tau^+\tau^-q\bar{q}$	1.8	2.6	30.3	30.2

Table 5.5: *Cross efficiency table for the lepton channels. The efficiencies are given for* $m_h = 95$ *GeV.*

selections for a 95 GeV Higgs boson. These cross efficiencies are treated in the following way. Events, which were already selected in the $hZ \to b\bar{b}e^+e^-$ and the $hZ \to b\bar{b}\mu^+\mu^-$ channel , are rejected in the τ channel selections. After this requirement 12 events remain for the tau channels with a background expectation of 17.1 events. Finally, the events, which pass the $hZ \to b\bar{b}\tau^+\tau^-$ and the $hZ \to \tau^+\tau^-q\bar{q}$ selections, are placed in either of the two, depending on the value of $F_{hZ\to b\bar{b}\tau^+\tau^-}$ and $F_{hZ\to\tau^+\tau^-q\bar{q}}$. As these two likelihood values depend on the Higgs mass hypothesis, the relative ratio of the collected background (and candidates) changes by changing the Higgs mass hypothesis. The distributions used for the combination with the other channels are shown in Figure 5.14 for a 95 GeV Higgs mass hypothesis. In chapter 8 a quantitative analysis on the overall agreement between the observed candidates and the MC expectation will be presented, when all search channels are combined. A qualitative look can already be made at this point. For this, the final discriminants from 50 to 95 GeV are considered in steps of 5 GeV. A cut of $F_{hZ} > 0.5$ is placed on the distributions for $hZ \to b\bar{b}\ell^+\ell^-$ ($\ell = e, \mu, \tau$). For the $hZ \to \tau^+\tau^-q\bar{q}$ channel, the bin closest to the Higgs mass hypothesis is considered. The candidates of the channels passing these requirements are summed up and compared to the background and signal expectation. This is shown in Figure 5.15. The observed candidates are consistent with the expected background.

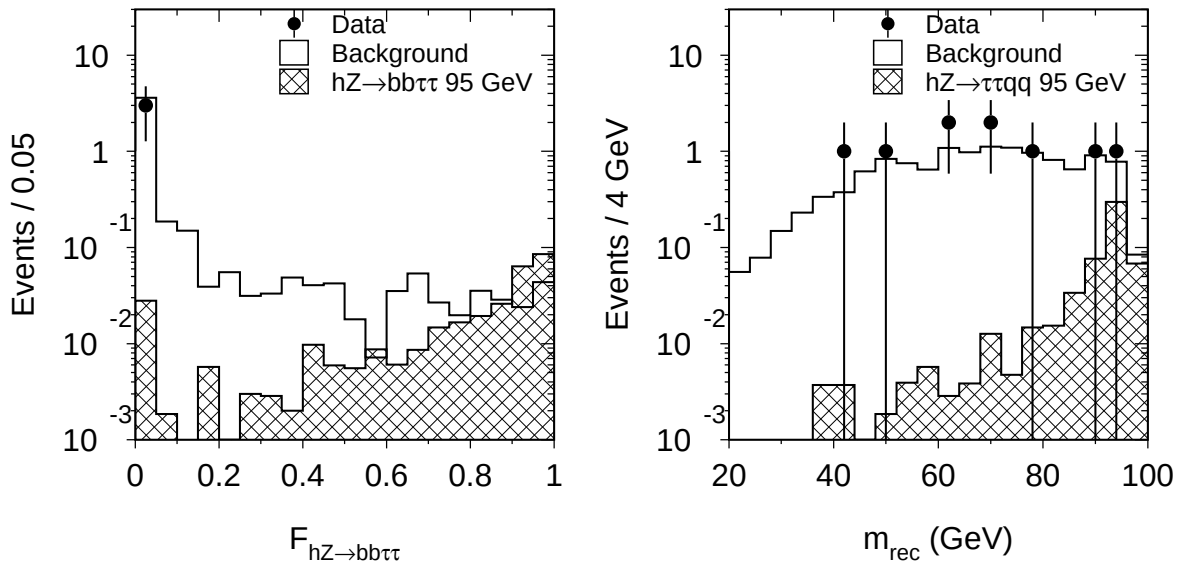

Figure 5.14: *Final discriminant,* $\mathrm{F_{hZ\to b\bar{b}\tau^+\tau^-}}$*, for the* $\mathrm{hZ \to b\bar{b}\tau^+\tau^-}$ *and the reconstructed mass,* $\mathrm{m_{rec}}$*, for the* $\mathrm{hZ \to \tau^+\tau^- q\bar{q}}$ *channel at* $\mathrm{m_h} = 95$ *GeV.*

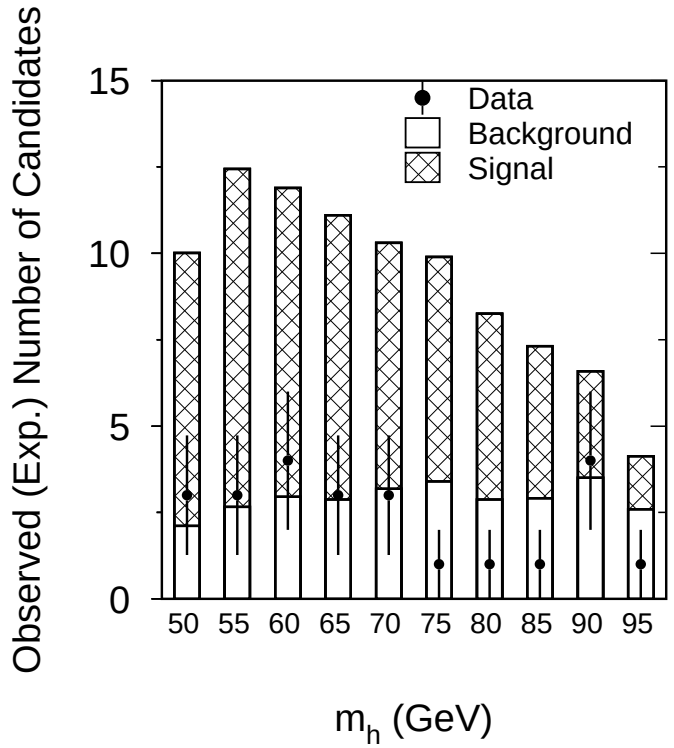

Figure 5.15: *Combined number of candidates for the* $\mathrm{hZ \to b\bar{b}\ell^+\ell^-}$ *and* $\mathrm{hZ \to \tau^+\tau^- q\bar{q}}$ *channels at various Higgs mass hypotheses for* $\sqrt{s} = 183$ *to* 189 GeV*. For the* $\mathrm{hZ \to b\bar{b}\ell^+\ell^-}$ *channels a cut of* $\mathrm{F_{hZ}} \geq 0.5$ *was placed. For the* $\mathrm{hZ \to \tau^+\tau^- q\bar{q}}$ *channel the bin closest to the Higgs mass hypothesis is considered. For* $\mathrm{m_h} = 50$ GeV *and 95 GeV the 183 GeV data are not included. This plot is purely illustrative. For the derivation of the mass limit to be discussed in chapter 8 the entire discriminant spectrum is used.*

5.6 Systematic Errors

Systematic uncertainties may arise if the Monte Carlo modelling can not adequately describe the data. This can be caused by an inadequate theoretical description plugged

into the Monte Carlo or by detector effects, which are not fully understood and not included in the realistic Monte Carlo simulation. This section describes the determination of systematic uncertainties.

Lepton Identification:
The selected Higgs sample considered here is too small to evaluate systematic errors because any deviation can be of purely statistical origin. Therefore, high statistic reference samples have been studied. These were $e^+e^- \to e^+e^-$, $e^+e^- \to \mu^+\mu^-$ and $e^+e^- \to \tau^+\tau^-$ obtained from $\approx 3\ pb^{-1}$ Z peak calibration data as well as from the high energy data at $\sqrt{s} = 189$ GeV taken in 1998. The reference samples are selected by making low multiplicity requirements and introducing veto cuts on possible background sources avoiding direct lepton identification criteria of the lepton flavour under consideration (for a description of the selection see appendix E). Examples of distributions are shown in Figure 5.16. There is good agreement found for electrons and taus within the statistical error of the reference sample. For muons the amount of well measured muons (triplets), relative to less well measured muons (doublets) and MIPs is overestimated in the Monte Carlo. This can be seen in Figures 5.16 c) and d). The effect of the lepton identification is studied for the barrel and the endcap region of the detector, separately. For this, the lepton identification criteria are applied to the sample, and the event acceptance is determined for both Monte Carlo and data. The statistical error of the reference sample is not negligible. The relative acceptance difference is summed in quadrature with the relative statistical error of the data reference sample and is considered as the systematic error in the lepton identification[6]. In order to evaluate the effect on the subsequent Higgs selections for both the Higgs signal and the background, the relative amount of events in the barrel and the endcap region is determined. The error assigned to the signal and the background is then the acceptance weighted average of the error on the lepton identification in the barrel and the endcap region. The assigned errors are shown in Table 5.6.

B-tagging:
B-tagging is not used in the selection but is included in the final discriminant. Therefore, a deviation between data and Monte Carlo will translate directly into the final discriminant, which is used in the limit calculation to be described in chapter 8. For the evaluation of b-tagging systematics a reference sample of radiative $q\bar{q}(\gamma)$ events was chosen. The event selection is described in appendix E. A sample of 6477 events is selected with a contribution of 97 % from $q\bar{q}(\gamma)$ events. The remaining background comes from WW, ZZ, Zee, two-photon interactions and single-W production. The efficiencies for the various Higgs channels in this sample are: 0.4% for $hZ \to b\bar{b}q\bar{q}$, 0.3% for $hZ \to b\bar{b}\nu\bar{\nu}$, 0.3% for $hZ \to b\bar{b}e^+e^-$, 0.6% for $hZ \to b\bar{b}\mu^+\mu^-$, less than 0.1% for $hZ \to b\bar{b}\tau^+\tau^-$ and 0.3% for $hZ \to \tau^+\tau^- q\bar{q}$ [7]. Even if the Higgs were present in the data, it would not influence the sample discussed here. The neural network b-tag distributions are shown in Figure 5.17. Very good agreement is found in the b-tag spectrum of the second most

[6] Alternatively one could use LEPI Z peak data to suppress the statistical error of the reference sample. However this can cause new uncertainties as the detector performance and the reconstruction code may be different for different data taking periods.

[7] The numbers are given for a 95 GeV Higgs.

energetic jet. In the spectrum of the first jet, the data are slightly shifted towards higher b-tag values. This gets emphasised if one integrates the spectrum from right to left (see Figure 5.17 e)). An enhancement of high b-tag events in the data with respect to the Monte Carlo can only deteriorate the mass limit. Hence, the observed limits to be derived in chapter 8 can be considered as conservative.

Energy Scale:
The systematic error arising from the energy scale has been evaluated by changing energy scale related quantities in the selection by ±2%, which corresponds to the maximal uncertainty in the calibration method. The errors assigned to the signal and the background are shown in Table 5.6.

Background Normalisation:
Following the suggestion of the LEP ZZ working group, the following uncertainties on the background cross section are assumed: 2% on WW and 5% on $q\bar{q}$, ZZ and Zee. The influence on the Higgs background expectation is shown in Table 5.6.

Theoretical Signal uncertainty:
Signal cross section errors arise from uncertainties in m_{top} and α_s ($\approx 0.1\%$) [87]. The Higgs decay branching ratio uncertainties amount to 1% [88].

Luminosity Error:
The relative uncertainty in the luminosity measurement is 0.3%.

Monte Carlo Statistics:
The statistical error on the predicted number of background and signal events from the finite number of generated Monte Carlo events is large, but is uncorrelated from bin to bin in the final discriminant distributions and has little effect on the result.

The systematic errors are taken into account as described in chapter 8.

5.7 The Other Channels

The selection and the results of the remaining two channels ($hZ \to b\bar{b}\nu\bar{\nu}$ and $hZ \to b\bar{b}q\bar{q}$) are explained in detail in References [89, 90]. The general search strategy is similar to the one described in the previous sections. Mass independent selections and kinematic fits are performed and finally a mass dependent discriminating variable is constructed.
The $hZ \to b\bar{b}q\bar{q}$ channel is characterised by high multiplicity and large visible energy. The events are clustered into 4 jets. Background from $q\bar{q}$ is removed by exploiting variables such as the DURHAM Y_{34} parameter, jet masses, the minimal jet energy and the maximal energy difference between any two jets. The large background contribution

Error Source	Relative error (%) for							
	bbee		bb$\mu\mu$		bb$\tau\tau$		$\tau\tau$qq	
	Sig	Bkg	Sig	Bkg	Sig	Bkg	Sig	Bkg
Lepton Identification	1.5	1.5	4.8	4.6	3.0	3.0	2.8	3.2
Energy Scale	0.1	0.8	0.0	0.5	1.8	6.5	3.9	9.0
Background Normalisation	–	2.6	–	4.1	–	1.8	–	1.3
Theory Signal	1.0	–	1.0	–	1.0	–	1.0	–
Luminosity	0.3	0.3	0.3	0.3	0.3	0.3	0.3	0.3
Total	1.8	3.1	4.9	6.2	3.6	7.4	4.9	9.6

Table 5.6: *Systematic errors for the SM Higgs search for the signal (Sig) and the background (Bkg).*

from WW $\rightarrow$ q$\bar{\text{q}}$q$\bar{\text{q}}$ is reduced by splitting the sample into two pieces. First, a kinematic fit is performed which imposes energy and momentum conservation and constraints the two di-jet masses to be equal. Then, a sliding cut on the resulting mass from this fit is placed, which depends on the Higgs mass hypothesis. The actual cut value is chosen by a cut optimiser [80]. This results in a low and a high purity sample. The low purity sample contains most of the properly reconstructed WW background, whereas the signal is contained in both samples with about equally large portions. Events with low b-tag values are removed in both samples. A mass χ^2 [80] that the event is consistent with the production of two particles with masses m_h and m_Z is calculated. The final variable is the weighted probability that an event is consistent with the background distributions of both the b-tag and the χ^2. Examples are shown in Figure 5.18 for $m_h = 95$ GeV.
The signature of the hZ $\rightarrow$ b$\bar{\text{b}}\nu\bar{\nu}$ channel is two acoplanar jets with large transverse missing momentum. The analysis is performed using a neural network. This network exploits variables such as b-tag, transverse imbalance, jet masses, the recoil mass to the jets and quality criteria on the kinematic fit. The final variable is called Purity [89], which is a convolution of the neural network output and the reconstructed Higgs mass. It is shown for $m_h = 95$ GeV in Figure 5.18. No indication of a signal was found in the two channels. A systematic error of 5% on the signal and 10% on the number of background events is assigned.

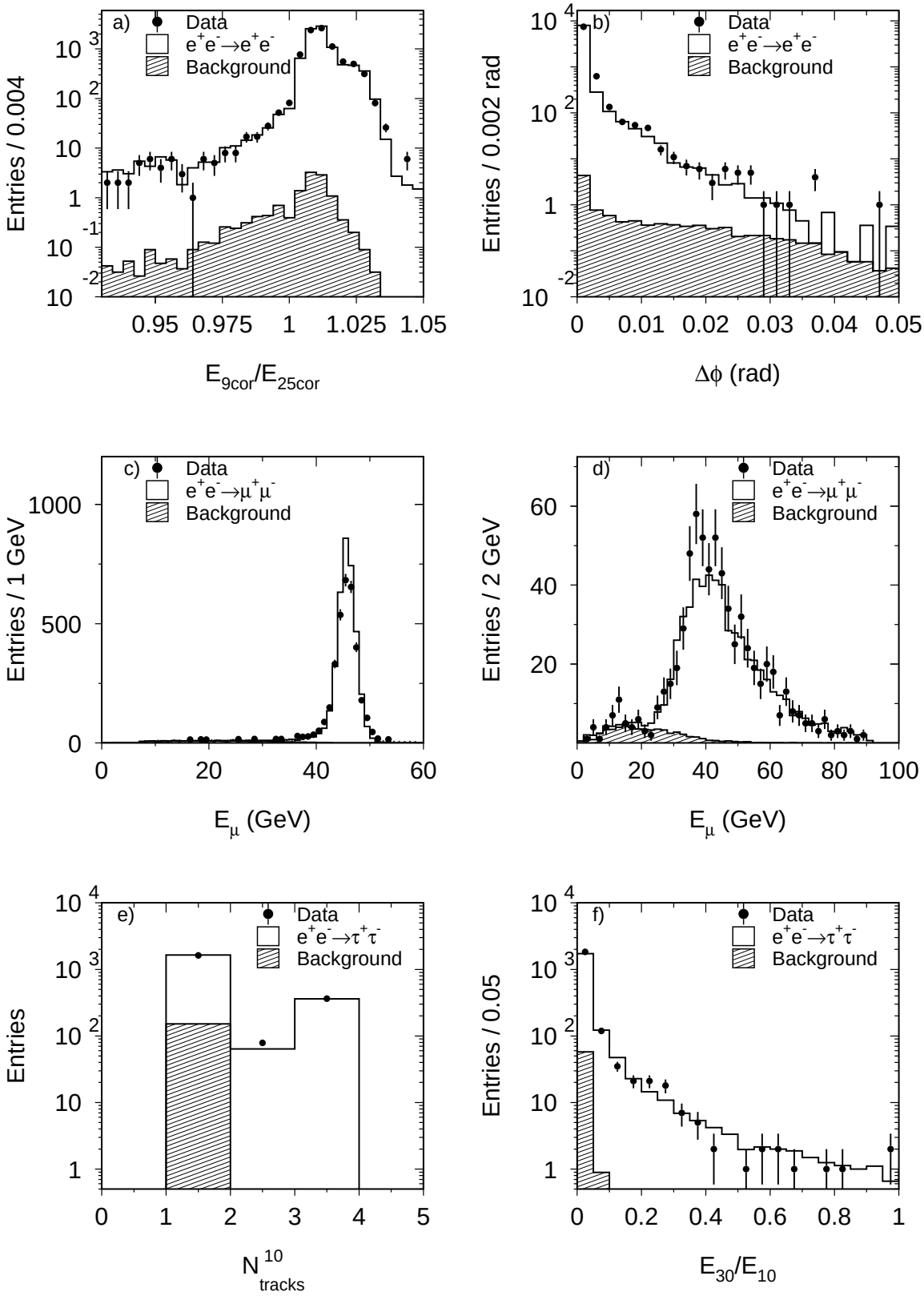

Figure 5.16: *Distributions of a) corrected energy ratio* E_{9cor}/E_{25cor}*, b) track–bump matching in* ϕ*, c) muon energy distribution (Z peak data) for triplets, d) muon energy distribution (Z peak data) for doublets, e) number of tracks within a 10 degree cone for a tau candidate, f) energy ratio* E_{30}/E_{10} *for tau candidates.*

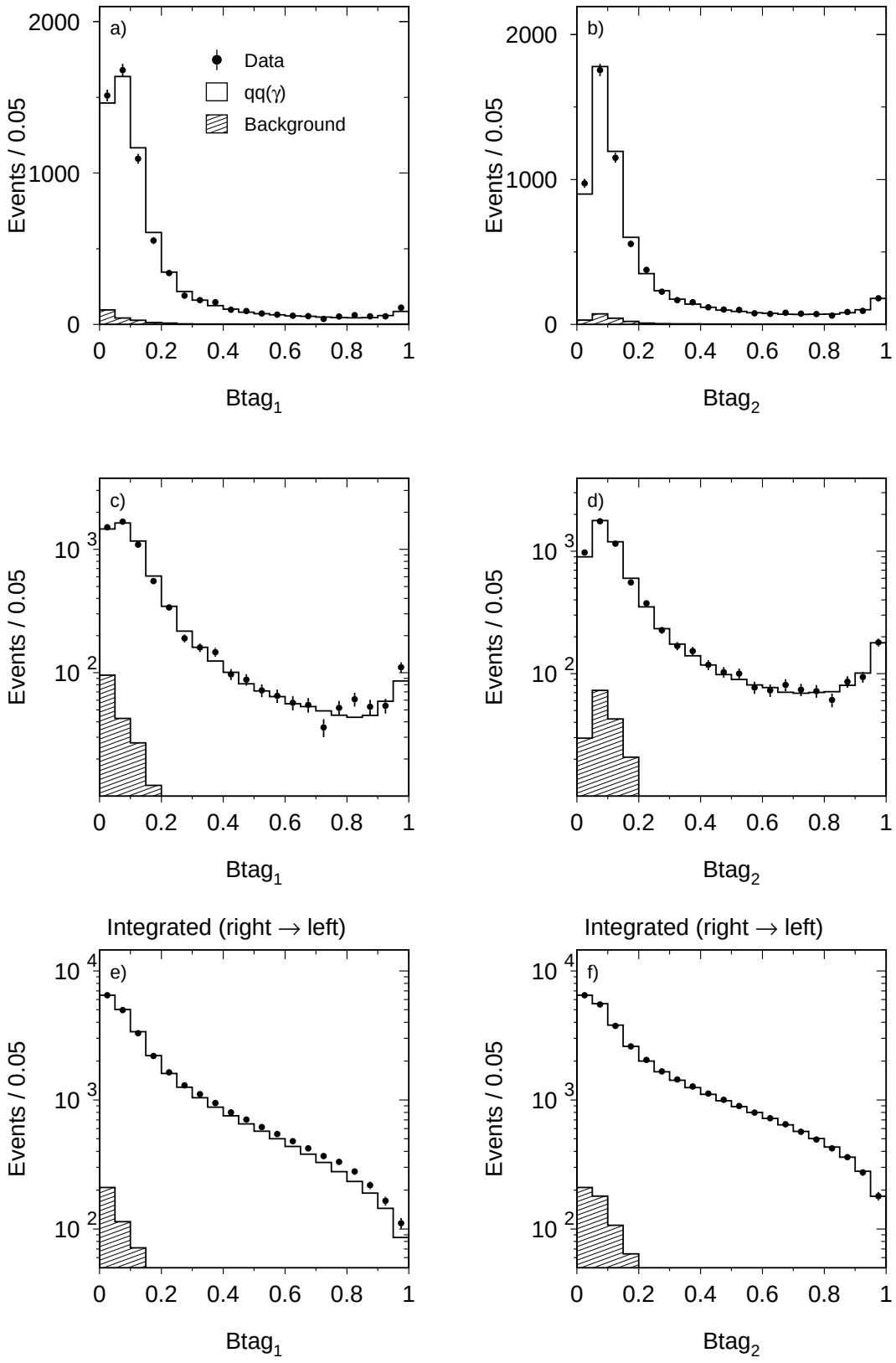

Figure 5.17: *B-tag of first (left) and second (right) most energetic jet in a reference sample of radiative $q\bar{q}(\gamma)$ events: a)–b) in linear scale, c)–d) in logarithmic scale and e)–f) from right to left integrated distributions in logarithmic scale.*

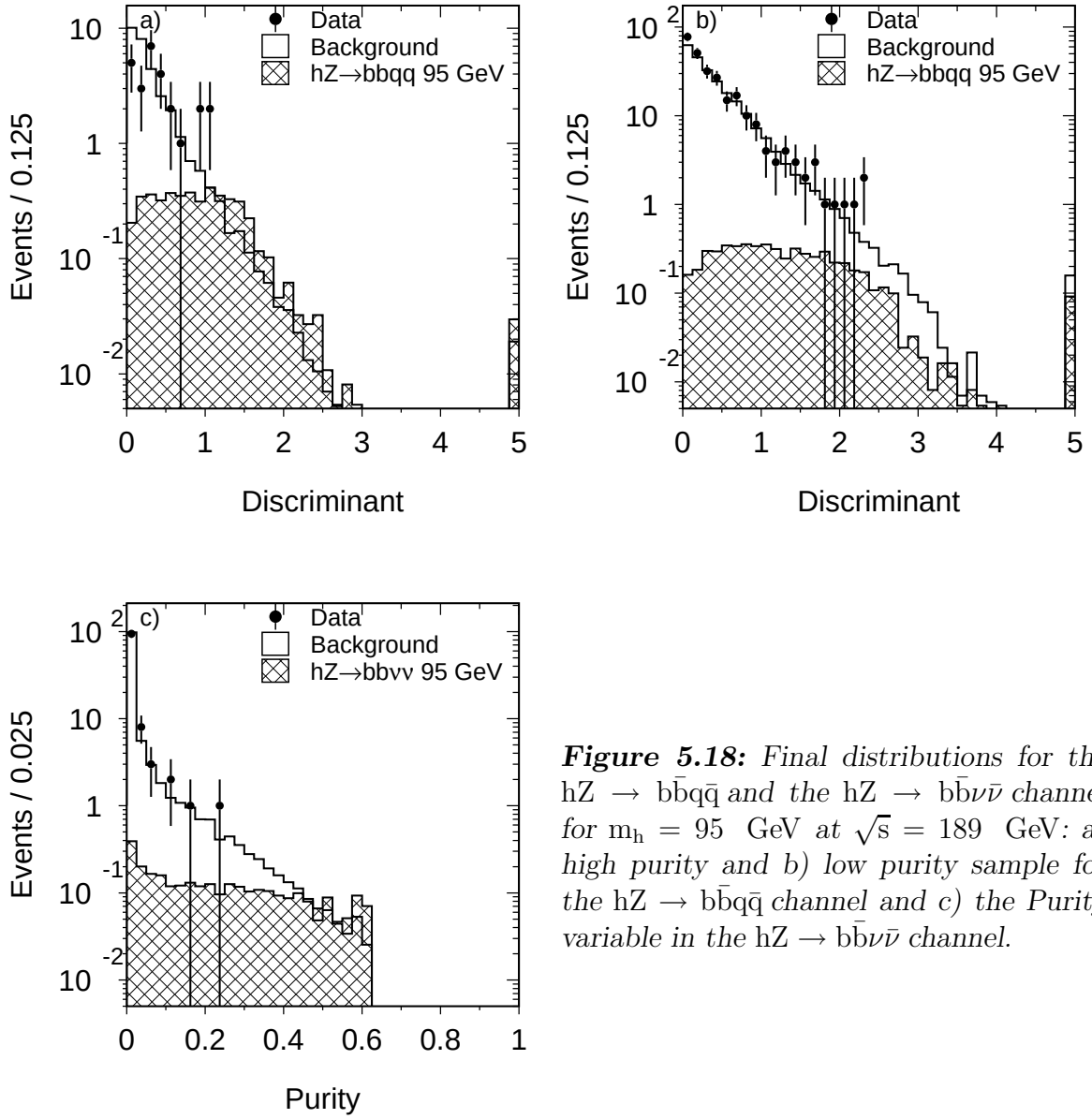

Figure 5.18: *Final distributions for the* $\mathrm{hZ} \to \mathrm{b\bar{b}q\bar{q}}$ *and the* $\mathrm{hZ} \to \mathrm{b\bar{b}}\nu\bar{\nu}$ *channel for* $\mathrm{m_h} = 95$ GeV *at* $\sqrt{\mathrm{s}} = 189$ GeV*: a) high purity and b) low purity sample for the* $\mathrm{hZ} \to \mathrm{b\bar{b}q\bar{q}}$ *channel and c) the Purity variable in the* $\mathrm{hZ} \to \mathrm{b\bar{b}}\nu\bar{\nu}$ *channel.*

Chapter 6

Search for Neutral Higgs Bosons in the MSSM

As discussed in section 2.3.3 there are 3 neutral Higgs bosons predicted within the minimal supersymmetric extension of the Standard Model. Two of those could be observed at LEP. The main production modes are the Higgs-strahlung $e^+e^- \to hZ$ and the associated pair production $e^+e^- \to hA$. These two are complementary, the first being dominant at low $\tan\beta$ whereas the second is predicted to be the main production mode at high $\tan\beta$. The most important decay modes are the decays into $b\bar{b}$ and $\tau^+\tau^-$. For the Higgs-strahlung the SM analyses can be reused. Dedicated selections have been performed for the $hA \to b\bar{b}b\bar{b}$ and $hA \to b\bar{b}\tau^+\tau^-$[1] final states. The latter was developed in this thesis and is described in more detail in the following section.

6.1 The $hA \to b\bar{b}\tau^+\tau^-$ Channel

The analysis is performed in a very similar way as for the $hZ \to b\bar{b}\tau^+\tau^-$ and the $hZ \to \tau^+\tau^- q\bar{q}$ channels, however the Z mass information can not be exploited and has to be compensated by other variables.
As in the SM Higgs search, a particle- and a jet-based selection are performed. Events are accepted if they pass either of the two selections. The major differences to the SM Higgs search are emphasised in the following. The cuts on the opening angles have been dropped to allow sensitivity to lower Higgs masses. The invariant masses of the tau-tau and the jet-jet system (obtained from a kinematic fit) are allowed to lie between 5 and 125 GeV. The increase in background is controlled by introducing additional variables reflecting differences of the expected signal to the background. The ratio of the energy sum of the visible decay products of the taus and the sum of the energy assigned to the hadronic jets, $(\frac{E^{dec}_{\tau 1}+E^{dec}_{\tau 2}}{E_{j1}+E_{j2}})$, must be smaller than or equal one. The energy of the Higgs decay products depend strongly on the Higgs mass. The ratio defined above, however, is independent for most of the parameter space. Only for large mass differences between h and A, the energy boost of the taus could result in energies of the tau decay products in a significant excess to the energy assigned to the jets. This, however, would correspond

[1] The $hA \to \tau^+\tau^- b\bar{b}$ channel is also considered.

to low $\tan\beta$ values, where the Higgs-strahlung is dominant. In the parameter space, where hA production is important (high $\tan\beta$), h and A have almost equal masses.

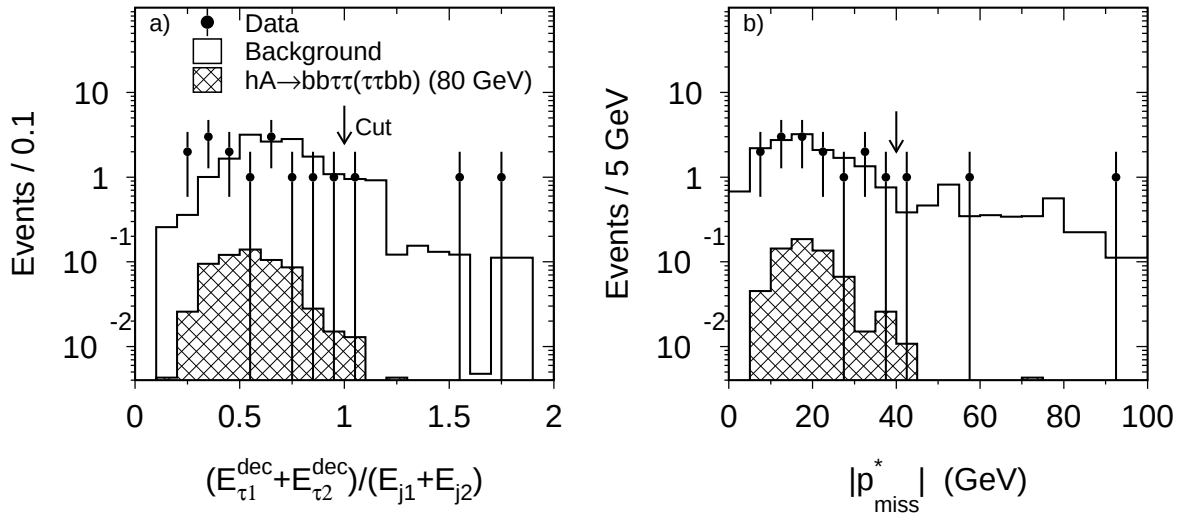

Figure 6.1: *Distributions for the jet based selection. All cuts, except the cut on the displayed quantity, have been applied. Shown are a) the ratio of the sum of the energy of the visible decay products of the τ candidates and the energy sum of the two hadronic jets and b) the missing momentum vector in the rest-frame of the particle decaying into the taus.*

	Particle-based selection	Jet-based selection
N_{tracks}	≥ 5	≥ 5
$N_{Cluster}$	≥ 15	≥ 15
$E_{vis}/\sqrt{s}$	≥ 0.4, ≤ 0.95	≥ 0.4, ≤ 0.9
E_e, E_μ, E_γ	≤ 40 GeV	≤ 40 GeV
$\ln Y_{34}$	≥ -6	≥ -6
p_T^{miss}	≥ 5 GeV	≥ 5 GeV
$\frac{E^{dec}_{\tau 1}+E^{dec}_{\tau 2}}{E_{j1}+E_{j2}}$	≤ 1	≤ 1
$m_{\tau\tau}$, m_{qq}	≥ 5 GeV, ≤ 125 GeV	≥ 5 GeV, ≤ 125 GeV
$\lvert \cos\theta \rvert$	≤ 0.8	≤ 0.8
$\lvert p^*_{miss} \rvert$	≤ 40 GeV	≤ 40 GeV
$\lvert \cos\theta_{miss} \rvert$	–	≤ 0.95
$\alpha_{\tau j}$	–	$\geq 25°$

Table 6.1: *Cuts applied in the hA selection.*

The missing momentum vector is transformed into the rest-frame of the Higgs which is

decaying into taus. In this frame the tau leptons are back-to-back, and the neutrinos are expected to be boosted into the flight direction of the tau. Therefore, the missing momentum vectors associated with the tau neutrinos should partially cancel. An upper cut on the absolute value of the missing momentum vector of 40 GeV in this frame is placed (see Figure 6.1). Furthermore, the production angle of the Higgs bosons is exploited. They are both scalars, and their production follows a $\sin^2\theta$ dependence. The production angle is required to satisfy $|\cos\theta| \leq 0.8$. The full set of cuts can be found in Table 6.1. After the selection, there are 20 events observed in the data with a background expectation of 16.6 events and a signal efficiency of 35% at 80 GeV. Table 6.2 summarises the background expectation and the signal efficiencies for the hZ (the events have passed the $hZ \to b\bar{b}\tau^+\tau^-$ or the $hZ \to \tau^+\tau^- q\bar{q}$ selections) and the hA selection. The acceptance

Selection of	Efficiency in (%)			Background from				Total	Data
	hA →	hZ →							
	$b\bar{b}\tau^+\tau^-$	$b\bar{b}\tau^+\tau^-$	$\tau^+\tau^- q\bar{q}$	WW	qq	ZZ	Zee		
hA	35.2	27.1	28.2	11.3	2.3	2.6	0.4	16.6	20
hZ	37.5	35.8	35.2	11.3	2.3	3.3	0.7	17.6	15
hA or hZ	39.9	37.5	37.6	17.4	3.9	4.0	0.9	26.2	26

Table 6.2: *Comparison of background expectation and signal efficiencies ($m_h = m_A = 80$ GeV) for the hZ and hA selections at $\sqrt{s} = 189$ GeV. Here, hZ denotes the* $hZ \to b\bar{b}\tau^+\tau^-$ *and the* $hZ \to \tau^+\tau^- q\bar{q}$ *selections (the events have passed either of the two).*

of the $hA \to b\bar{b}\tau^+\tau^-$ selection for various Higgs masses is shown in Table 6.3. As in the

	m_A (GeV)	50	60	70	80	80	90	100	100
	m_h (GeV)	50	60	70	80	70	70	70	80
$\epsilon_{hA\to b\bar{b}\tau^+\tau^-}$ (%)		38.0	38.8	38.9	35.2	37.3	32.2	27.5	26.4
$\epsilon_{hA\to\tau^+\tau^- b\bar{b}}$ (%)		39.2	43.3	35.9	34.3	33.9	36.4	28.2	26.5

Table 6.3: *Efficiency of the* $hA \to b\bar{b}\tau^+\tau^-$ *and* $hA \to \tau^+\tau^- b\bar{b}$ *sample for various Higgs mass combinations at* $\sqrt{s} = 189$ *GeV.*

SM Higgs analysis, the presence of a Higgs signal is tested by constructing a discriminant variable as described in section 5.1.5. The two neural net b-tags of the hadronic jets and the invariant masses, $m_{\tau\tau}$ and m_{qq}, are used as input. The distributions of these variables are shown in Figure 6.2. There is some small excess of events observed with high b-tag values. This gets more apparent if one integrates the b-tag distributions from right to left as shown in Figure 6.3. The excess can be partly related to the small deviation of the b-tag spectrum discussed in section 5.6 or it can be a purely statistical fluctuation, and at this stage we can also not exclude the presence of a Higgs signal. A qualitative estimate can be given by looking at the mass $m_{qq} + m_{\tau\tau}$. We expect Higgs decays into $\tau\tau$

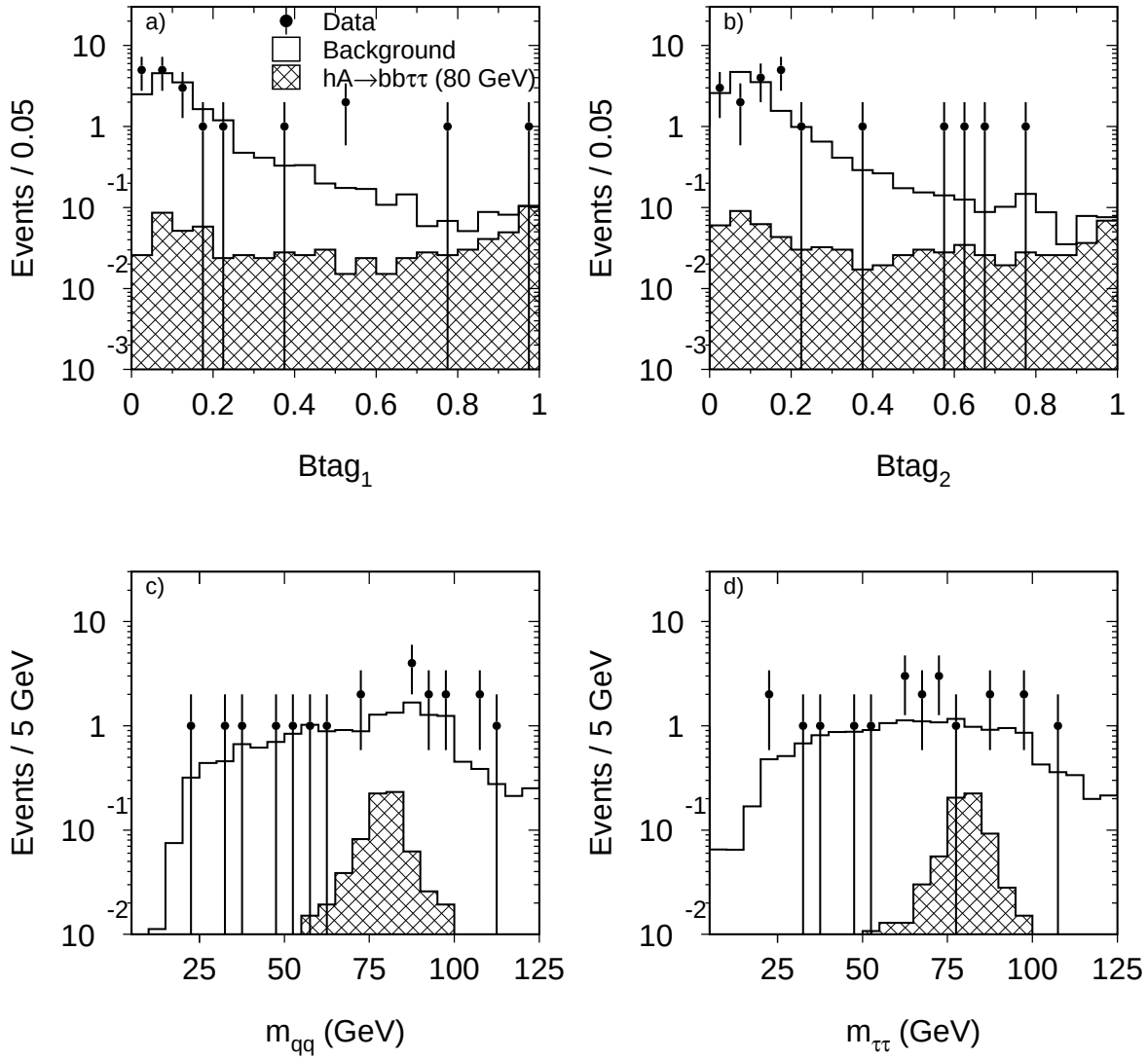

Figure 6.2: *Distributions used for the construction of the final discriminant in the* $\mathrm{hA \to b\bar{b}\tau^+\tau^-}$ *channel.*

and $\mathrm{b\bar{b}}$. If the masses h and A are different, a clustering of events should not necessarily be visible in the individual distributions $\mathrm{m}_{\tau\tau}$ and m_{qq} since the expected signal is very small. A more pronounced picture is expected for the sum of the masses. This is shown in Figure 6.4 for different cuts on the b-tags of the jets. The expected hA signal at $\mathrm{m_A} = 80$ GeV and $\tan\beta = 50$ is also shown. At this $\tan\beta$ value, $\mathrm{m_h}$ is equal to $\mathrm{m_A}$. No clustering of events is observed. The overall observed candidates are statistically compatible with the expectation from the background. However, significant candidates exist for different Higgs mass hypotheses. For a more quantified interpretation, the mass dependent discriminant is calculated as described above as a function of $\mathrm{m_A}$ and $\tan\beta$. As can be seen from Table 6.2, there is a large event overlap between the hZ and the

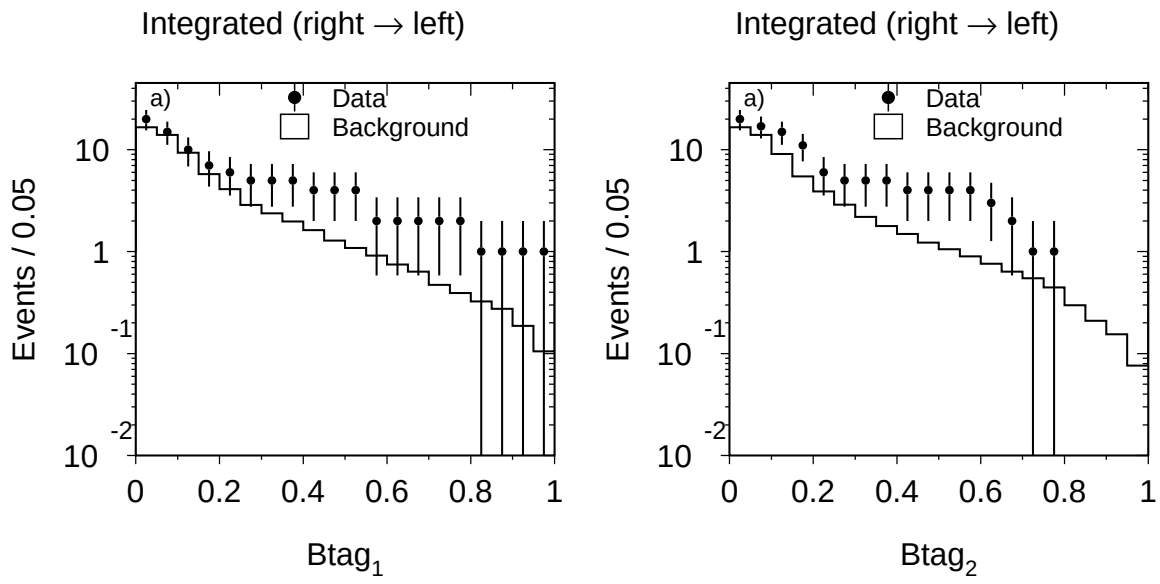

Figure 6.3: *Integrated b-tag spectrum for the* $\mathrm{hA} \rightarrow \mathrm{b\bar{b}}\tau^+\tau^-$ *channel at* $\sqrt{\mathrm{s}} = 189$ GeV.

hA selections. This overlap has to be taken into account in the construction of the final discriminant. Since the relative rate of the expected hZ and hA signal changes with $\tan\beta$ and $\mathrm{m_A}$, not only the events kinematics (as in the case of the SM tau channels) but also the different cross sections have to be taken into account in order to obtain the maximal possible sensitivity at every $\mathrm{m_A}$–$\tan\beta$ point. There are in total 4 possible final states: $\mathrm{hZ} \rightarrow \mathrm{b\bar{b}}\tau^+\tau^-$, $\mathrm{hZ} \rightarrow \tau^+\tau^-\mathrm{q\bar{q}}$, $\mathrm{hA} \rightarrow \mathrm{b\bar{b}}\tau^+\tau^-$ and $\mathrm{hA} \rightarrow \tau^+\tau^-\mathrm{b\bar{b}}$. Events are uniquely assigned to one channel in the following way. The likelihood values $\mathrm{F_{hZ\rightarrow b\bar{b}\tau^+\tau^-}}$, $\mathrm{F_{hZ\rightarrow\tau^+\tau^-q\bar{q}}}$, $\mathrm{F_{hA\rightarrow b\bar{b}\tau^+\tau^-}}$ and $\mathrm{F_{hA\rightarrow\tau^+\tau^-b\bar{b}}}$ for an event are compared taking the expected cross section as a weight into account and the event is placed in the channel with the highest cross section weighted likelihood value[2]. Examples for hA are shown in Figure 6.5 at $\tan\beta = 50$ and for $\mathrm{m_A}$ masses of 55 GeV and 80 GeV. As $\mathrm{m_A} = \mathrm{m_h}$ at this $\tan\beta$ value, the two discriminant spectra for $\mathrm{hA} \rightarrow \mathrm{b\bar{b}}\tau^+\tau^-$ and $\mathrm{hA} \rightarrow \tau^+\tau^-\mathrm{b\bar{b}}$ have been added for better visibility. These values have been chosen because they are close to the sensitivity of this analysis ($\mathrm{m_A} = 55$ GeV) alone and in combination with the four-jet channel $\mathrm{hA} \rightarrow \mathrm{b\bar{b}b\bar{b}}$ ($\mathrm{m_A} = 80$ GeV). For $\mathrm{m_A} = 55$ GeV a significant candidate is observed. The question on the existence or non-existence of Higgs bosons for a large portion of the possible parameter space can be answered only in combination with the $\mathrm{hA} \rightarrow \mathrm{b\bar{b}b\bar{b}}$ channel, where the signal expectation is much higher due to the larger branching ratio of the Higgs bosons into b-quarks. This will be discussed in chapter 8. The results of the 183 GeV analysis are summarised in appendix B. Good agreement between the observed candidates and the background expectation was found in that data sample.

[2]Events, which are placed in the $\mathrm{hZ} \rightarrow \mathrm{b\bar{b}}\tau^+\tau^-$ or the $\mathrm{hZ} \rightarrow \tau^+\tau^-\mathrm{q\bar{q}}$ channels and which were already selected in the $\mathrm{hZ} \rightarrow \mathrm{b\bar{b}e^+e^-}$ or $\mathrm{hZ} \rightarrow \mathrm{b\bar{b}}\mu^+\mu^-$ channels, are rejected to avoid double counting in the combination. The effect of the event overlap between the $\mathrm{hA} \rightarrow \mathrm{b\bar{b}}\tau^+\tau^-$ and the $\mathrm{hZ} \rightarrow \mathrm{b\bar{b}e^+e^-}$ ($\mathrm{hZ} \rightarrow \mathrm{b\bar{b}}\mu^+\mu^-$) selections was found to be negligible.

Systematic Errors:
The systematic errors are derived as described in section 5.6 and are summarised in Table 6.4.

Error Source	Relative error (%) on Signal	Background
Lepton Identification	2.9	2.8
Energy Scale	1.0	7.0
Background Normalisation	–	1.7
Theory Signal	1.0	–
Luminosity	0.3	0.3
Total	3.2	7.7

Table 6.4: *Systematic errors for the MSSM Higgs search.*

6.2 The $\mathbf{hA \to b\bar{b}b\bar{b}}$ Channel

The four-jet channel is very similar to the $hZ \to b\bar{b}q\bar{q}$ channel. A detailed description can be found in References [91, 92]. The same variables as in the $hZ \to b\bar{b}q\bar{q}$ channel are used complemented with the Higgs production angle. The actual cut values are chosen by a cut optimiser, which optimises the signal-over-background ratio at four parameter points close to the discovery potential[3]. Events passing the optimised cuts are placed into three categories: 1) those that pass only the hA cuts (hA), 2) those that pass only the hZ cuts (hZ) and 3) those that pass both set of cuts. Category (3) is then split into two separate samples by choosing the most likely production hypothesis based on the probability of the χ^2 of the mass hypothesis and the relative production rates of hA and hZ. If the hZ hypothesis is more likely, then the event is classified as hZ′; otherwise, it is called hA′. Finally, a discriminant variable is constructed in the same way as in the SM four-jet analysis for all 4 sub-categories. These discriminants are recalculated at every parameter point and used to probe a given Higgs mass hypothesis. The observed candidates are in agreement with the expectation from SM background processes. A systematic error of 5% on the signal and 10% on the background is assigned for this channel.

6.3 The $\mathbf{hZ \to AAf\bar{f}}$ Channel

To investigate h decays into A-pairs in the region of very low $\tan\beta$ and low m_A, where this channels becomes dominant, the hZ four jet analysis is employed without adjustment. The signature of this process is at least four hadronic jets with very high probabilities to contain b-quarks. The efficiency on $hZ \to AAZ \to b\bar{b}b\bar{b}q\bar{q}$ is above 40% over the region

[3]The $hZ \to b\bar{b}q\bar{q}$ channel is not split into a low and a high purity sample as in the SM Higgs analysis.

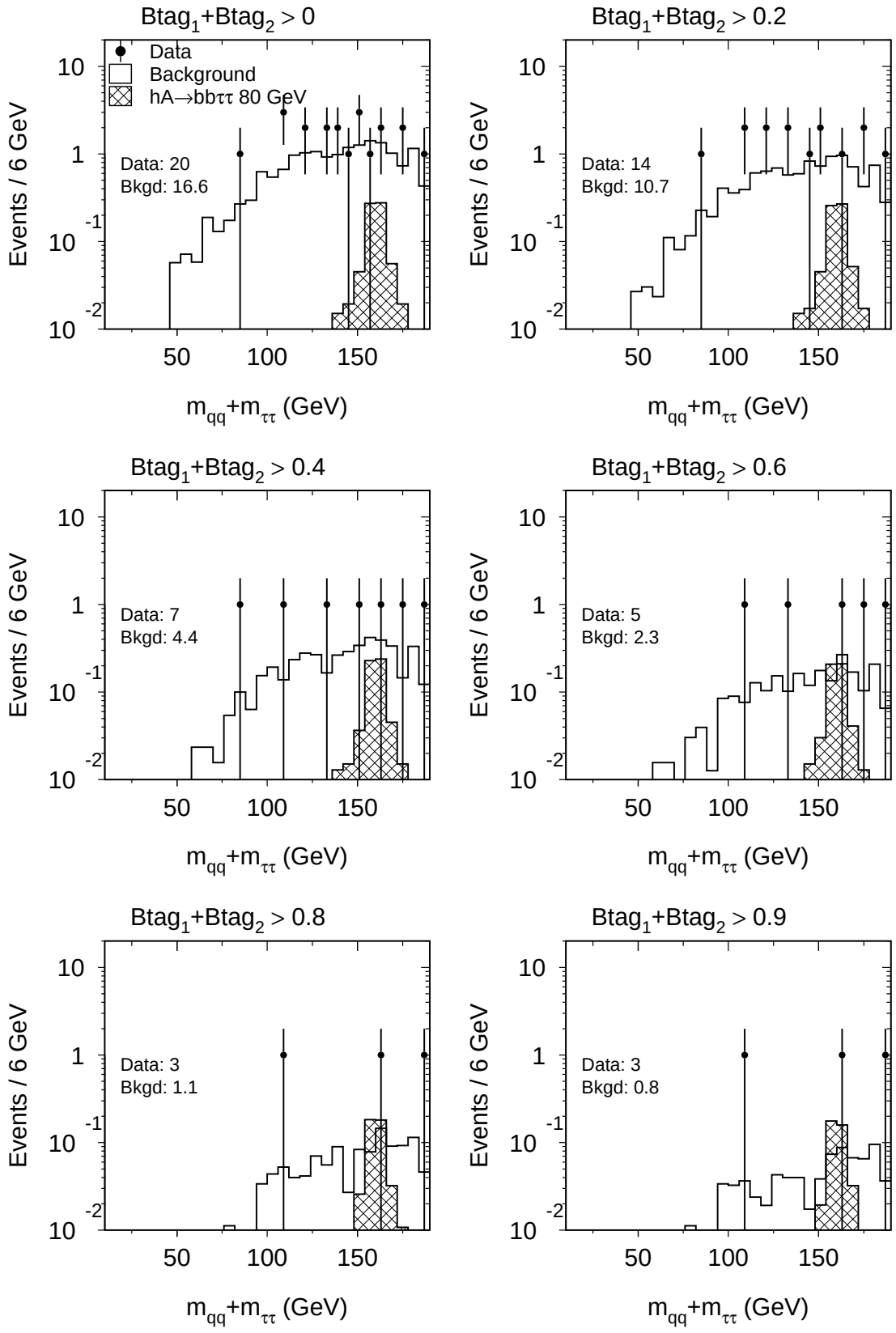

Figure 6.4: *Sum of the invariant masses of the tau-tau and the jet-jet system in the MSSM Higgs search for different b-tag values. The overall background expectation and the observed number of candidates are also shown.*

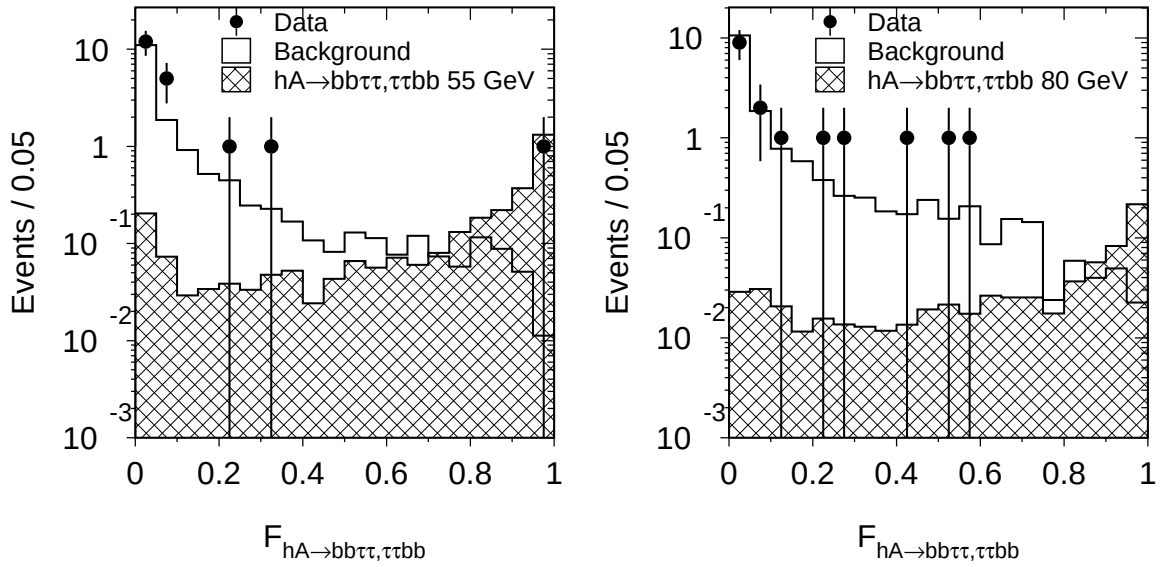

Figure 6.5: *Final discriminant spectrum in the* $\mathrm{hA} \rightarrow \mathrm{b\bar{b}}\tau^+\tau^-$ *channel for* $\mathrm{m_h} = \mathrm{m_A} = 55$ GeV *and* $\mathrm{m_h} = \mathrm{m_A} = 80$ GeV *corresponding to* $\tan\beta = 50$ *in the minimal mixing scenario.*

of interest. The mass χ^2 of the four jet analysis is less effective in the six jet topology, however, the b-tag gives the final variable enough discriminating power to distinguish between signal and background.

Chapter 7

Search for Charged Higgs Bosons

Following the discussion in section 2.5.3, the search for charged Higgs bosons is performed in three channels:

- in the $H^+H^- \to c\bar{s}\bar{c}s$ channel
- in the $H^+H^- \to c\bar{s}\tau^-\bar{\nu}_\tau$ channel[1]
- in the $H^+H^- \to \tau^+\nu_\tau\tau^-\bar{\nu}_\tau$ channel

The sum of the branching fractions $Br(H^\pm \to \tau\nu)$ and $Br(H^\pm \to cs)$ is assumed to be one[2]. In this thesis the $H^+H^- \to c\bar{s}\tau^-\bar{\nu}_\tau$ channel was analysed which will be discussed in the following.

7.1 The $H^+H^- \to c\bar{s}\tau^-\bar{\nu}_\tau$ Channel

The $H^+H^- \to c\bar{s}\tau^-\bar{\nu}_\tau$ is characterised by two hadronic jets, a τ lepton and missing energy due to the presence of at least two neutrinos, one arising from the decay of $H^\pm \to \tau\nu$ and one coming from the τ decay. If the τ decays into an electron or a muon, one more neutrino will be present in order to conserve the lepton flavour.
The main background comes from $WW \to qq\ell\nu$ which is especially severe if ℓ is a τ lepton, leading to almost the same signature with the only difference being that the mother particle (W) is a spin-1 particle whereas the Higgs is a scalar. This difference is reflected in the production angle.
High multiplicity events are selected requiring at least 5 charged tracks and 10 calorimetric clusters. The visible energy must be within $0.35\sqrt{s}$ and $1.0\sqrt{s}$. A major fraction of $q\bar{q}(\gamma)$ and two-photon interactions is removed by requiring that $|\cos\theta_{miss}| \leq 0.95$, $p_T^{miss} \geq 5$ GeV and and $E_\gamma \leq 50$ GeV. The energy, accumulated in the luminosity monitor, E_{Lumi}, must not exceed 15 GeV.

[1] The charge conjugated channel is also considered.

[2] As there will be no quark flavour tagging applied in the analysis, the interpretation of section 8.4 remains valid even if there is a non-vanishing branching fraction into cb or any other quark pair.

One τ lepton is required to be identified as described in section 5.1.1. After these requirements 927 events are observed in the data with a background expectation of 936.9 events and a signal efficiency of 55% at $m_H^{\pm} = 75$ GeV. Selected events are forced into two jets using the DURHAM algorithm, after subtracting the τ candidate. Figure 7.1 shows the distributions of the visible mass of the jet-jet system, m_{qq}^{vis}, and the energy of the decay products of the τ, E_τ^{dec} at this stage of the analysis. The visible mass, m_{qq}^{vis}, must be smaller than 110 GeV and the energy of the visible decay products of the τ lepton less than 50 GeV to reduce $q\bar{q}(\gamma)$ contamination. The same background is further

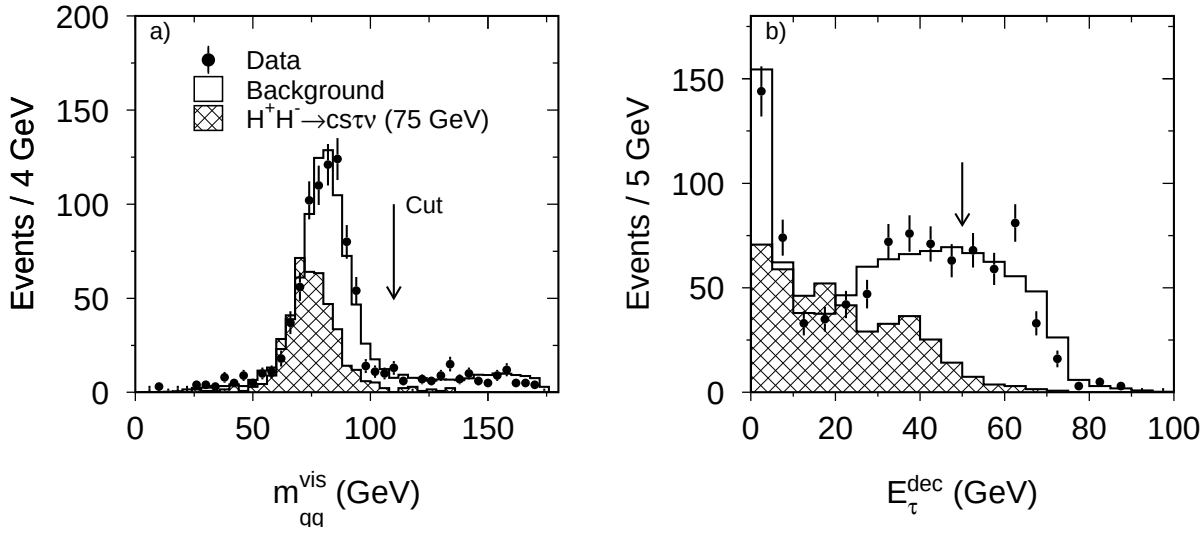

Figure 7.1: *Comparison of data and background for the* $H^+H^- \to c\bar{s}\tau^-\bar{\nu}_\tau$ *channel after preselection as described in the text. a) Visible mass of the jet-jet system, b) Energy of the decay products of the* τ *lepton. The expected signal for a 75 GeV Higgs boson at* $Br(H^\pm \to \tau\nu) = 0.5$ *multiplied by a factor of 50 is superimposed.*

reduced by requiring the missing transverse momentum to exceed 25 GeV, the missing momentum parallel to the beam axis to be smaller than 50% of the visible energy and the direction of the missing momentum vector to satisfy $|\cos\theta_{miss}| < 0.9$. The sum of the opening angles of the τ candidate and the missing momentum vector to the closest jet, $\alpha_{mj} + \alpha_{\tau j}$, must be larger than 70° (see Figure 7.2 a)).
A kinematic fit is performed imposing energy and momentum conservation for an assumed production of a pair of equal mass particles with one decaying into two jets and the other into a τ and a neutrino. The directions of the τ and of the missing momentum vector are kept at their measured values and infinite energy resolution is assumed. Using this method, a resolution of about 4 GeV is obtained in the distribution of the effective mass of the two jets and of the τ and the neutrino. To further reject $q\bar{q}(\gamma)$, two–photon interactions and W pair events, the flight direction of the parent particle is considered. The production of the charged Higgs follows a $\sin^2\theta$ dependence whereas the major fraction of the background is collected in the forward-backward region of the

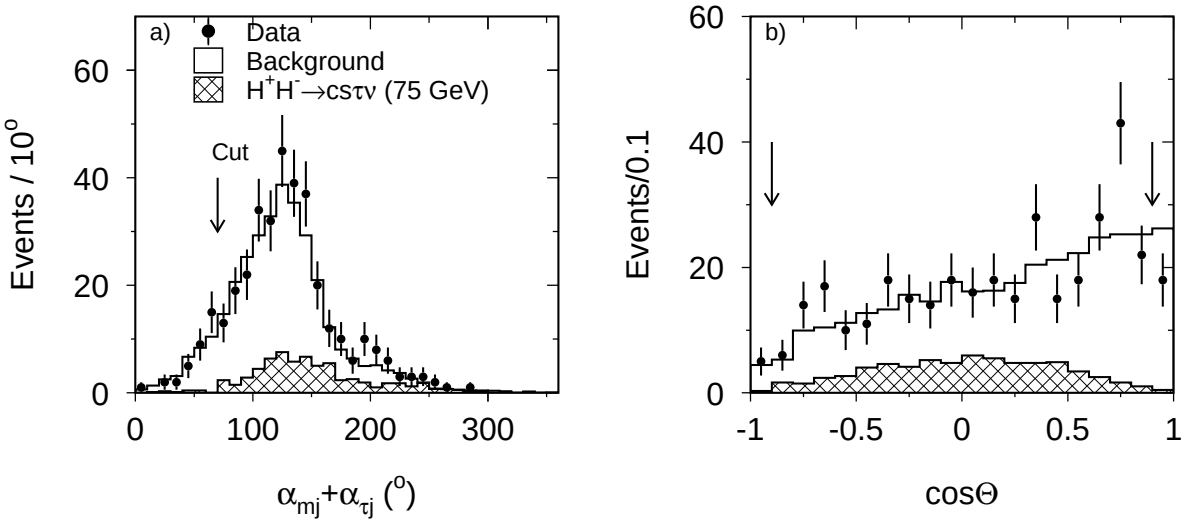

Figure 7.2: *Comparison of data and background for the* $\mathrm{H^+H^-} \to \mathrm{c\bar{s}}\tau^-\bar{\nu}_\tau$ *channel. All cuts are applied except the cut on the quantity which is shown. a) Sum of the opening angles of the missing momentum vector and the* τ *lepton to the closest jet, b)* $\cos\theta$ *distribution, where* θ *is the production angle of the negative mother particle. The expected signal for a 75 GeV Higgs boson at* $\mathrm{Br}(\mathrm{H^\pm} \to \tau\nu) = 0.5$ *multiplied by a factor of 10 is superimposed.*

detector. Events with $|\cos\theta| \leq 0.9$ are accepted (see Figure 7.2 b)).
Semileptonically decaying W-pairs ($\mathrm{WW} \to \mathrm{qq}\ell\nu,\ \ell = \mathrm{e}, \mu$) are suppressed in the following way. The four momenta are transformed into the rest frame of the leptonically decaying parent particle. In this frame, the lepton energy E^*_ℓ is greater if the lepton comes from a prompt W decay than from a τ decay. The missing momentum $|\mathrm{P}^*_{\mathrm{miss}}|$ is also larger in the first case because the neutrinos from the τ decay are almost oppositely directed to the τ neutrino coming directly from the W. For the selection, the sum $\mathrm{E}^*_\ell + |\mathrm{P}^*_{\mathrm{miss}}|$ is used, which should be smaller than 60 GeV for an electron and smaller than 50 GeV for a muon in the final state. This is illustrated in Figure 7.3.
The total number of events selected in data is 138, where 129.3 background events are expected from Standard Model processes. The background is dominated by the process $\mathrm{WW} \to \mathrm{qq}\tau\nu$ (73%) and other WW decays (24%). The remaining contributions are $\mathrm{q\bar{q}}(\gamma)$ and neutral current four-fermion events. The signal efficiencies are shown for various Higgs masses in Table 7.2.
For the final mass distribution, the average of the masses of the jet–jet and the $\tau\,\nu$ pairs, calculated after the kinematic fit, is used. Figure 7.4 shows the mass distribution for $\sqrt{\mathrm{s}} = 189$ GeV and for the combination of all data from 130 to 189 GeV. The observed candidates are consistent with the expectations from SM background processes. Details of the individual results at centre-of-mass energies below 189 GeV can be found in appendix C.

Systematic errors: Systematic errors are determined as described in section 5.6. The theory error corresponds to the difference in the cross section prediction using PYTHIA and the HZHA generator.

Error Source	Relative error (%) on Signal	Background
Lepton Identification	1.9	1.4
Energy Scale	0.5	1.4
Background Normalisation	–	1.9
Theory Signal	1.0	–
Luminosity	0.3	0.3
Total	2.2	2.8

Table 7.1: *Systematic errors for the* $\mathrm{H^+H^-} \to \mathrm{c\bar{s}}\tau^-\bar{\nu}_\tau$ *channel.*

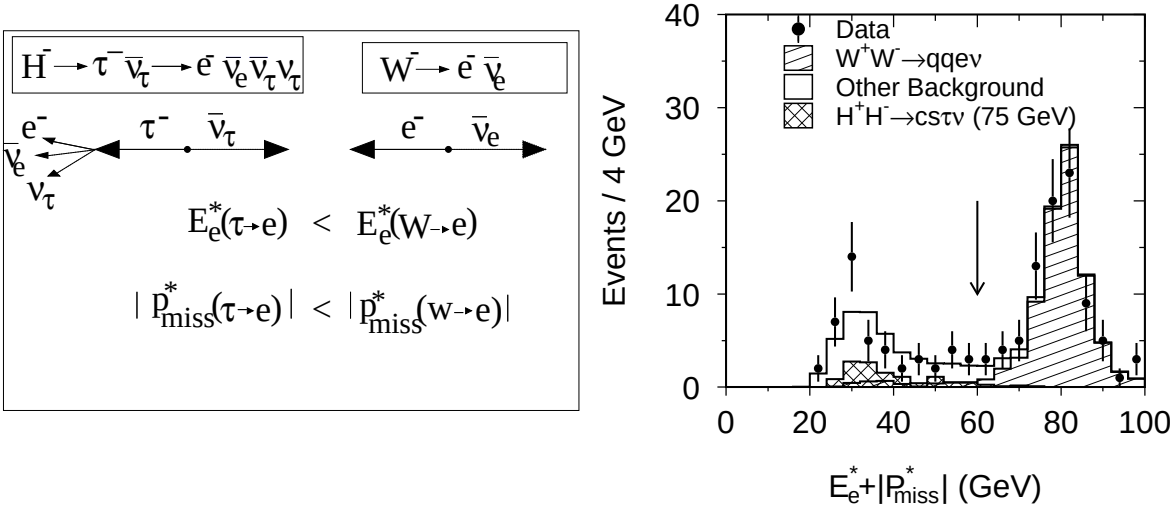

Figure 7.3: *Discrimination of the* $\mathrm{WW} \to \mathrm{qqe}\nu$ *background. Left: illustration of the different kinematics for* $\mathrm{H^\pm} \to \tau\nu \to e\nu\nu\nu$ *and* $\mathrm{W^\pm} \to e\nu$ *in the rest-frame of the leptonically decaying mother particle. Right: sum of the electron energy and the absolute value of the missing momentum vector in the rest-frame of the leptonically decaying mother particle for events with an identified electron in the final state after all other cuts have been applied.*

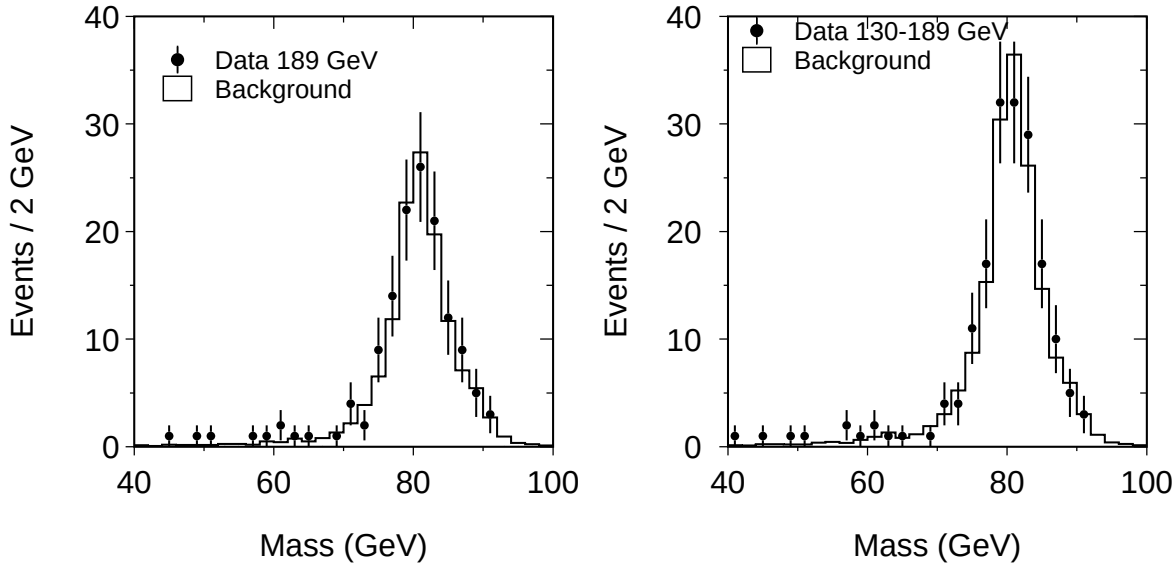

Figure 7.4: *Mass distribution after all cuts. Left: the 189 GeV data only. Right: all data from 130 to 189 GeV.*

7.2 The Other Channels

A detailed description of the analysis and the results in the other two channels can be found in References [93, 94]. In the $H^+H^- \to \tau^+\nu_\tau\tau^-\bar{\nu}_\tau$ channel low multiplicity events with a low visible energy are selected reflecting the expected signature of tau leptons with large missing energy due to the presence of neutrinos. Di-lepton production $e^+e^- \to \ell^+\ell^-$ ($\ell = e, \mu, \tau$), $WW \to \ell\nu\ell\nu$ and two-photon interactions are the most significant background sources. They are suppressed by making requirements on the opening angle between the visible decay products of the tau leptons and their energy. Furthermore, the transverse and longitudinal imbalance and energy depositions in the low angle calorimeters are exploited. As the mass of the Higgs can not be reconstructed, the total number of observed events is compared to the number of expected background events. This is shown in Table 7.2 for a centre-of-mass energy of 189 GeV. No excess in the number of candidates is observed.

The four-jet channel $H^+H^- \to c\bar{s}\bar{c}s$ is characterised by four hadronic jets, which are balanced in momentum leading to a high multiplicity and large visible energy in the detector. The major background sources are the fully hadronically decaying WW events and $q\bar{q}$ production with gluon radiation in the final state. High multiplicity events with large visible energy are selected. They are clustered into 4 jets using the DURHAM algorithm. Requirements on opening angles between the jets and on the production angle of the reconstructed mother particle are made. The reconstructed mass is used as the final variable to evaluate the existence of the signal. This mass is obtained from a kinematic fit, which imposes energy and momentum conservation and constrains the two di-jet masses to be equal. The distribution for $\sqrt{s} = 189$ GeV is shown in Figure 7.5. A small small excess in the 67 GeV region is observed, which is, however, fully compatible with a

Channel $H^+H^- \rightarrow$	Efficiency (%) for $m_H^{\pm}$ = 60 GeV	65 GeV	70 GeV	75 GeV	Background	Data
$\tau^+\nu_\tau\tau\bar{\nu_\tau}$	24	27	31	32	32.5	30
$c\bar{s}\tau\bar{\nu_\tau}$	44	42	40	39	129.3	138
$c\bar{s}\bar{c}s$	39	38	38	34	359.4	348

Table 7.2: *The signal efficiencies for various Higgs masses, the background expectations and the number of candidates.*

fluctuation of the background. The total number of observed candidates to the number of expected events is shown in Table 7.2 for a centre-of-mass energy of 189 GeV. The signal efficiencies for various Higgs masses are also given. An overall systematic error of 10% on the number of background events and 5% on the signal is assigned for these channels.

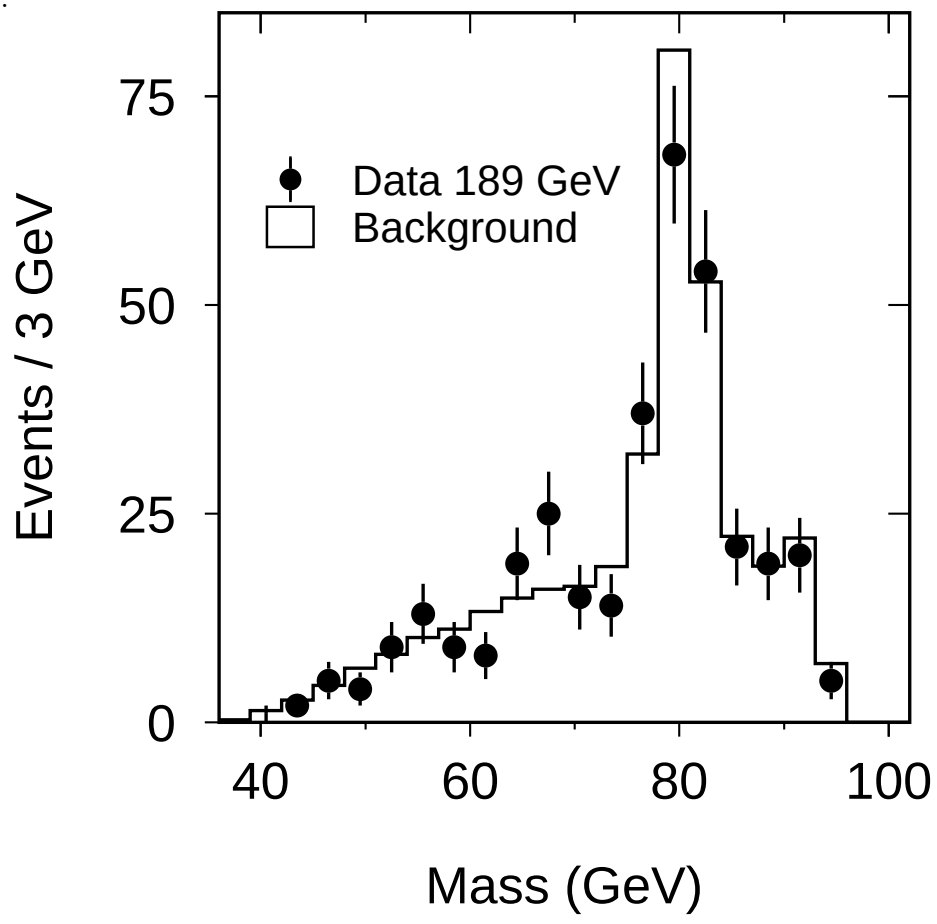

Figure 7.5: *Distribution of the mass resulting from a kinematic fit, with assumed production of a pair of equal mass particles, for data and background events in the* $H^+H^- \rightarrow c\bar{s}\bar{c}s$ *channel at* $\sqrt{s} = 189$ *GeV.*

Chapter 8

Interpretation

In the previous chapters the analyses and the results of the searches for the various Higgs bosons considered were presented. No apparent hint of a signal was found. In this chapter the results of the individual search channels are combined. As the expected signal is usually quite small, a possible deviation from the background expectation may only become apparent in the combination. If candidates show up at the same point in the parameter space considered, they may lead to a significant excess with respect to the background expectation. On the other hand, if the candidates in the individual channels are observed at different points, they lose significance.

8.1 Confidence Level Calculation

The method [95, 96] employed to calculate the confidence level that the signal is absent, allows also to evaluate the presence of a signal. The procedure is described in the following.
First, a binned likelihood based on Poisson statistics is constructed, using mass sensitive distributions[1] for the individual search channels at the different centre-of-mass energies:

$$\mathcal{L}(\mathrm{s}) = \prod_{k=1}^{l} \prod_{j=1}^{n_k} \prod_{i=1}^{m_{kj}} \frac{\mathrm{e}^{-(\mathrm{s}_{ijk}+\mathrm{b}_{ijk})}(\mathrm{s}_{ijk}+\mathrm{b}_{ijk})^{\mathrm{N}_{ijk}}}{\mathrm{N}_{ijk}!}. \tag{8.1}$$

Here, $k = 1..l$ runs over all investigated centre-of-mass energies, $j = 1..n_k$ over the search channels and $i = 1..m_{kj}$ over the bins of the distribution of a given channel j at the centre-of-mass energy k. The variables s_{ijk}, b_{ijk} and N_{ijk} represent the expected signal[2], the expected background and the number of observed candidates for the individual analyses, respectively. The total number of expected signal events, s, is given by:

$$\mathrm{s} = \sum_{k=1}^{l} \sum_{j=1}^{n_k} \sum_{i=1}^{m_{kj}} \mathrm{s}_{ijk}. \tag{8.2}$$

[1] As outlined earlier, the reconstructed mass is a very important variable because of its good resolution.

[2] At this point, we take advantage of the fact that the models make specific predictions on the signal as a function of the Higgs mass.

The background and signal expectations, b_{ijk} and s_{ijk}, are fixed to their Monte Carlo predictions. If no excess in the number of observed candidates in comparison to the background expectation is observed, the likelihood has its maximum at s = 0. In the next step, an estimator based on Bayesian statistics is constructed:

$$X_{Bay}(s) = \frac{\int_s^\infty \mathcal{L}(s')ds'}{\int_0^\infty \mathcal{L}(s')ds'}. \tag{8.3}$$

The confidence level to exclude a signal within the framework of Bayesian statistics is given by:

$$CL_{Bay} = 1 - X_{Bay}. \tag{8.4}$$

In order to take into account the possibility of background and signal fluctuations, we perform now a large number of reference Monte Carlo experiments based on Poisson statistics for two hypotheses:
a) background only
b) background + signal.
For all these experiments the Bayesian estimator is calculated and the confidence level to exclude a signal is defined as:

$$CL = 1 - \frac{P(X_{Bay}^{S+B} < X_{Bay}^{Obs})}{P(X_{Bay}^{B} < X_{Bay}^{Obs})}, \tag{8.5}$$

where P is the probability to obtain an estimator smaller than the observed X_{Bay}^{Obs} for hypothesis a) (X_{Bay}^{B}) and for hypothesis b) (X_{Bay}^{S+B}). The background only experiments can also be used to calculate an expected confidence level in the absence of a signal based purely on the Monte Carlo prediction for background and signal. The confidence level computed in this way indicates the sensitivity of the analysis. An example is shown in Figure 8.1 for the leptonic channels in the SM Higgs search at $m_h = 90$ GeV. There are commonly two ways used to quote the expected confidence level. The average CL is just the overall average of the CL distribution. The median CL is the confidence level, where the distribution is divided into two equally large portions, indicating that one would expect in 50% of the experiments a lower and in 50% a higher confidence level. As the latter is precisely defined independent of the shape of the CL distribution[3], we will use in the following the median expected CL. The same distribution can be used to extract the probability that the observed confidence level is consistent with the background only hypothesis. This is a strong indicator for a signal.

The systematic errors derived in the subsequent sections are incorporated in the confidence level calculation by smearing the background and signal expectations in the generation of the MC trial experiments according to a Gaussian distribution with a width of the corresponding error.

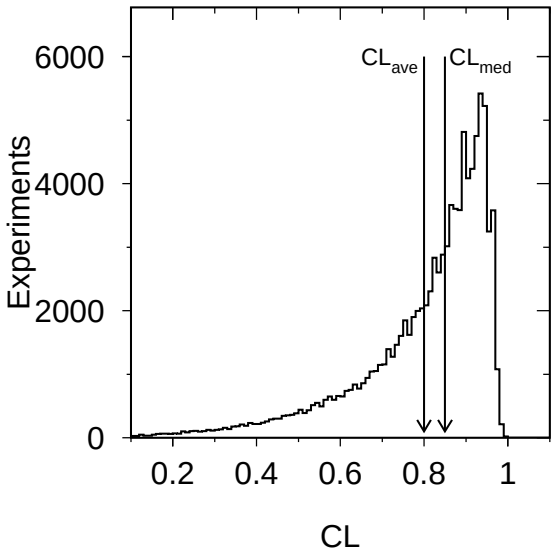

Figure 8.1: *Expected confidence level distribution derived from MC background only experiments combining the* $\mathrm{hZ} \to \mathrm{b\bar{b}}\ell^+\ell^-$ *(*$\ell = \mathrm{e}, \mu, \tau$*) and the* $\mathrm{hZ} \to \tau^+\tau^-\mathrm{q\bar{q}}$ *channel at centre-of-mass energies between 183 and 189 GeV at* $\mathrm{m_h} = 90$ *GeV.*

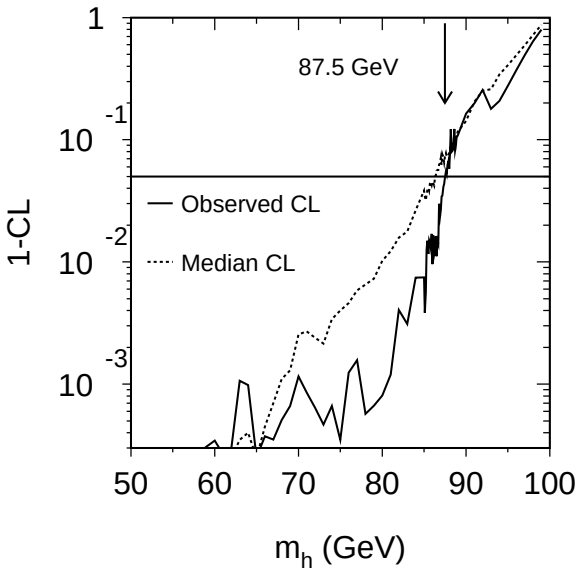

Figure 8.2: *The confidence level CL as a function of the Higgs mass combining the* $\mathrm{hZ} \to \mathrm{b\bar{b}}\ell^+\ell^-$ *(*$\ell = \mathrm{e},\ \mu,\ \tau$*) and the* $\mathrm{hZ} \to \tau^+\tau^-\mathrm{q\bar{q}}$ *channel at centre-of-mass energies between 183 and 189 GeV. The median expected confidence level is also shown.*

8.2 Mass Limit in the Standard Model

In the Standard Model the cross section for Higgs production depends only on the mass and the centre-of-mass energy. The branching ratios are precisely predicted. Therefore, mass limits can be set as a function of the Higgs mass. First, only the

[3]The shape strongly depends on the specific signal and background expectation at a given parameter point.

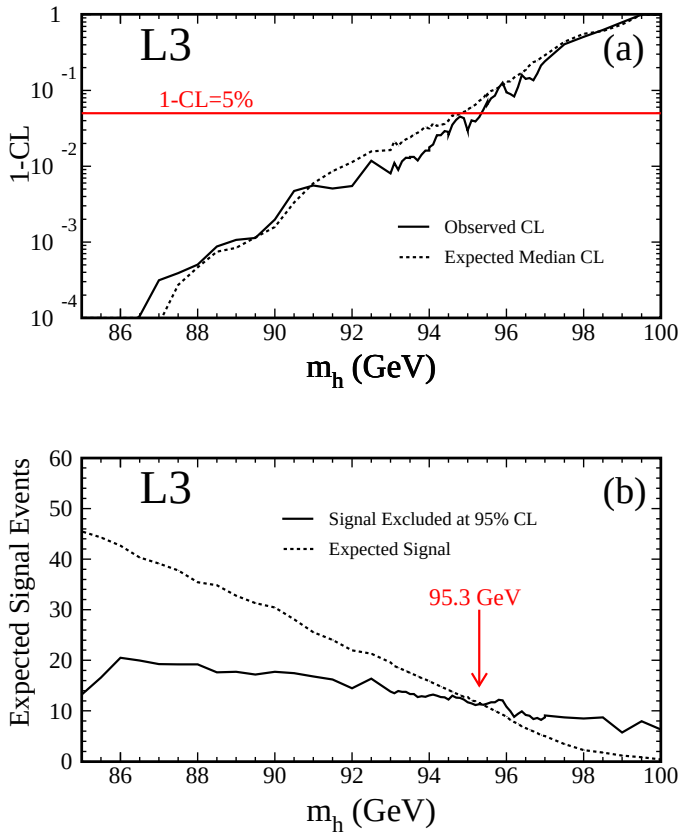

Figure 8.3: *a) The observed and the expected median confidence levels as a function of the Higgs mass for all channels combined and b) the number of expected and excluded signal events. Both plots include results from the 189 GeV data as well as from lower centre-of-mass energies. The lower limit on the Higgs mass is set at* $m_h > 95.3$ GeV *at the 95% CL.*

$hZ \to b\bar{b}\ell^+\ell^-$ ($\ell = e, \mu, \tau$) and $hZ \to \tau^+\tau^- q\bar{q}$ [4] are combined using the data taken at $\sqrt{s} = 183 - 189$ GeV. The distributions used are the mass dependent final discriminants defined in section 5.1.5. For the $hZ \to \tau^+\tau^- q\bar{q}$ channel, the reconstructed Higgs mass, m_{rec}, is used. Higgs masses between 50 and 100 GeV were considered[5]. The confidence level as a function of the Higgs mass is shown in Figure 8.2. The combination does not reveal deviations from the background expectation. Higgs masses below 87.5 GeV can be excluded at 95% CL. The probability to observe a higher mass limit in the absence of a signal is 36%. The median expected mass limit is 86.3 GeV.
The combination of the results with the other two search channels $hZ \to b\bar{b}\nu\bar{\nu}$ and $hZ \to b\bar{b}q\bar{q}$ [6] increases significantly the sensitivity towards higher Higgs masses. In the

[4]The contributions from Higgs decays into c-quarks and gluons and from the ZZ fusion diagram are also used.

[5]Higgs masses below 50 GeV are well excluded by previous analyses (see section 2.6.3).

[6]Contributions from Higgs decays into c-quarks and gluons and from the WW fusion diagram are also considered.

calculation of the confidence level, only bins with a signal-over-background ratio of at least 0.05 are considered[7]. The confidence level as a function of the Higgs mass is shown in Figure 8.3. No deviation from the SM background expectation is observed. The median expected CL crosses the 95% line at $m_h = 94.8$ GeV. A lower mass limit of

$$m_h > 95.3 \text{ GeV} \tag{8.6}$$

is set at the 95% confidence level. The probability to obtain a higher mass limit in the absence of a signal is 37%.

8.3 Mass Limits in the MSSM

Within the MSSM the neutral Higgs bosons h and A can be produced at LEP energies via the Higgs-strahlung ($e^+e^- \to hZ$) and the associated pair production ($e^+e^- \to hA$) processes. The relative production and decay rates vary with the parameter choice. Following the suggestion in Reference [12], the data are interpreted for the minimal and maximal scalar top mixing scenarios.
At high $\tan\beta$, the hA mode is dominant. Figure 8.4 shows the observed and the expected confidence level as a function of the Higgs mass m_h at $\tan\beta = 50$ for the $hA \to b\bar{b}\tau^+\tau^-$ ($hA \to \tau^+\tau^- b\bar{b}$) channels only. The probability to observe a higher confidence level in the absence of a signal is also shown. There are several candidates observed with different masses leading to an overall shift of the observed confidence level with respect to the expected one. The difference between the observed mass limit ($m_h = 45$ GeV) and the expected ($m_h = 59$ GeV) is large and results from the overall low signal expectation which is also reflected in the flat rise of the median confidence level. The probabilities for masses below 60 GeV are, however, reasonable. There are two interesting regions where the observed candidates are not very consistent with the background expectation as can be seen from the probability in Figure 8.4. The final discriminants corresponding to these regions ($m_h = 65$ GeV and $m_h = 85$ GeV) are shown in Figure 8.5. If one integrates the distributions from right to left stopping at the point where the signal to background ratio drops below one, the following numbers are obtained: for $m_h = 65$ GeV, there are 5 events observed with a background expectation of 1.6 ± 0.1, and for $m_h = 85$ GeV, there are 2 events observed with a background expectation of 0.15 ± 0.01. Unfortunately, the sensitivity of the analysis at these masses is not sufficient to draw any solid conclusion from these channels alone. A clearer picture can be obtained if one combines this analysis with the $hA \to b\bar{b}b\bar{b}$ channel, the $hZ \to AAf\bar{f}$ and the SM Higgs channels in a scan over the entire parameter space. This is shown for minimal and maximal scalar top mixing in Figure 8.6. The existence of a signal can not be established and a large fraction of the parameter space is excluded. For $\tan\beta$ greater than one, lower mass limits of

$$\begin{aligned} m_h &> 77.1 \text{ GeV} \\ m_A &> 77.1 \text{ GeV} \end{aligned} \tag{8.7}$$

[7] This cut was obtained from an analysis which optimised the average confidence level in the presence of systematic errors, carried out by Aaron Dominguez [97].

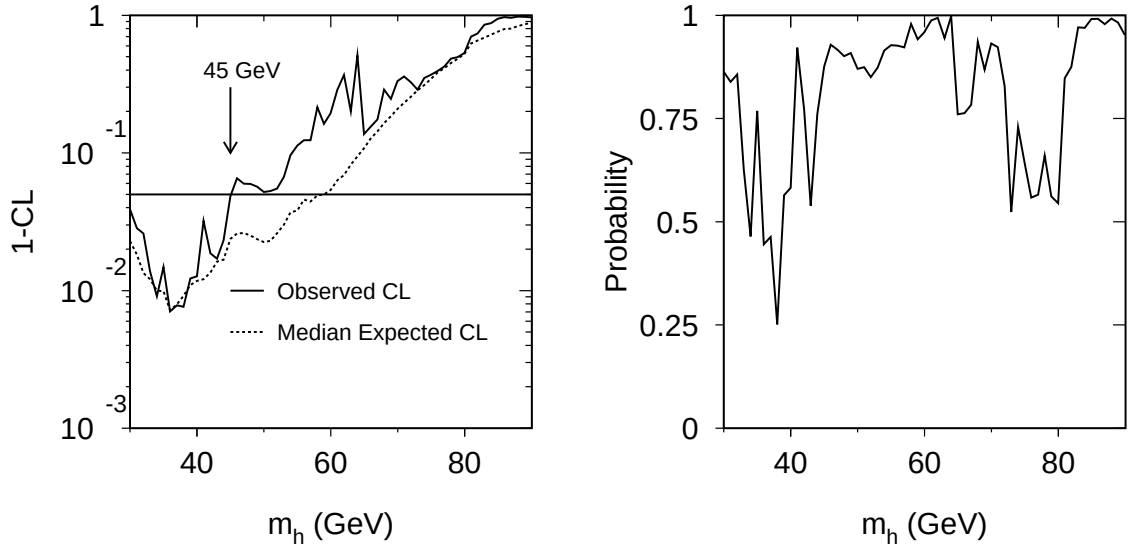

Figure 8.4: *Left: exclusion confidence level at* $\tan\beta = 50$ *for the* $\mathrm{hA} \to \mathrm{b\bar{b}}\tau^+\tau^-$ *(*$\mathrm{hA} \to \tau^+\tau^-\mathrm{b\bar{b}}$ *) channels only. Right: probability to observe a higher confidence level in the absence of a signal.*

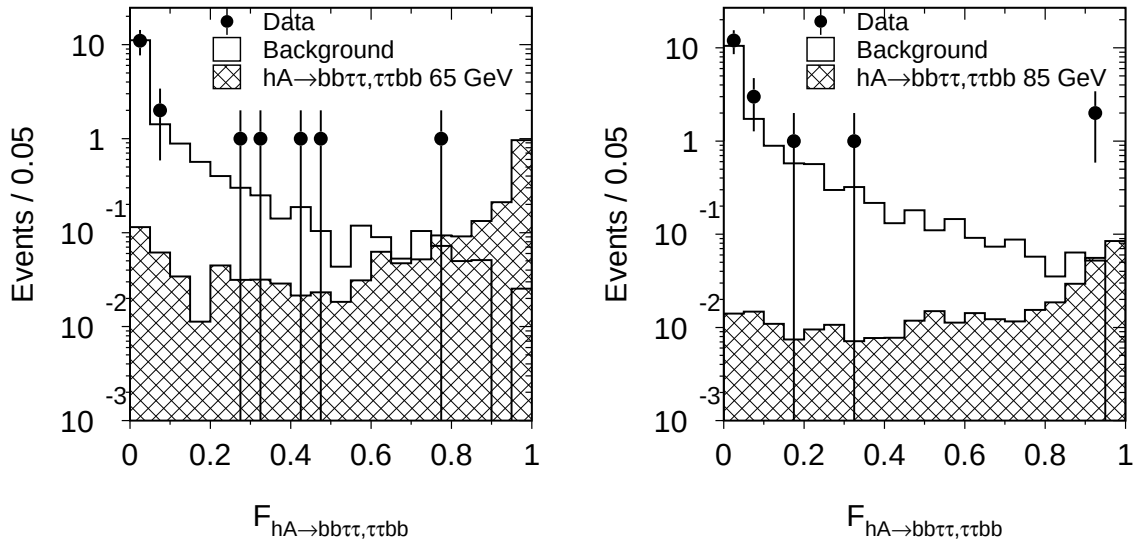

Figure 8.5: *Final discriminants for the* $\mathrm{hA} \to \mathrm{b\bar{b}}\tau^+\tau^-$ *(*$\mathrm{hA} \to \tau^+\tau^-\mathrm{b\bar{b}}$ *) channel at* $\tan\beta = 50$ *for* $\mathrm{m_h} = 65$ GeV *and* $\mathrm{m_h} = 85$ GeV.

are obtained at the 95% CL. The expected median mass limits are $\mathrm{m_h} > 80.0$ GeV $\mathrm{m_A} > 80.0$ GeV. The probability to observe a higher mass limit than the ones obtained is 80 % reflecting some fluctuation in the data with respect to the background expec-

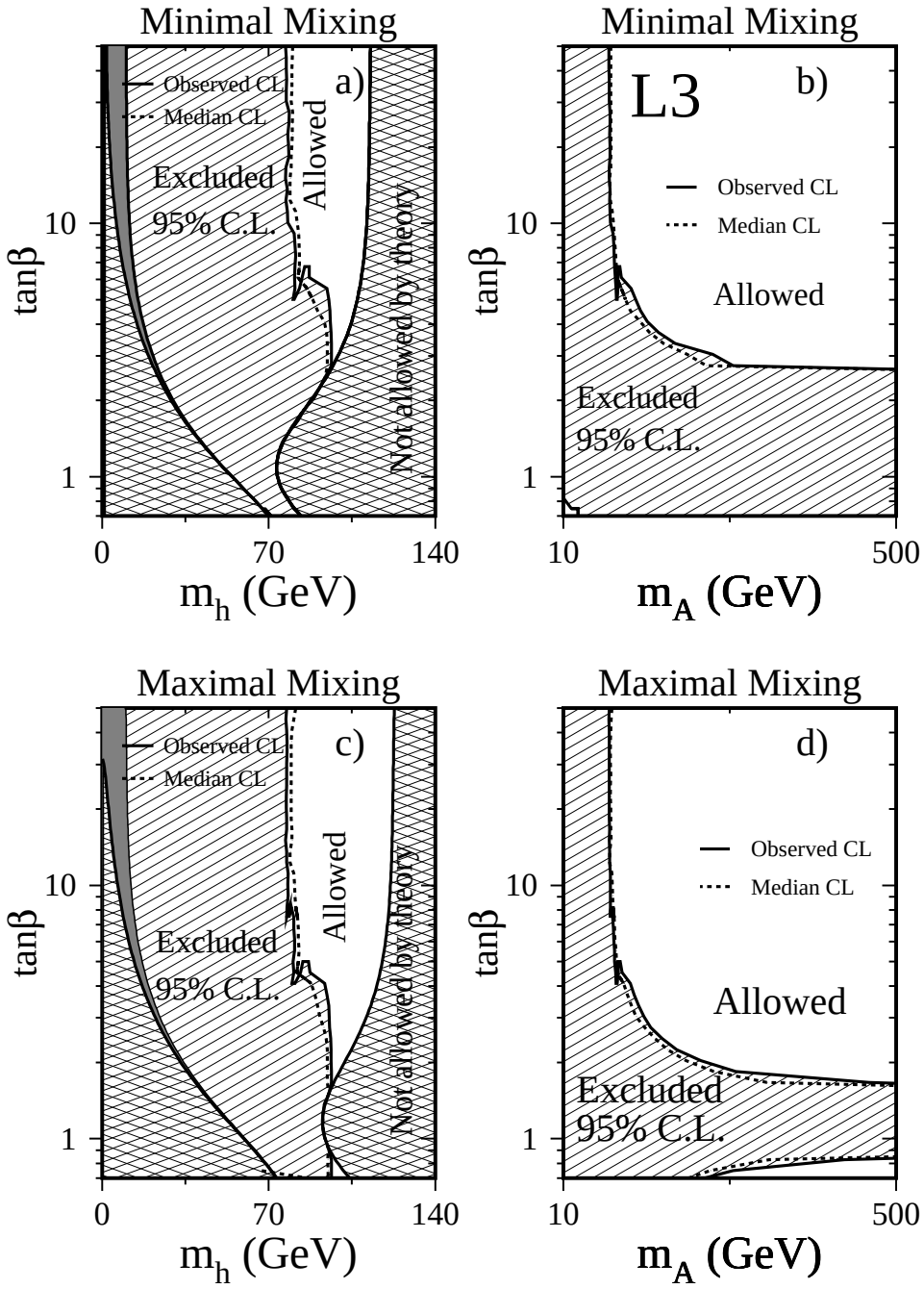

Figure 8.6: *Exclusion plots of the Higgs mass versus* $\tan\beta$ *at the 95% CL. In all plots the area shaded by diagonal lines is the 95% exclusion, while the cross hatched region is theoretically disallowed. The grey area in plots a) and c) corresponds to* $m_A < 10$ GeV *and has been previously excluded at LEP [24]. Plot a) is the 95% CL exclusion of* m_h *versus* $\tan\beta$ *in the minimal mixing scenario, b) is the 95% exclusion of* m_A *versus* $\tan\beta$ *also for minimal mixing. Plots c) and d) are the same for the maximal mixing scenario.*

tation. The region round 85 GeV remains very interesting. The probability to observe a higher confidence level is larger than 95 % indicating that the observation is not very consistent with the background only hypothesis. Unfortunately, this region is beyond our current discovery potential. The data taken in 1999 at centre-of-mass energies between $\sqrt{s} = 192$ and 202 GeV will, however, be sensitive to this region.
In the minimal scalar top mixing scenario the range $0.7 \leq \tan\beta \leq 2.6$ is excluded whereas for maximal mixing, the range $0.8 \leq \tan\beta \leq 1.5$ can be excluded at the 95% confidence level. These exclusion ranges strongly depend on the top mass and are valid for $m_{top} = 175$ GeV. For a lower top mass they would become larger whereas for a higher top mass, the ranges become smaller. Recently, there were new two-loop calculations [98] reported which favour larger values of the maximum allowed m_h. This would also reduce the excluded band of $\tan\beta$.

8.4 Mass Limits for Charged Higgs Bosons

For the charged Higgs bosons, the decays $H^{\pm} \to \tau\nu$ and $H^{\pm} \to cs$ were considered. Their relative ratio is model dependent. Three decay channels were considered: $H^+H^- \to \tau^+\nu_\tau\tau^-\bar{\nu}_\tau$, $H^+H^- \to c\bar{s}\tau^-\bar{\nu}_\tau$ and $H^+H^- \to c\bar{s}c\bar{s}$. The sum of the branching ratios, $Br(H^{\pm} \to \tau\nu)$ and $Br(H^{\pm} \to cs)$, is assumed to be one. Therefore, the individual cross sections are:

$$\begin{aligned} \sigma_{\tau\nu\tau\nu} &= \left[\mathrm{Br}(H^{\pm} \to \tau\nu)\right]^2 \sigma_{H^+H^-} \\ \sigma_{cs\tau\nu} &= 2 * \left[\mathrm{Br}(H^{\pm} \to \tau\nu)\right]\left[1 - \mathrm{Br}(H^{\pm} \to \tau\nu)\right]\sigma_{H^+H^-} \qquad (8.8) \\ \sigma_{cscs} &= \left[1 - \mathrm{Br}(H^{\pm} \to \tau\nu)\right]^2 \sigma_{H^+H^-}. \qquad (8.9) \end{aligned}$$

For the $H^+H^- \to c\bar{s}\tau^-\bar{\nu}_\tau$ channel, the relative cross section becomes maximal at $Br(H^{\pm} \to \tau\nu) = 0.5$. The confidence level at this branching ratio for the $H^+H^- \to c\bar{s}\tau^-\bar{\nu}_\tau$ channel only is shown in Figure 8.7 combining the data from 130 to 189 GeV. Mass limits can be set as a function of the branching ratio $Br(H^{\pm} \to \tau\nu)$. This is shown for the three channels and their combination in Figure 8.8.

A small hole in the exclusion is observed due to candidates in the $H^+H^- \to c\bar{s}c\bar{s}$ channel around 67 GeV (see Figure 7.5). For $Br(H^{\pm} \to \tau\nu) = 0$, the confidence level has a minimum at $m_{H^{\pm}} = 67.3$ GeV, where it drops to 88%. The probability to obtain a higher confidence level in the absence of a signal at this point is 83% (meaning that in 17% of the cases one could even have a lower confidence level). This probability indicates that the candidates are consistent with a statistical fluctuation of the background. No conclusion on the existence of a signal can be drawn.
The branching ratio independent mass limit is

$$m_{H^{\pm}} > 65.5 \text{ GeV} \qquad (8.10)$$

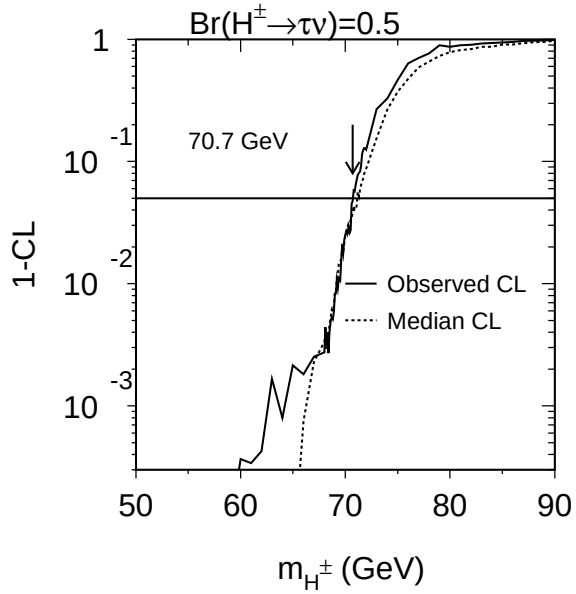

Figure 8.7: *The confidence level CL as a function of the Higgs mass in the* $\mathrm{H^+H^-} \to \mathrm{c\bar{s}\tau^-\bar{\nu}_\tau}$ *channel at* $\mathrm{Br(H^\pm \to \tau\nu)} = 0.5$ *using data taken at centre-of-mass energies between 130 and 189 GeV . The median expected confidence level is also shown.*

at the 95% CL. Charged Higgs bosons of type I, which were predicted to decay in 33% of the cases into $\tau\nu$ (see section 2.5.3) are excluded for masses below 71.9 GeV. For $\tan\beta > 0.8$, charged Higgs bosons of type II with masses below 71.5 GeV are excluded at 95% CL.

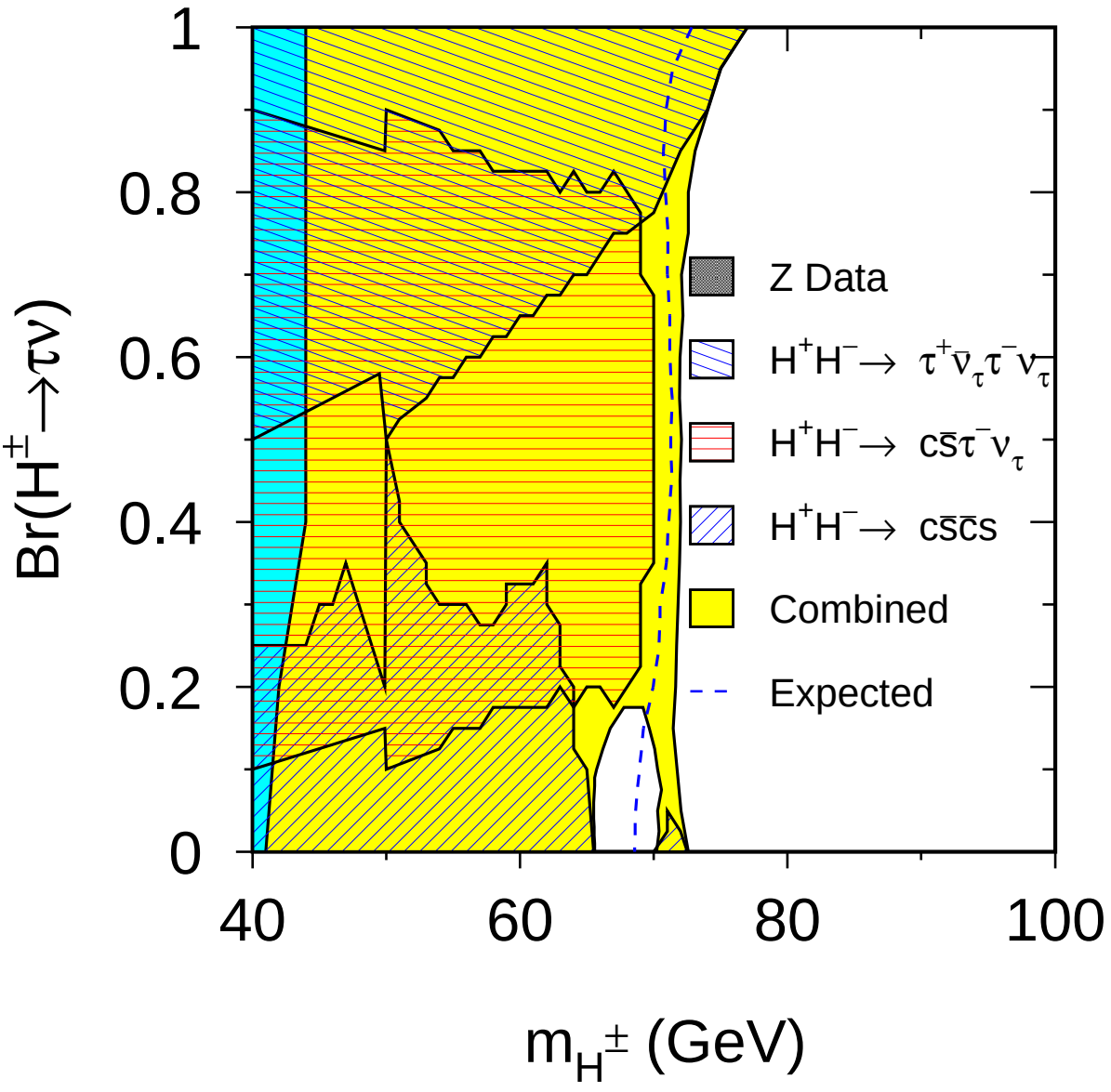

Figure 8.8: *Excluded regions for the charged Higgs boson at 95% CL in the plane of the branching fraction* $\mathrm{Br}(\mathrm{H}^{\pm} \to \tau\nu)$ *versus mass using data taken at centre-of-mass energies between 130 and 189 GeV. For masses below 50 GeV, the* $\sqrt{\mathrm{s}} = 189$ *GeV data were not used. The region excluded by L3 using Z peak data is also shown.*

Chapter 9

Observation of Resonant ZZ Production

Pair produced Z bosons are the most signal-like background source in the SM Higgs search. The cross section of this process has been measured at centre-of-mass energies of 183 and 189 GeV. The procedure is presented along with the results for $\sqrt{s} = 189$ GeV in this chapter. The analysis and the results for $\sqrt{s} = 183$ GeV can be found in appendix D. For the cross section measurement, it is assumed that the Higgs production cross section is zero.

9.1 Signal Definition

The process $e^+e^- \to ZZ$ results in a four fermion final state. There are other neutral and charged current reactions resulting to the same final state. The signal definition needs therefore some explanation.
The ZZ signal is defined using the four fermion event generator EXCALIBUR which takes all possible interference diagrams between initial and final state fermions into account. Phase space cuts are applied to define the interesting region where both Z bosons are produced on-shell. The invariant masses of the fermion pairs with the same flavour are required to lie between 70 and 105 GeV. In final states with four fermions of the same flavour, at least one of the possible fermion combinations must fulfil this requirement. In final states with electrons, events are not considered as signal if $|\cos\theta_e|$ is larger than 0.95. For the $ZZ \to q\bar{q}\ell^+\ell^-$ channel this is shown in Figure 9.1. In the case in which fermion pairs can originate from a charged-current process ($u\bar{u}d\bar{d}$, $c\bar{c}s\bar{s}$ and $\nu_\ell\bar{\nu}_\ell\ell^+\ell^-$, with $\ell = e, \mu, \tau$) the masses of the fermion pairs which could come from W decays are required to be either below 75 GeV or above 85 GeV. With these generator cuts a total cross section of 0.662 pb for $\sqrt{s} = 189$ GeV is predicted.

9.2 The $ZZ \to q\bar{q}\ell^+\ell^-$ Channel

The selections performed are similar to those in the SM Higgs analyses, but as the mass of the Z boson is well known, this information is already exploited in the selection leading

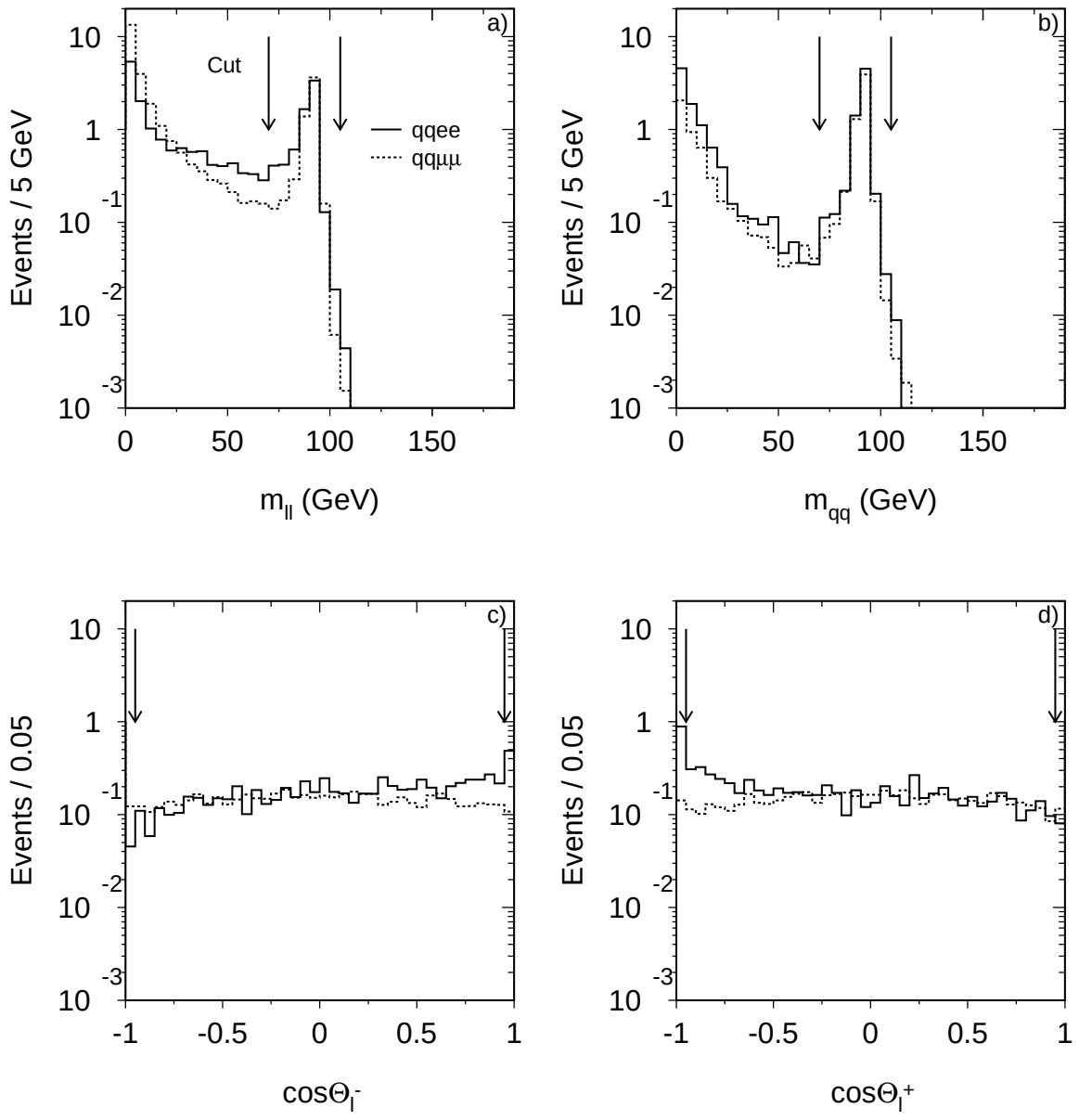

Figure 9.1: *Signal definition for the* $\mathrm{ZZ} \to \mathrm{q\bar{q}}\ell^+\ell^-$ *channel at generator level: a) invariant masses of the lepton-lepton system, b) invariant mass of the quark-quark system, c)* $\cos\theta$ *distribution for the negative lepton and d)* $\cos\theta$ *for the positive lepton. The variables are shown after all generator cuts have been applied except the cut on the quantity which is shown.*

to tighter cuts on opening angles and invariant masses, which in return allows to drop other cuts. As in the SM Higgs analysis, dedicated selections for the $\mathrm{q\bar{q}e^+e^-}$, $\mathrm{q\bar{q}}\mu^+\mu^-$ and $\mathrm{q\bar{q}}\tau^+\tau^-$ have been performed. For the latter, again two selections have been applied: a particle- and a jet-based selection. Events are accepted for the $\mathrm{ZZ} \to \mathrm{q\bar{q}}\ell^+\ell^-$ channel

if they pass either of the four selections.
The lepton identification is unchanged with respect to the SM Higgs analysis and the kinematic cuts are shown in Table 9.1. The tighter set of cuts on the opening angles

	Selection of			
	$q\bar{q}e^+e^-$	$q\bar{q}\mu^+\mu^-$	$q\bar{q}\tau^+\tau^-$	
			Particle Based	Jet Based
N_{tracks}	≥ 5	≥ 5	≥ 5	≥ 5
$N_{Cluster}$	≥ 15	≥ 15	≥ 15	≥ 15
$E_{vis}/\sqrt{s}$	≥ 0.8	≥ 0.4	≥ 0.4	$\geq 0.6, \leq 0.9$
$\ln Y_{34}$	$\geq -6.$	≥ -6.5	$\geq -6.$	$\geq -6.$
$\alpha_{\ell\ell}$ (°), α_{qq} (°)	≥ 130	≥ 130	≥ 130	≥ 130
$m_{\ell\ell}$ (GeV)	$\geq 70, \leq 120$	$\geq 70, \leq 120$	$\geq 70, \leq 120$	$\geq 70, \leq 120$
m_{qq} (GeV)	$\geq 70, \leq 120$	$\geq 70, \leq 120$	$\geq 70, \leq 120$	$\geq 70, \leq 120$
p_T^{miss} (GeV)	–	–	≤ 40	≤ 40
E_γ (GeV)	–	–	≤ 30	≤ 30
E_e (GeV)	–	–	–	≤ 40
E_μ (GeV)	–	–	–	≤ 40

Table 9.1: *Cuts applied in the* $ZZ \to q\bar{q}\ell^+\ell^-$ *selections at* $\sqrt{s} = 189$ GeV.

and the fact that ZZ is now our signal and not background, as in the previous chapters, allowed the upper cut on the visible energy as well as on electron and muon energy in the particle-based tau selection to be removed. This introduces a much larger cross efficiency of the tau selection on the $q\bar{q}e^+e^-$ and the $q\bar{q}\mu^+\mu^-$ final states leading to an improved overall acceptance for the $ZZ \to q\bar{q}\ell^+\ell^-$ channel. The efficiency table is shown together with the number of observed candidates and the background and signal expectation in Table 9.2. There are in total 15 events selected with an expectation of 10.9 events from

Selection of process $ZZ \to$	Efficiency (%) on $ZZ \to$			Expected Signal	Expected Background	Observed Data
	$q\bar{q}e^+e^-$	$q\bar{q}\mu^+\mu^-$	$q\bar{q}\tau^+\tau^-$			
$q\bar{q}e^+e^-$	77.8	0.0	0.5	5.2	2.1	9
$q\bar{q}\mu^+\mu^-$	0.0	63.5	1.3	3.6	0.2	2
$q\bar{q}\tau^+\tau^-$	46.1	49.5	31.6	7.6	3.3	10

Table 9.2: *Cross efficiencies for the different lepton flavour selection in the* $ZZ \to q\bar{q}\ell^+\ell^-$ *channel. The expected signal and background along with the number of observed candidates are also shown.*

the signal and 5.4 from the background. The invariant mass arising from a kinematic fit, which requires energy and momentum conservation and the lepton-lepton mass to be equal to the jet-jet mass, is shown in Figure 9.2 a).

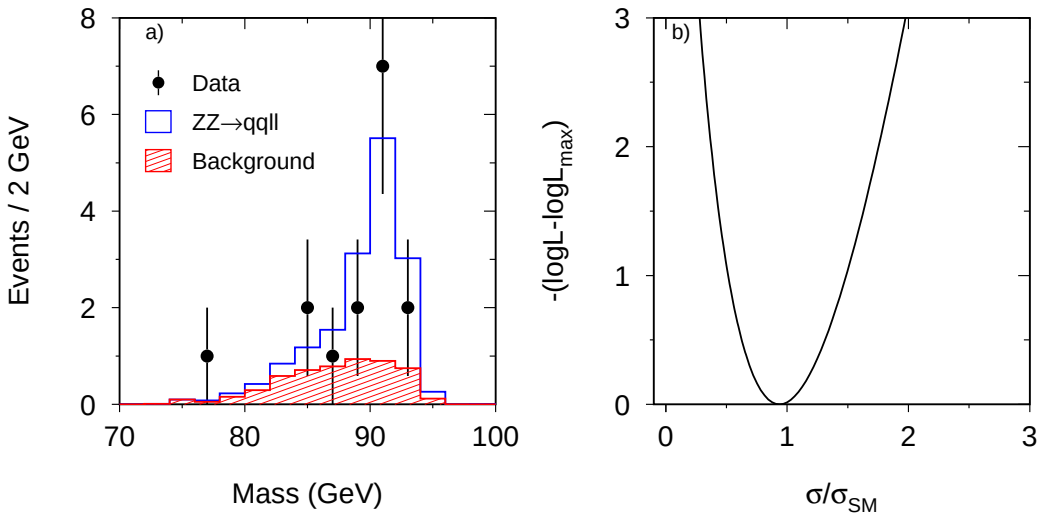

Figure 9.2: *a) Final mass distribution in the* $ZZ \to q\bar{q}\ell^+\ell^-$ *channel at* $\sqrt{s} = 189$ GeV, *b) likelihood curve obtained by fitting the spectrum in a) as a function of the ratio of the measured to the predicted cross section*

9.3 The ZZ Cross Section

The cross section for the $ZZ \to q\bar{q}\ell^+\ell^-$ channel is obtained by applying a binned maximum likelihood fit to the invariant mass distribution shown in Figure 9.2 a). The fit result is presented in Figure 9.2 b). The cross section is measured to be:

$$\sigma_{ZZ \to q\bar{q}\ell^+\ell^-} = 0.096^{+0.039}_{-0.033} \text{ pb},$$

which is in good agreement with the SM prediction of 0.102 pb. The quoted error is purely statistical.
The probability to measure this or a higher cross section as result of a background fluctuation, assuming that the ZZ process does not exist, is $3 \cdot 10^{-5}$.
Other analyses were performed in the channels $ZZ \to q\bar{q}\nu\bar{\nu}$, $\ell^+\ell^-\nu\bar{\nu}$, $\ell^+\ell^-\ell'^+\ell'^-$ and $q\bar{q}q'\bar{q}'$. A description of the analysis and the individual results can be found in References [99, 100].
The channels are combined by making an one parameter maximum likelihood fit assuming that the individual contributions scale with the generator prediction. This yields a total cross section of:

$$\sigma_{ZZ} = 0.74^{+0.15}_{-0.14} \text{ pb}.$$

In the calculation of the cross section, the effect of the cross efficiencies between the channels was found to be negligible.

9.4 Systematic Errors

Systematic errors for the individual channels were studied. They are divided into those which are correlated and those which are uncorrelated between the different channels. Correlated among the channels are uncertainties on the background cross section prediction, the LEP energy and the energy scale of the detector. Their effect on the measured

Systematic Source	Variation	$\delta\sigma_{ZZ}$ (pb)	$\delta\sigma_{ZZ\to b\bar{b}X}$ (pb)
Correlated sources			
Lep energy	40 MeV	< 0.01	< 0.01
WW cross section	2%	0.01	< 0.01
Four–jet rate	5%	0.01	0.01
Weν cross section	10%	0.01	< 0.01
Four–fermion cross section	5%	< 0.01	0.01
Energy scale	2%	0.01	0.01
Theory predictions	2%	0.01	< 0.01
Uncorrelated sources			
Jet resolution ($q\bar{q}q'\bar{q}'$)	2%	0.01	< 0.01
Charge multiplicity ($q\bar{q}q'\bar{q}'$)	1%	< 0.01	< 0.01
B–tag ($q\bar{q}q'\bar{q}'$)		0.01	0.01
Bhabha background ($\ell^+\ell^-\nu\bar{\nu}$)		0.01	–
Monte Carlo statistics		0.02	0.01
Lepton identification		0.01	0.01
Total		0.04	0.02

Table 9.3: *Systematic uncertainties on σ_{ZZ} and $\sigma_{ZZ\to b\bar{b}X}$.*

cross section is determined by performing a new fit of σ_{ZZ} after varying their values within the limits as listed in Table 9.3. An error of 2% has to be attributed to the measured cross section to account for the theoretical uncertainty on the relative contribution of the different channels to the total cross section. This error was derived by comparing the EXCALIBUR prediction to the prediction obtained from the GRC4F [101] Monte Carlo generator.
Uncorrelated errors arise from limited Monte Carlo statistics and channel related analysis techniques or selection criteria such as lepton identification ($q\bar{q}\ell^+\ell^-$, $\ell^+\ell^-\nu_\ell\bar{\nu}_\ell$ and $\ell^+\ell^-\ell'^+\ell'^-$), jet resolution, charged track multiplicity and b-tagging[1] ($q\bar{q}q'\bar{q}'$). In the $ZZ \to \ell^+\ell^-\nu\bar{\nu}$ channel an error due to the insufficient Bhabha background description had to be assigned. The influence of the individual error sources on the measured cross section is presented in Table 9.3. The measured cross section is then:

$$\sigma_{ZZ} = 0.74^{+0.15}_{-0.14}\ (\text{stat.})\ \pm 0.04\ (\text{syst.})\ \text{pb}.$$

[1]B-tagging is used in the neural network based four-jet analysis to discriminate against the overwhelming WW background.

For the ZZ $\rightarrow q\bar{q}\ell^+\ell^-$ channel alone a systematic error of ± 0.003 pb is determined. The measured cross section is displayed together with its predicted evolution as a function of $\sqrt{s}$ in Figure 9.3. The cross section ZZ $\rightarrow b\bar{b}X$ is also shown. For the latter the contribution of the light quarks (u,d,s,c) is fixed to their SM predictions and only the b-content in the ZZ sample for the three hadronic channels ZZ $\rightarrow q\bar{q}\ell^+\ell^-$, ZZ $\rightarrow q\bar{q}\nu\bar{\nu}$ and ZZ $\rightarrow q\bar{q}q'\bar{q}'$ is fitted. No enhancement on b-quark production is observed, which is consistent with the analysis presented in chapter 5.

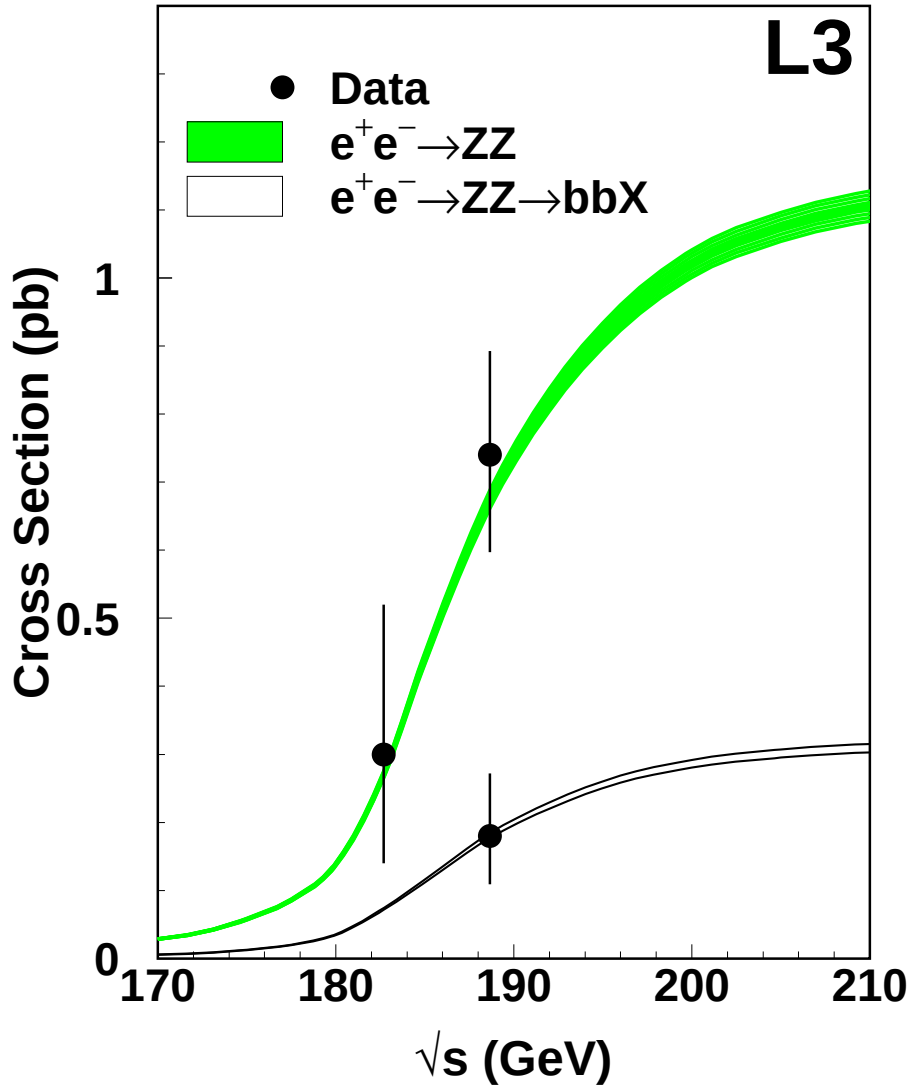

Figure 9.3: *ZZ cross section measured at 183 and 189 GeV. Signal definition cuts implemented with the EXCALIBUR Monte Carlo are applied and a 2% uncertainty is associated to the prediction. The measured* ZZ $\rightarrow b\bar{b}X$ *is also shown.*

Chapter 10

Conclusions

10.1 Higgs Searches

Searches for Higgs bosons predicted in one and two doublet models have been carried out in experimentally related channels. No evidence for Higgs boson production was found. The negative outcome of this search was translated into mass limits.
The SM Higgs boson was searched for in the $hZ \to b\bar{b}e^+e^-$, $hZ \to b\bar{b}\mu^+\mu^-$, $hZ \to b\bar{b}\tau^+\tau^-$ and the $hZ \to \tau^+\tau^- q\bar{q}$ channels with data taken at centre-of-mass energies between 183 and 189 GeV. No indication of such a boson was found and a lower mass limit of

$$m_h > 87.5 \ \text{GeV}$$

is set at the 95% confidence level. Combining the results of this thesis with the $hZ \to b\bar{b}q\bar{q}$ and the $hZ \to b\bar{b}\nu\bar{\nu}$ analyses investigated by other members of the L3 Higgs working group leads to a lower limit of

$$m_h > 95.3 \ \text{GeV}.$$

This number is compared to the results of the other LEP collaborations in Table 10.1. The results of the four LEP collaborations were combined and a lower limit of

$$m_h > 95.2 \ \text{GeV}$$

is derived [102]. No improvement with respect to L3 alone is found because of an overall excess of candidates observed by the ALEPH and OPAL experiments. These candidates are consistent with a statistical fluctuation of the background and can not be interpreted as a signal.
For the search of neutral Higgs bosons predicted within the MSSM, the SM Higgs analyses were complemented with a dedicated selection of the process $hA \to b\bar{b}\tau^+\tau^-$ ($hA \to \tau^+\tau^- b\bar{b}$). In combination with the $hA \to b\bar{b}b\bar{b}$ channel, exclusion limits were set in dependence of m_A and $\tan\beta$. The lower mass limits for $\tan\beta > 1$ are:

$$\begin{aligned} m_h &> 77.1 \ \text{GeV} \\ m_A &> 77.1 \ \text{GeV}. \end{aligned}$$

The results of the other LEP experiments are shown in Table 10.1. Charged Higgs bosons were searched for in the $H^+H^- \to c\bar{s}\tau^-\bar{\nu}_\tau$ channel. Mass limits are set as a function of the branching ratio $Br(H^\pm \to \tau\nu)$. In combination with the $H^+H^- \to \tau^+\nu_\tau\tau^-\bar{\nu}_\tau$ and the $H^+H^- \to c\bar{s}\bar{c}s$ channels a lower mass limit of

$$m_{H^\pm} > 65.5 \text{ GeV}$$

is derived. The results of the other LEP collaborations are shown in Table 10.1.

	SM Higgs	MSSM Higgs		Charged Higgs
	m_h (GeV)	m_h (GeV)	m_A (GeV)	$m_{H^\pm}$ (GeV)
ALEPH	92.9 (95.9)	82.5 (83.0)	83.1 (83.0)	65.5 (69.5)
DELPHI	94.1 (94.6)	82.1 (81.1)	83.2 (82.2)	66.9 (66.5)
L3	95.3 (94.8)	77.1 (80.0)	77.1 (80.0)	65.5 (68.5)
OPAL	91.0 (94.9)	74.8 (76.4)	76.5 (78.2)	68.7 (69.0)

Table 10.1: *Lower mass limits for Higgs bosons obtained by the LEP experiments using the data up to a centre-of-mass energy of 189 GeV [103]. The numbers in parentheses denote the expected limits.*

10.2 ZZ Production

The ZZ cross section was measured for the first time. This measurement is an unique opportunity to cross-check the Higgs analyses. The search for the Higgs bosons relies on the Higgs-fermion couplings. Assuming that these couplings are not correctly predicted by the theory, we would not necessarily see the Higgs bosons in the dedicated analyses. If a Higgs boson is, however, present in the data, it should lead to an enhancement of the cross section in a quark flavour blind measurement of the ZZ cross section. In this thesis, the cross sections for $ZZ \to q\bar{q}\ell^+\ell^-$ ($\ell = e, \mu, \tau$) at $\sqrt{s} = 183$ GeV and $\sqrt{s} = 189$ GeV were measured to be:

$$\sigma_{ZZ\to q\bar{q}\ell^+\ell^-} = 0.054^{+0.134}_{-0.034} \text{ (stat.)} \pm 0.002 \text{ (syst.) pb at 183 GeV},$$

$$\sigma_{ZZ\to q\bar{q}\ell^+\ell^-} = 0.096^{+0.039}_{-0.033} \text{ (stat.)} \pm 0.003 \text{ (syst.) pb at 189 GeV},$$

which is in agreement with the SM expectations of 0.043 pb at 183 GeV and 0.102 pb at 189 GeV. Combining these results with the channels $ZZ \to q\bar{q}\nu\bar{\nu}$, $\ell^+\ell^-\nu\bar{\nu}$, $\ell^+\ell^-\ell'^+\ell'^-$ and $q\bar{q}q'\bar{q}'$, analysed by other members of the L3 ZZ working group, leads to cross sections of:

$$\sigma_{ZZ} = 0.30^{+0.22}_{-0.16} \text{ (stat.)} \, ^{+0.07}_{-0.03} \text{ (syst.) pb at 183 GeV},$$

$$\sigma_{ZZ} = 0.74^{+0.15}_{-0.14} \text{ (stat.)} \, ^{+0.04}_{-0.04} \text{ (syst.) pb at 189 GeV}.$$

The Standard Model predicts values of 0.25 pb and 0.662 pb in agreement with the measurement. For the combination of the results with the other experiments, the efficiencies

are recalculated for the NC02 approximation for double-resonant Z pair production. The cross sections measured by the four LEP experiments and their combination is shown in Figures 10.1 and 10.2. The evolution of the cross section as a function of the centre-of-mass energy is presented in Figure 10.3. The LEP measurement agrees with the Standard Model prediction.

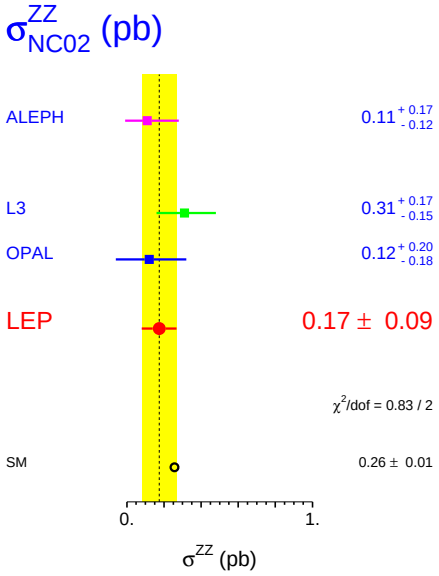

Figure 10.1: *Cross section measured by the LEP experiments at* $\sqrt{s}$ = 183 GeV *and their combined value. The SM prediction is also plotted.*

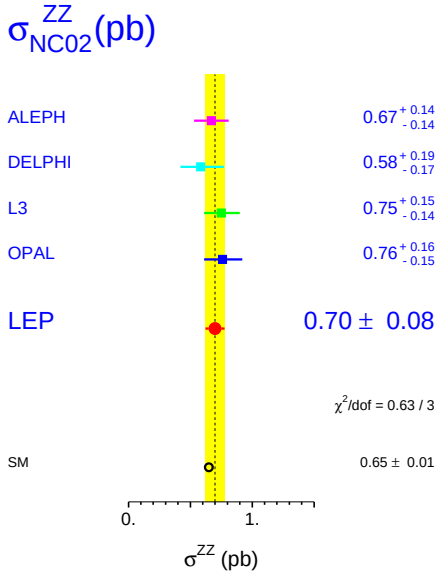

Figure 10.2: *Cross section measured by the LEP experiments at* $\sqrt{s}$ = 189 GeV *and their combined value. The SM prediction is also plotted.*

10.3 Perspectives on Further Searches

Perspectives at LEP:
Although, only mass limits could be reported in this thesis, LEP remains an exciting place also for the last two years of running. In particular, a discovery of the SM Higgs boson and the neutral Higgs bosons of the MSSM is still possible. By the time at which this thesis was written, integrated luminosities of 29.3 pb^{-1} at 192 GeV, 81.4 pb^{-1} at 196 GeV, 73.4 at 200 GeV centre-of-mass energy have been collected by L3. Currently, data are taken at $\sqrt{s} = 202$ GeV. In the year 2000 LEP will most likely run at 205 GeV. Depending on the final energy and the amount of luminosity collected, the discovery potential of LEP lies between $m_h \approx 105$ and 107 GeV. If the Higgs is not in the reach of LEP, it can be excluded for masses below 110 GeV.
In the MSSM the sensitivity of LEP is almost independent of the final energy. Since the predicted cross section is low, a large amount of integrated luminosity is very important.

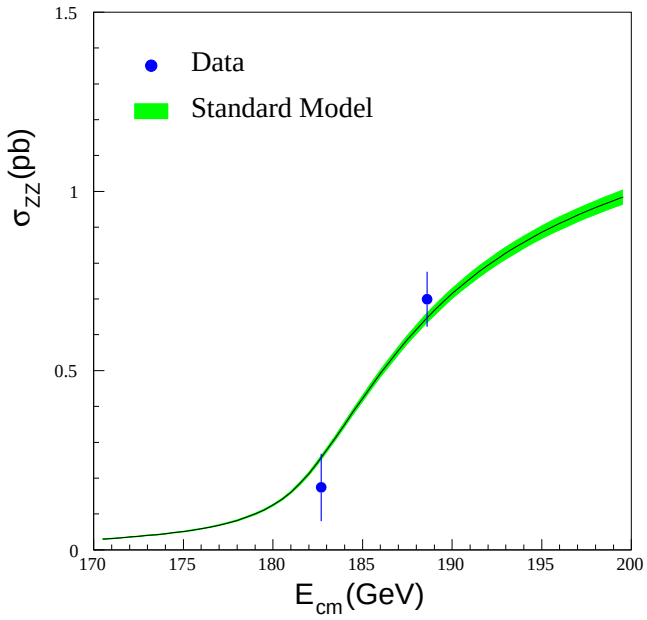

Figure 10.3: *Evolution of the ZZ cross section with the centre-of-mass energy. The curve of the SM prediction includes a 2% theoretical error.*

With an optimistic estimate, that 400 pb^{-1} per experiment are going to be collected in the years 1999–2000, LEP will be sensitive to h and A masses of about 92 GeV [104]. More interesting is, however, that a large fraction of the parameter space (low $\tan\beta$) can be ruled out completely, setting stringent constraints on the MSSM.
A discovery of charged Higgs bosons at LEP is not very likely taking into account that the sensitivity is somewhere around the W mass. Since here the expected signal cross section is almost two orders of magnitude smaller than the WW cross section, it would be very difficult to prove the existence of a signal.

After LEP
The next machine, which can contribute to Higgs physics, is the TEVATRON at Fermilab. Run II (2 fb^{-1} per experiment) is approved and will start in mid 2000. Although single Higgs production by gluon fusion has the largest cross section, the more promising scenarios are the $q\bar{q}' \rightarrow hW$ and $q\bar{q} \rightarrow hZ$ production modes, since a large fraction of the overwhelming QCD background can be suppressed by tagging leptons from the W and Z decays. The integrated luminosity of run II will, however, not be sufficient to go significantly beyond the sensitivity of LEP. For the SM Higgs, masses up to about 110 GeV could be excluded [105]. No discovery is possible in run II. In the MSSM a large fraction of the parameter space can be excluded. However, for a discovery, 20–30 fb^{-1} per experiment will be needed. If this amount of luminosity will be delivered in an extension of run II, the SM Higgs boson with masses up to 180 GeV can be discovered at a 3 σ level. Almost the entire parameter space in the MSSM can be covered with the exception of a few pathological regions. The time needed to collect this amount of integrated luminosity will bring the TEVATRON on the same time scale with the LHC

at CERN. The LHC, most likely starting in 2005, will cover the entire SM and MSSM parameter space.
Once Higgs bosons are discovered, a Linear Collider, as proposed in Reference [106], will be the most suitable device at an intermediate time scale to study the properties of Higgs bosons. With a muon collider one could even do better. However, up to now, it is not clear whether it will be technically possible to build such a machine.

Appendix A

SM Higgs at 183 GeV

The same selections discussed in chapter 5 have been applied to the data taken at $\sqrt{s} = 183$ GeV. The selection efficiencies are shown in Table A.1. The number of observed

Selection of process	Efficiency (%) on m_h (GeV)						
	55	60	70	80	85	87	90
$hZ \to b\bar{b}e^+e^-$	75 ± 3	79 ± 3	75 ± 3	78 ± 3	78 ± 3	74 ± 3	76 ± 3
$hZ \to b\bar{b}\mu^+\mu^-$	49 ± 3	52 ± 3	52 ± 3	56 ± 3	55 ± 3	56 ± 3	57 ± 3
$hZ \to b\bar{b}\tau^+\tau^-$	29 ± 2	30 ± 2	31 ± 2	30 ± 2	27 ± 2	28 ± 2	26 ± 2
$hZ \to \tau^+\tau^-q\bar{q}$	29 ± 2	30 ± 2	32 ± 2	31 ± 2	32 ± 2	30 ± 2	30 ± 2

Table A.1: *Selection efficiencies for various Higgs masses in the Standard Model at* $\sqrt{s} = 183$ *GeV.*

candidates is compared to the background expectation after the selection in Table A.2. As an example, the final discriminant distributions are shown for $m_h = 87$ GeV in

Channel	Background	Data
$hZ \to b\bar{b}e^+e^-$	2.9 ± 0.1	4
$hZ \to b\bar{b}\mu^+\mu^-$	1.1 ± 0.1	0
$hZ \to b\bar{b}\tau^+\tau^-$	1.5 ± 0.1	1
$hZ \to \tau^+\tau^-q\bar{q}$	3.6 ± 0.4	4

Table A.2: *Number of observed candidates and background expectation in the SM Higgs analysis at 183 GeV. The relative number of events in the* $hZ \to b\bar{b}\tau^+\tau^-$ *and the* $hZ \to \tau^+\tau^-q\bar{q}$ *channel changes with the Higgs mass hypothesis and is given here for* $m_h = 87$ GeV.

Figure A.1.

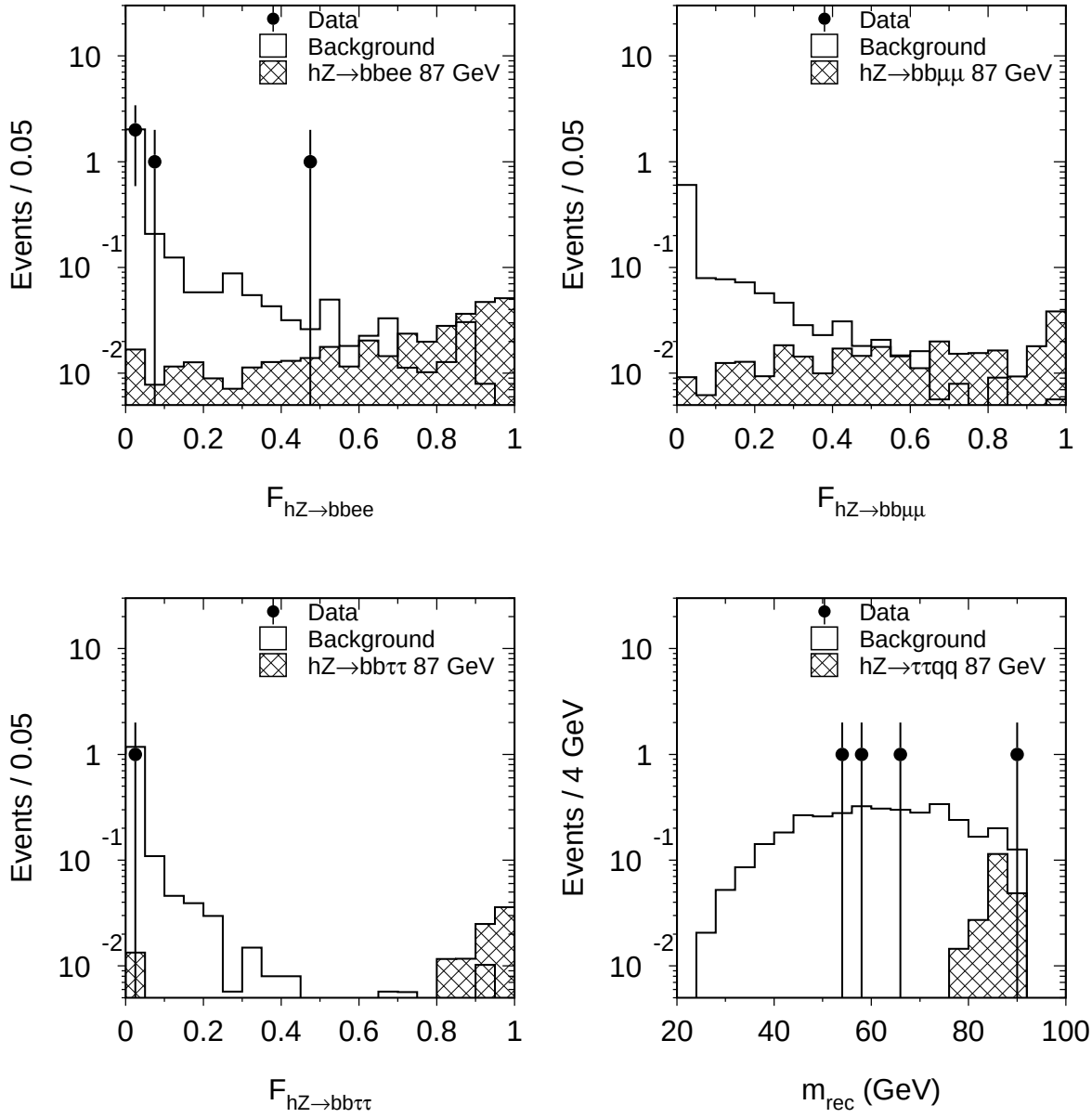

Figure A.1: *Final discriminant variables in the SM Higgs analysis at 183 GeV for* $m_h = 87$ GeV.

Appendix B

MSSM Higgs at 183 GeV

The same selection criteria as for the 189 GeV are applied to the data sample at $\sqrt{s} = 183$ GeV. The selection efficiencies for various Higgs masses are reported in Table B.1. The background expectations and the number of observed candidates are

	m_A (GeV)	50	60	70	80	70	80
	m_h (GeV)	50	60	70	80	60	70
$\epsilon_{hA\to b\bar{b}\tau^+\tau^-}$ (%)		36 ± 2	36 ± 2	36 ± 2	32 ± 2	37 ± 2	34 ± 2
$\epsilon_{hA\to\tau^+\tau^- b\bar{b}}$ (%)		34 ± 2	39 ± 2	34 ± 2	31 ± 2	38 ± 2	36 ± 2

Table B.1: *Efficiency of the* $hA \to b\bar{b}\tau^+\tau^-$ *and* $hA \to \tau^+\tau^- b\bar{b}$ *sample for various Higgs mass combinations at* $\sqrt{s} = 183$ *GeV.*

given in Table B.2. Discriminant distributions for several Higgs mass hypotheses at

Selection of	Background	Data
hA	5.1 ± 0.4	5
hZ	5.1 ± 0.5	5
hA or hZ	7.9 ± 0.8	7

Table B.2: *Number of observed candidates and background expectation in the MSSM Higgs analysis at 183 GeV. The letters hA denote the* $hA \to b\bar{b}\tau^+\tau^-$ *channel, and hZ stands for* $hZ \to b\bar{b}\tau^+\tau^-$ *and* $hZ \to \tau^+\tau^- q\bar{q}$.

$\tan\beta = 50$ are shown in Figure B.1.

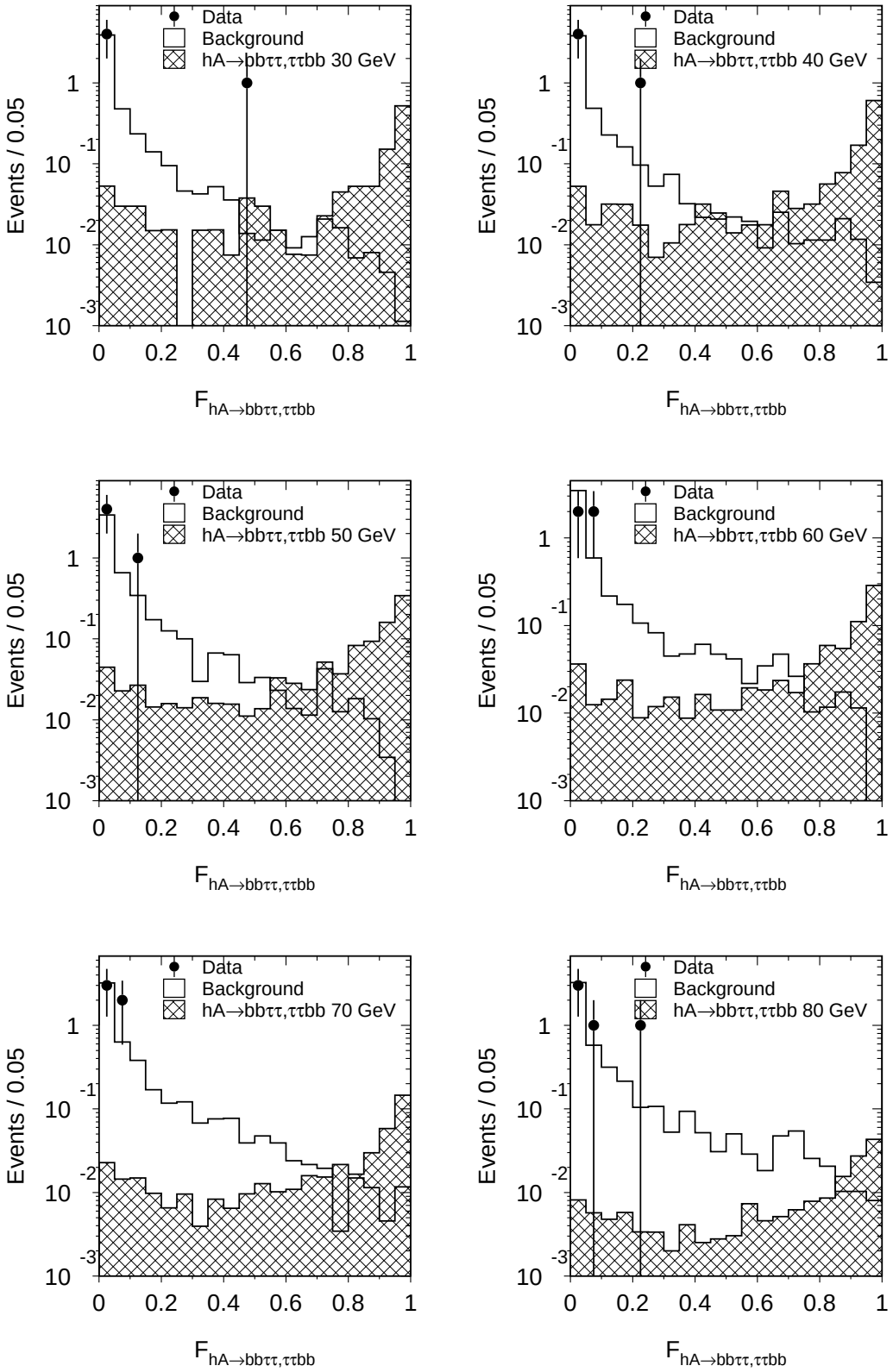

Figure B.1: *Final discriminants for the* $\mathrm{hA} \to \mathrm{b\bar{b}}\tau^+\tau^-$ *channel at* $\sqrt{\mathrm{s}} = 183$ GeV *for various Higgs masses at* $\tan\beta = 50$.

Appendix C

Charged Higgs between 130 and 183 GeV

The cuts applied at the lower centre-of-mass energies in the charged Higgs search differ slightly from those presented in chapter 7. Table C.1 shows the selection cuts for the centre-of-mass energies between 130 and 183 GeV.

	$\sqrt{s}$ (GeV)			
	130–136	161	172	183
N_{tracks}	≥ 5	≥ 5	≥ 5	≥ 5
$N_{cluster}$	≥ 10	≥ 10	≥ 10	≥ 10
$E_{vis}/\sqrt{s}$	$\geq 0.35, \leq 1$	$\geq 0.35, \leq 1$	$\geq 0.35, \leq 1$	$\geq 0.35, \leq 1$
E_{Lumi} (GeV)	≤ 10	≤ 10	≤ 10	≤ 10
E_{γ} (GeV)	≤ 10	≤ 20	≤ 40	≤ 50
$\mid \cos\theta_{miss} \mid$	≤ 0.9	≤ 0.9	≤ 0.9	≤ 0.9
p_T^{miss} (GeV)	≥ 5	≥ 3	≥ 3	≥ 3
p_T^{miss}/E_{vis}	≥ 0.1	≥ 0.1	≥ 0.1	≥ 0.1
p_Z^{miss}/E_{vis}	–	–	≤ 0.4	≤ 0.5
$\alpha_{mj} + \alpha_{\tau j}$ (°)	≥ 60	≥ 80	≥ 80	≥ 80
α_{miss}^{25} (GeV)	≤ 10	≤ 40	≤ 40	≤ 40
m_{qq}^{vis} (GeV)	≤ 90	≤ 90	≤ 90	≤ 90
$\alpha_{qq}^{r\phi}$ (°)	–	–	–	≤ 160
$\mid \cos\theta \mid$	≤ 0.8	≤ 0.8	≤ 0.8	≤ 0.9
$\mid p_{miss}^{*} \mid + E_e^{*}$ (GeV)	–	≤ 60	≤ 60	≤ 60
$\mid p_{miss}^{*} \mid + E_{\mu}^{*}$ (GeV)	–	≤ 50	≤ 50	≤ 50

Table C.1: *Selection cuts in the* $H^+H^- \rightarrow c\bar{s}\tau^-\bar{\nu}_\tau$ *channel at centre-of-mass energies between 130 and 183 GeV. The abbreviations not explained before have the following meaning:* α_{miss}^{25} *is the energy deposition in a 25 degree cone around the missing momentum vector and* $\alpha_{qq}^{r\phi}$ *is the opening angle between the two hadronic jets in the r-*ϕ *plane.*

The selection efficiencies for various Higgs masses are presented along with the number of candidates and the background expectation in Table C.2.

$\sqrt{s}$ (GeV)	$m_{H^\pm}$ (GeV)					Background	Data
	40	50	60	65	70		
130–136	41 ± 2	41 ± 2	33 ± 2	/	/	0.6 ± 0.4	1
161	32 ± 2	40 ± 2	47 ± 2	44 ± 2	41 ± 2	2.0 ± 0.2	1
172	34 ± 2	35 ± 2	46 ± 2	44 ± 2	42 ± 2	7.1 ± 0.2	9
183	30 ± 1	41 ± 2	41 ± 2	42 ± 2	42 ± 2	30.1 ± 0.9	28

Table C.2: *Selection efficiencies for various Higgs masses, the background expectation and the number of observed candidates for the* $H^+H^- \to c\bar{s}\tau^-\bar{\nu}_\tau$ *channel at centre-of-mass energies between 130 and 183 GeV.*

Distributions of important variables used in the analysis are shown in Figure C.1 for $\sqrt{s} = 183$ GeV.

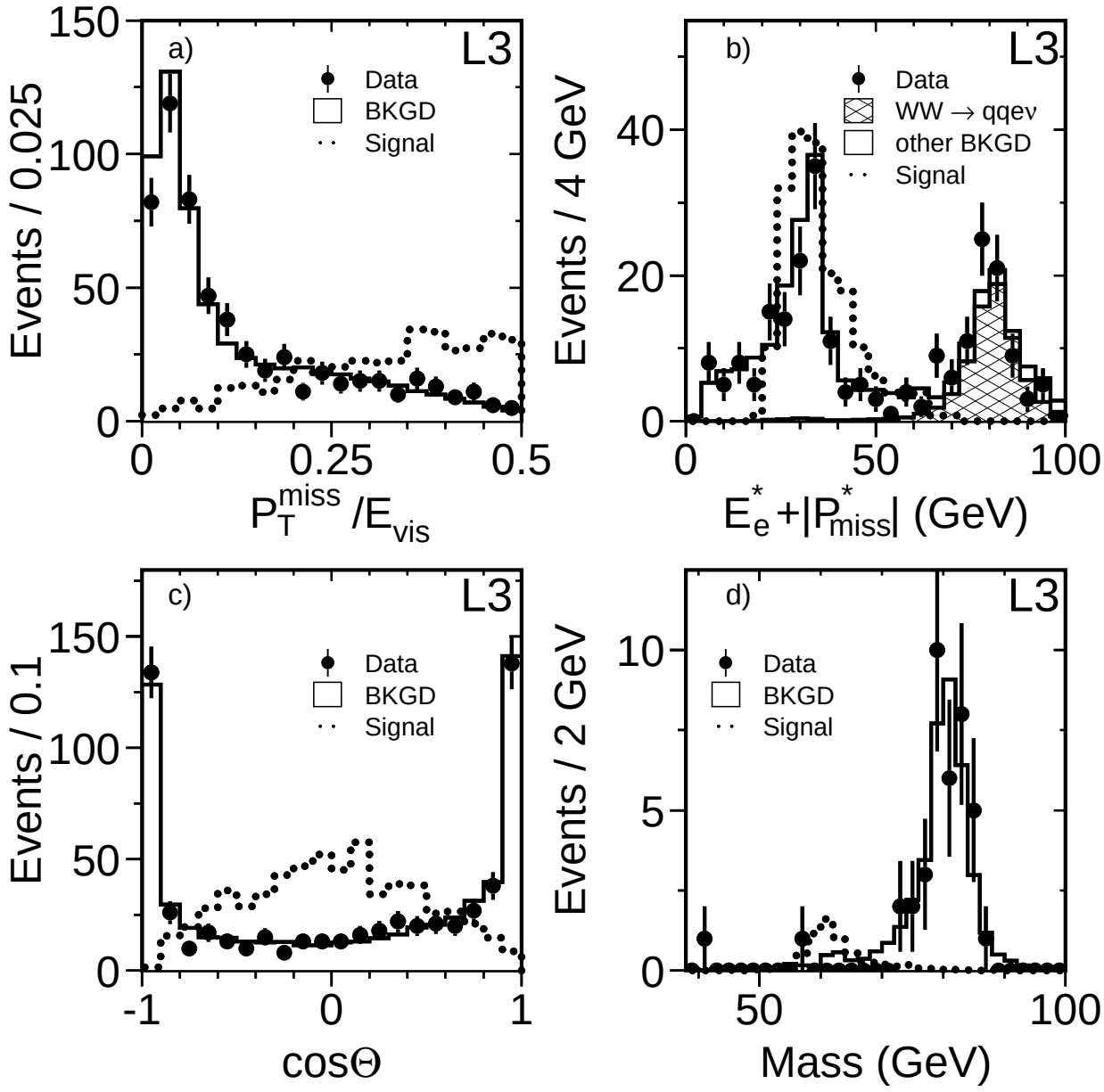

Figure C.1: *Distributions for the* $\mathrm{H^+H^-} \to \mathrm{c\bar{s}}\tau^-\bar{\nu}_\tau$ *channel after a hadronic preselection and* τ *identification: a) ratio of the missing transverse momentum and the visible energy for* $\sqrt{s} = 183$ *GeV, b) sum of the electron energy and the absolute value of the missing momentum in the rest frame of the leptonically decaying parent particle for events with an identified electron in the final state for* $\sqrt{s} = 183$ *GeV, where the background process* $\mathrm{W^+W^-} \to \mathrm{q\bar{q}e}\nu$ *is clearly separated from the signal, c) polar angle distribution of the negative parent particle for* $\sqrt{s} = 183$ *GeV and d) reconstructed mass spectrum after all cuts for* $\sqrt{s} = 130 - 183$ *GeV. The dotted lines indicate the signal for a 60 GeV charged Higgs boson at* $\mathrm{Br(H^\pm \to \tau\nu)} = 0.5$ *multiplied by a factor of 100 (a-c) and by a factor of one (d).*

Appendix D

ZZ Production at 183 GeV

The selection of the ZZ $\to$ q$\bar{\text{q}}\ell^+\ell^-$ channel at $\sqrt{\text{s}} = 183$ GeV differs slightly to the one presented in chapter 9. The selection criteria are summarised in Table D.1. The

	Selection of ZZ $\to$			
	qqee	qq$\mu\mu$	qq$\tau\tau$	
			Particle-based	Jet-based
N_{Tracks}	≥ 9	≥ 9	≥ 9	≥ 9
N_{Cluster}	≥ 15	≥ 15	≥ 15	≥ 15
$E_{\text{vis}}/\sqrt{s}$	≥ 0.8	≥ 0.7	≥ 0.4, ≤ 0.95	≥ 0.4
$m_{\text{vis}}/\sqrt{s}$	–	–	–	≤ 0.87
E_e (GeV)	≥ 20, ≤ 60	–	≤ 50	≤ 45
E_μ (GeV)	–	≥ 20 GeV	≤ 50	≤ 45
$\alpha_{\ell\ell}$ (°), α_{qq} (°)	≥ 120	≥ 120	≥ 130	≥ 130
$\ln Y_{34}$	$\geq -6.$	$\geq -6.$		
$m_{\ell\ell}$ (GeV)	≥ 70	–	≥ 70, ≤ 120	≥ 70, ≤ 120
m_{qq} (GeV)	≥ 70	–	≥ 70, ≤ 120	≥ 70, ≤ 120
$p_T^{\text{miss}}/E_{\text{vis}}$	≤ 0.1	–	–	–
p_Z^{miss} (GeV)	–	–	30	–
$p^{\text{miss}}/E_{\text{vis}}$	–	–	–	≤ 0.25
$p_Z^{\text{miss}}/p_T^{\text{miss}}$	–	–	–	≤ 3
$m_{\ell\ell}/m_{\ell\ell}^{\text{eq}}$, $m_{\text{qq}}/m_{\text{qq}}^{\text{eq}}$	–	–	≥ 0.8, ≤ 1.2	≥ 0.8, ≤ 1.2

Table D.1: *Selection cuts in the* ZZ $\to$ q$\bar{\text{q}}\ell^+\ell^-$ *channel at* $\sqrt{\text{s}} = 183$ GeV. *Here,* m_{vis} *is the visible mass of the event and* p^{miss} *the absolute value of the missing momentum vector. The variables* $m_{\ell\ell}^{\text{eq}}$ *and* $m_{\text{qq}}^{\text{eq}}$ *denote the invariant masses of the lepton-lepton and the jet-jet system, obtained from a kinematic fit imposing energy and momentum conservation and equal masses. The other abbreviations were explained in the main text.*

selection efficiencies, the background expectation and the number of observed candidates are summarised in Table D.2. The spectrum of the mass obtained from a kinematic fit,

imposing four-momentum conservation and equal masses of the lepton and the jet pair, is shown in Figure D.1. The result of the binned likelihood fit to this spectrum is also shown.

Selection of process $ZZ \to$	Efficiency (%) on $ZZ \to$ $q\bar{q}e^+e^-$	$q\bar{q}\mu^+\mu^-$	$q\bar{q}\tau^+\tau^-$	Expected Signal	Expected Background	Observed Data
$q\bar{q}e^+e^-$	78.9	0.0	0.2	0.79 ± 0.07	0.29 ± 0.04	2
$q\bar{q}\mu^+\mu^-$	0.0	57.5	0.5	0.42 ± 0.02	0.09 ± 0.01	0
$q\bar{q}\tau^+\tau^-$	4.4	8.8	30.4	0.26 ± 0.02	0.85 ± 0.13	0

Table D.2: *Efficiencies for the* $ZZ \to q\bar{q}\ell^+\ell^-$ *channel at* $\sqrt{s} = 183$ GeV. *The expected signal and background along with the number of observed candidates are also shown.*

The $ZZ \to q\bar{q}\ell^+\ell^-$ cross section is measured to be:

$$\sigma_{ZZ \to q\bar{q}\ell^+\ell^-} = 0.054^{+0.134}_{-0.034}\ (\text{stat}) \pm 0.002\ (\text{sys})\ \text{pb}.$$

The EXCALIBUR prediction of 0.043 pb is in agreement with this measurement. In combination with the other channels, the following cross section is obtained:

$$\sigma_{ZZ} = 0.30^{+0.22}_{-0.16}\ (\text{stat})\ ^{+0.07}_{-0.03}\ (\text{sys})\ \text{pb},$$

which agrees with SM value of 0.25 pb. At the 95% CL, one obtains 0.03 pb $< \sigma_{ZZ} <$ 0.79 pb.

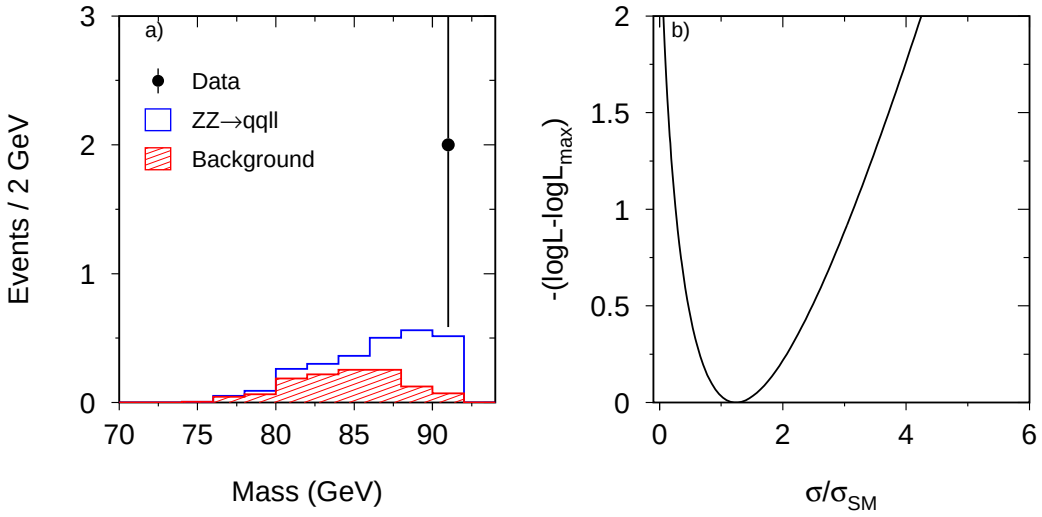

Figure D.1: *a) Final mass distribution in the* $ZZ \to q\bar{q}\ell^+\ell^-$ *channel at* $\sqrt{s} = 183$ GeV, *b) likelihood curve obtained by fitting the spectrum in a) as a function of the ratio of the measured to the predicted cross section.*

Appendix E

Selection of Reference Samples

The selection criteria for the reference samples used to evaluate systematic uncertainties are described in this chapter.

$e^+e^- \to e^+e^-$
Low multiplicity events are selected with less than 11 calorimetric clusters and a number of tracks between 1 and 4. Two calorimetric objects with an opening angle between them of more than 155° must have been detected. In the next step, di-muon events are antiselected by requiring the energy measured in the muon chambers to be smaller than 5 GeV. In order to suppress $e^+e^- \to \tau^+\tau^-$ and $WW \to \ell\nu\ell\nu$ events, the visible energy must be larger than $0.6\sqrt{s}$ and the energy of the objects must exceed 15 GeV.

$e^+e^- \to \mu^+\mu^-$
Events with less than 8 calorimetric clusters and a number of tracks between 1 and 4 are selected. At least two objects with an opening angle between them of more than 155° to each other are required. Events containing energy depositions in the electromagnetic calorimeter consistent with an electromagnetic shower shape are removed. The visible energy must exceed $0.4\sqrt{s}$, from which 5 GeV must be associated with the muon chambers. In order to suppress cosmic ray contamination, there must be at least one scintillator fired within in a time-of-flight corrected time window of 3.0 ns around the beam crossing. Furthermore at least one track in the TEC is required with not more than 5 mm distance of closest approach (DCA) to the beam axis.

$e^+e^- \to \tau^+\tau^-$
The process $e^+e^- \to \tau^+\tau^-$ is selected by limiting the number of clusters at maximum 11 and requiring the number of tracks to lie between 1 and 8. Events from $e^+e^- \to e^+e^-$ and $e^+e^- \to \mu^+\mu^-$ are rejected by requiring the energy of electrons and muons to be below $0.225\sqrt{s}$. The visible energy must be within $0.2\sqrt{s}$ and $0.8\sqrt{s}$. Two calorimetric energy depositions with an opening angle between them of 155° to each other are required. Cosmic ray contamination is suppressed in the same way as in the $e^+e^- \to \mu^+\mu^-$ selection.

Radiative $q\bar{q}(\gamma)$ Events:
This class of events is characterised by high multiplicity and a large longitudinal imbalance due to initial state photon, which escapes in most of the cases undetected through the beam pipe.
The events at $\sqrt{s} = 189$ GeV have been selected by requiring at least 5 tracks, 15 calorimetric clusters and a visible between $0.5\sqrt{s}$ and $0.9\sqrt{s}$. The missing momentum vector along the beam pipe must be at least 50 GeV but less than $0.7 \cdot E_{vis}$. The visible mass of the event is required to lie within 25 and 120 GeV. In order to suppress background from the two-photon process the direction of the event thrust must satisfy $| \cos\theta_{thrust} | \leq 0.95$, and there should be not more than 60 GeV energy deposited in the luminosity monitor.

Bibliography

[1] S. Weinberg, Phys. Rev. Lett. **19** (1967) 1264.

[2] The UA1 Collaboration, G. Arnison *et al.*, Phys. Lett. **B122** (1983) 103;
The UA1 Collaboration, G. Arnison *et al.*, Phys. Lett. **B126** (1983) 398.

[3] The Gargamelle Neutrino Collaboration, F. J. Hasert *et al.*, Phys. Lett. **B46** (1973) 138.

[4] P. W. Higgs, Phys. Lett. **12** (1964) 132, Phys. Rev. Lett. **13** (1964) 508 and Phys. Rev. **145** (1966) 1156;
F. Englert and R. Brout, Phys. Rev. Lett. **13** (1964) 321;
G.S. Guralnik *et* al, Phys. Rev. Lett. **13** (1964) 585.

[5] G. Kane, *Modern Elementary Particle Physics*, Addison-Wesley Publishing Company Inc., 1987.

[6] S. Dawson, J.F. Gunion, H.E. Haber and G.L. Kane, *The Physics of the Higgs Bosons: Higgs Hunter's Guide*, Addison Wesley, Menlo Park, 1989.

[7] S. Glashow and S. Weinberg, Phys. Rev. **D15** (1977) 1958.

[8] J. F. Gunion, H. E. Haber, Nucl. Phys. **B272** (1986) 1., erratum ibid. **B402** (1993) 567.

[9] S. Dawson, J.F. Gunion, H.E. Haber and G.L. Kane, *The Physics of the Higgs Bosons: Higgs Hunter's Guide*, Addison Wesley, Menlo Park, 1989, page 307 ff.

[10] H. E. Haber and M. Schmitt, *Supersymmetry*, in Review of Particle Physics, Eur. Phys. J. **C3** (1998) 743..

[11] S. P. Li and M. Sher, Phys. Lett. **B140** (1984) 339.

[12] E. Accomando *et al.*, in *Physics at LEP2*, ed. G. Altarelli, T. Sjöstrand and F. Zwirner, CERN 96-01.

[13] A. Djouadi, P. Janot, J. Kalinowski and P. M. Zerwas, Phys. Lett. **B376** (1996) 220.

[14] M. Carena, J. R. Espinosa, M. Quiros, C.E.M. Wagner, Phys. Lett. **B355** (1995) 209.

[15] M. Carena, M. Quiros, C.E.M. Wagner, Nucl. Phys. **B461** (1996) 407.

[16] G. Altarelli, T. Sjöstrand, F. Zwirner,*Physics at LEP2*, CERN 96-01, Vol. 1.

[17] P.H. Chankowski, S. Pokorski and J. Rosiek, Phys. Lett. **B274** (1992) 191.

[18] P. Janot, *The HZHA Generator* in G. Altarelli, T. Sjöstrand, F. Zwirner,*Physics at LEP2*, CERN 96-01, 1996, vol. 2, p.309.

[19] A. G, Akeroyd and W. J. Strirling, *Light Charged Higgs Scalars at High Energy* e^+e^- *Colliders*, Preprint University of Durham, **DTP/94/96**.

[20] S. Komamiya, Phys. Rev. **D38** (1988) 2158.

[21] L. Resnick, M.K. Sundaresan, P. J. S. Watson, Phys. Rev. **D8** (1973) 172.

[22] E. Braaten, J.P. Leveille, Phys. Rev. **D22** (1980) 715;
N.Sakai, Phys. Rev. **D22** (1980) 2220;
T. Inami, T. Kubota, Nucl. Phys. **B179** (1981) 171;
M. Drees, K. Hikasa, Phys. Lett. **B 240** (1990) 455;
S. G. Gorishny, A. L. Kataev, S. A. Larin, L. R. Surguladze, Mod. Phys. Lett. **5** (1990) 2703;
A. L. Kataev, V. T. Kim, Mod. Phys. Lett. **A9** (1994) 1309;
L. R. Surguladze, Phys. Lett. **B 341** (1994) 61.

[23] S. Narison, Phys. Lett. **B 341** (1994) 73.

[24] G. Alexander *et al.*, Z. Phys. **C73** (1997) 189.

[25] M. Veltmann, Acta Phys. Polon. **B8** (1977) 475;
B. W. Lee, C. Quigg and H. Thacker, Phys. Rev. **D16** (1977) 1519;
D. Dicus and V. Mathur, Phys. Rev. **D7** (1972) 3111.

[26] L. Maiani, G. Parisi and R. Petronzio, Nucl. Phys. **B136** (1978) 115;
R. Dashen and H. Neuberger, Phys. Rev. Lett. **50** (1983) 1897.

[27] U.M. Heller, M. Klomfass, H. Neuberger and P. Vranus, Nucl. Phys. **B405** (1993) 555;
J. Kuti, L. Lin and Y. Shen, Phys. Rev. Lett. **61** (1988) 678;
M. Gockeler, K. Jansen and T. Neuhaus, Phys. Lett. **B273** (1991) 450;
U. M. Heller, H. Neuberger and P. Vranas, Phys. Lett. **B283** (1992) 335.

[28] M. Lindner, M. Sher and H.W. Zaglauer, Phys. Lett. **B228** (1988) 139.

[29] A.D. Linde, JETP Lett. **23** (1976) 64;
S. Weinberg, Phys. Rev. Lett. **36** (1976) 294.

[30] M.J. Duncan, R. Phillipe and M. Sher, Phys. Lett. **153B** (1985) 165;
G. Altarelli and I. Isidori, Phys. Lett. **B337** (1994) 141;
J. A. Casas, J. R. Espinosa and M. Quiros, Phys. Lett. **B342** (1995) 171; Phys. Lett. **B382** (1996) 374.

[31] The LEP Electroweak Working Group, *A Combination of Preliminary Electroweak Measurements and Constraints on the Standard Model*, CERN-EP/99-15, 1999.

[32] S. Eidelmann, F. Jegerlehner, Z. Phys. **C67** (1995) 585.

[33] M. Davier, A. Höcker, Phys. Lett. **B419** (1998) 419.

[34] SLD Collaboration, K. Baird, *Measurements of $A_{\rm LR}$ and A_ℓ from SLD*, Talk Presented at ICHEP 98, Vancouver, B. C., Canada, 23-29 July, 1998.

[35] UA2 Collaboration, J. Alitti *et al.*, Phys. Lett. **B276** (1992) 354.

[36] CDF Collaboration, F. Abe *et al.*, Phys. Rev. Lett. **65** (1990) 2243;
CDF Collaboration, F. Abe *et al.*, Phys. Rev. **D43** (1991) 2070;
CDF Collaboration, F. Abe *et al.*, Phys. Rev. Lett. **75** (1995) 11;
CDF Collaboration, F. Abe *et al.*, Phys. Rev. **D52** (1995) 4784;
A. Gordan, Talk Presented at XXXIInd Rencontres de Moriond, Les Arcs, 16-22 March 1997.

[37] D0 Collaboration, S. Abachi *et al.*, Phys. Rev. Lett. **77** (1996) 3309;
K. Streets, Talk Presented at Hadron Collider Physics 97, Stony Brook.

[38] CDF Collaboration, W. Yao, *t Mass at CDF*, Talk Presented at ICHEP 98, Vancouver, B. C., Canada, 23-29 July,1998.

[39] D0 Collaboration, B. Abbott *et al.*, Phys. Rev. **D58** (1998) 052001.

[40] CCFR/NuTeV Collaboration, K. McFarland *et al.*, Eur. Phys. J. **C1** (1998) 509;
NuTeV Collaboration, K. McFarland, Talk Presented at the XXXIIIth Rencontres de Moriond, Les Arcs, France, 15-21 March, 1998, HEP-EX/9806013.

[41] Z. Szillasi, *Direct and Indirect SM Higgs Search at LEP*, Talk Presented at the International Europhysics Conference High Energy Physics 99, Tampere, Finland, 15-21 July 1999.

[42] M. S. Alam *et al.*, Phys. Rev. Lett. **74** (1995) 2885.

[43] S. Bertolini *et al.*, Nucl. Phys. **B294** (1987) 321;
S. Bertolini *et al.*, Nucl. Phys. **B353** (1991) 591;
Y. Okada, Phys. Lett. **B315** (1993) 119.

[44] P. Bock *et al.*, *LEP Higgs Boson Searches Working Group*, CERN-EP/98-46.

[45] The ALEPH Collaboration, Phys. Lett. **B412** (1997) 173.

[46] The Delphi Collaboration, Eur. Phys. J. **C2** (1998) 1.

[47] The OPAL Collaboration, Eur. Phys. J. **C5** (1998) 19.

[48] The L3 Collaboration, Phys. Lett. **B294** (1992) 457.

[49] J.A. Valls for the CDF Collaboration, *Higgs Searches at the TEVATRON in RUN I*, Proceedings Internation Europhysics Conference on High Energy Physics, Tampere, Finland, July 15-21, 1999.

[50] The ALEPH Collaboration, Phys. Lett. **B418** (1998) 419.

[51] The OPAL Collaboration, Phys. Lett. **B426** (1998) 180.

[52] The CDF Collaboration, Phys. Rev. Lett. **79** (1997) 357 ;
The D0 Collaboration, Phys. Rev. Lett. **82** 4975;
Brendan Bevensee, *Top to Charged Higgs Decays and Top Properties at the TEVATRON*, FERMILAB-CONF-98-155-E.

[53] The ALEPH Collaboration, Nucl. Instr. Meth. **A 294** (1990) 121.

[54] The DELPHI Collaboration, Nucl. Instr. Meth. **A 303** (1991) 233.

[55] L3 Collaboration, B. Adeva *et al.*, Nucl. Instr. Meth. **A289** (1990) 35.

[56] J.A. Bakken *et al.*, Nucl. Instr. Meth. **A275** (1989) 81.

[57] O. Adriani *et al,*, Nucl. Instr. Meth. **A302** (1991) 53.

[58] B. Adeva *et al.*, Nucl. Instr. Meth. **A323** (1992) 109;
S. Lanzano, *et al.*, Nucl. Instr. Meth. **A289** (1990) 335.

[59] K. Deiters *et al.*, Nucl.Instr.Meth. **A323** (1992) 162.

[60] M. Chemarin *et al.*, Nucl.Instr.Meth. **A349** (1994) 345.

[61] B. Acciari *et al.*, Nucl.Instr.Meth. **A351** (1994) 300.

[62] G. Basti *et al.*, Nucl.Instr.Meth. **A374** (1996) 293.

[63] I.C. Brock *et al.*, Nucl. Instr. Meth. **A381** (1996) 236.

[64] U. Uwer, *The L3 Scintillation Counter System: Description and Status*, L3 Internal Note 2003, 1996.

[65] A. Adam *et al.*, Nucl.Instr.Meth. **A383** (1996) 342.

[66] The OPAL Collaboration, Nucl. Instr. Meth. **A 305** (1991) 275.

[67] A. Adam *et al.*, Nucl. Instr. Meth. **A344** (1994) 521.

[68] A. Kopp, *Aufbau und Test der elektronischen Auslese der L3 Z-Kammer im Bunch-Train-Regime von LEP*, Diplomarbeit, Humboldt-Universität zu Berlin, 1995.

[69] The L3 Collaboration, Phys. Rep. **236** (1993).

[70] W. Lustermann, *Das anomale magnetische Moment des τ Leptons*, Ph.D. Thesis, ETH Zürich (1996), DISS. ETH Nr. 11645.

[71] I. Brock *et al.*, Nucl. Inst. Meth. **A381** (1996) 236.

[72] The LEP Energy Working Group Collaboration, A. Blondel *et al.*, *Evaluation of the LEP Centre-of-Mass Energy above the W-pair Production Threshold*, Preprint CERN-EP/98-191, CERN-SL/98-073, CERN 1998, Submitted to Eur. Phys. J. C.;
The LEP Energy Working Group Collaboration, *Energies for LEP1.5 Run*, Preprint LEP ECAL/97-04, LEP ECAL, 1997;
The LEP Energy Working Group Collaboration, *Preliminary LEP Energy Calibration for 1997 Data*, Preprint LEP ECAL/98-01, LEP ECAL, 1998;
The LEP Energy Working Group Collaboration, *Evaluation of the LEP Centre-of-Mass Energy for Data Taken in 1998*, Preprint LEP ECAL/99-01, LEP ECAL, 1999.

[73] T. Sjöstrand, CERN-TH 7112/93, CERN (1993), revised August 1995;
T. Sjöstrand, Comp. Phys. Comm. **82** (1994) 74.

[74] M. Skrzypek *et al.*, Comp. Phys. Comm. **94** (1996) 216;
M. Skrzypek *et al.*, Phys. Lett. **B372** (1996) 289.

[75] R. Kleiss and R. Pittau, Comp. Phys. Comm. **83** (1994) 141;
see also F.A. Berends, R. Kleiss and R. Pittau in "Physics at LEP2", CERN 96-01, Vol. 2, eds. G. Altarelli, T. Sjöstrand and F. Zwirner.

[76] R. Engel, Z. Phys. **C 66** (1995) 203;
R. Engel and J. Ranft, Phys. Rev. **D 54** (1996) 4244.

[77] The L3 Detector Simulation is Based on GEANT Version 3.15.
See R. Brun *et al.*, "GEANT 3", CERN DD/EE/84-1 (Revised), September 1987.
The GHEISHA Program (H. Fesefeldt, RWTH Aachen Report PITHA 85/02 (1985)) is Used to Simulate Hadronic Interactions.

[78] O. Adriani *et al.*, Nucl. Instr. Meth. **A302** (1991) 53.

[79] C.Caso *et al.*, *Review of Particle Physics*, The Eur. Phys. J. **C3** (1998) 1.

[80] A. Dominguez, *Search for Neutral Higgs Bosons in e^+e^- Interactions at Center-of-Mass Energies between 130 GeV and 183 GeV*, Ph.D. Thesis, UCSD, 1998, http://hep.ucsd.edu/thesis/aaron.html.

[81] J. Branson, A. Dominguez, I. Fisk and G. Raven, *The UCSD B Tag for 1996*, L3 Internal Note 2108, 1997.

[82] L. Lönnblad, C. Peterson and T. Rognvaldsson, Nucl. Phys. **B349** (1991) 675;
C. Peterson *et al.*, Comp. Phys. Comm. **81** (1994) 185.

[83] O. Adriani *et al.*, Phys. Lett. **B307** (1993) 237.

[84] S. Bethke *et al.*, Nucl. Phys. **B 370** (1992) 310.

[85] N. J. Kjaer and R. Moller, *Reconstruction of Invariant Masses in Multi-Jet Events*, DELPHI Internal Note 91-17,1991.

[86] OPAL Collaboration, K. Ackerstaff *et al.*, Eur. Phys. J. **C1** (1998) 425.

[87] B. A. Kniehl, Phys. Rep. **C240** (1994) 211;
E. Gross, B. A. Kniehl and G. Wolf, Z. Phys. **C63** (1994) 417, erratum-ibid **C66** (1995) 321.

[88] A. Djouadi *et al.*, Z. Phys. **C70** (1996) 427.

[89] L3 Collaboration, M. Acciari *et al.*, Phys. Lett. **B431** (1998) 437.

[90] L3 Collaboration, M. Acciari *et al.*, Phys. Lett. **B461** (1999) 376.

[91] L3 Collaboration, M. Acciari *et al.*, Phys. Lett. **B436** (1998) 389.

[92] L3 Collaboration, M. Acciari *et al.*, *Search for Neutral Higgs Bosons of the Minimal Supersymmetric Model in* e^+e^- *Interactions at* $\sqrt{s} = 189$ GeV, L3 preprint 192, Submitted to Phys. Lett. **B**.

[93] L3 Collaboration, M. Acciari *et al.*, Phys. Lett. **B446** (1999) 368.

[94] L3 Collaboration, M. Acciari *et al.*, *Search for Charged Higgs Bosons in* e^+e^- *Collisions at* $\sqrt{s} = 189$ GeV, CERN-EP/99-120, Accepted by Phys. Lett. **B** (1999).

[95] L3 Collaboration, M. Acciari *et al.*, Phys.Lett. **B411** (1997) 373.

[96] A. Favara, M. Pieri, *Confidence Level Estimation and Analysis Optimisation*, Preprint DFF-278-4-1997, INFN, 1997.

[97] A. Dominguez, Presentation in the L3 Higgs Working Group, 1999.

[98] S. Heinemeyer, W. Hollik and G. Weiglein, Phys. Lett. **B440** (1998) 296.

[99] L3 Collaboration, M. Acciari *et al.*, *Study of Z Boson Pair Production in* e^+e^- *Collisions at LEP* $\sqrt{s} = 189$ GeV, CERN-EP/99-119, Accepted by Phys. Lett. **B**.

[100] L3 Collaboration, M. Acciari *et al.*, Phys. Lett. **B450** (1999) 281.

[101] J. Fujimoto *et al.*, Comp. Phys. Comm. **100** (1997) 128.

[102] The LEP Working Group for Higgs Boson Searches, *Searches for Higgs Bosons: Preliminary Combined Results from the four LEP Experiments at* $\sqrt{s} \approx 189$ GeV, ALEPH 99-081 CONF 99-052, DELPHI 99-142 CONF 327, L3 Note 2442, OPAL Technical Note TN-614 (1999).

[103] ALEPH Collaboration, *Search for the Neutral Higgs Bosons of the Standard Model and the MSSM in* e^+e^- *Collisions at* $\sqrt{s} = 188.6$ GeV, Contribution to the 1999 Summer Conferences, ALEPH 99-053 CONF 99-029 (1999);
ALEPH Collaboration, *Search for Charged Higgs Bosons in* e^+e^- *Collisions at* $\sqrt{s} = 189$ GeV, Contribution to the 1999 Summer Conferences, ALEPH 99-070 CONF 99-044 (1999);
DELPHI Collaboration, *Search for Neutral Higgs Bosons in* e^+e^- *Collisions at* $\sqrt{s} = 188.7$ GeV, Contribution to the HEP'99 Conference in Tampere, Finland, DELPHI 99-86 CONF 273 (1999);
DELPHI Collaboration, *Search for Charged Higgs Bosons*, Contribution to the HEP'99 Conference in Tampere, Finland, DELPHI 99-92 CONF 279 (1999);
OPAL Collaboration, *Search for Neutral Higgs Bosons in* e^+e^- *Collisions at* $\sqrt{s} \approx 189$ GeV, CERN-EP/99-096, Submitted to Eur. Phys. J. **C** (1999);
OPAL Collaboration, *Search for Charged Higgs Bosons in* e^+e^- *collisions at* $\sqrt{s} = 189$ GeV, Contribution to the 1999 Summer Conferences, OPAL-PN/99-373 (1999).

[104] P. Janot, *Higgs Searches: Present and Future*, Talk Presented at the XIth Rencontres de Blois, June 27 - July 3, 1999.

[105] John S. Conway, *Higgs Searches in Run II at the Tevatron*, Published Proceedings of the 13th Les Recontres de Physique de al Valle D'Aosta: Results and Perspectives in Particle Physics, La Thuile, Valle d'Aoste, Italy, February 28–March 6, 1999.

[106] R. Brinkmann, G. Materlik, J. Rossbach, A. Wagner, *Conceptual Design Report of a 500 GeV* e^+e^- *Linear Collider with Integrated X-Ray Laser Facility*, DESY 1997-048.

Acknowledgements

First of all, I wish to thank my advisors Wolfgang Lohmann and Thomas Hebbeker for their continuous support and guidance throughout the last three years.
I enjoyed the work in the Higgs group and profited a lot from fruitful discussions with Andrei Kounine, Aaron Dominguez and Ian Fisk.
My friendship to Ho Jong Lee, Peter Molnár and Daniel Ruschmeier has proven to be extremely valuable in tackling many difficult problems.
I am grateful to Ia Iashvili, who patiently explained me the complicated SUSY world.
I would like to thank Prof. S.C.C. Ting for sharing his wisdom on performing and presenting physics analysis with the L3 community. The impressive demonstration of his ability to distinguish between important and less important problems helped me to develop an efficient working style.
A thesis in experimental high energy physics is not possible without the combined effort of many people. I am grateful to the numerous technicians, engineers and physicists who have built and maintained LEP and the L3 detector. I acknowledge the effort of all shift takers and experts on call who ensured data taking and I thank all those people who have made these data usable by calibrating the detector, writing reconstruction code, producing Monte Carlos and and and ...
A special thank you goes to Chris Tully for the careful reading of the manuscript. He considerably improved my English.
Finally, I would like to thank all members of the L3 groups in Zeuthen and Berlin for providing a very pleasant working atmosphere. I remember with joy the numerous social evenings that we spent together with all those unique moments that will make the time at CERN unforgettable.

Hiermit erkläre ich, daß ich diese Arbeit selbständig verfaßt und keine anderen als die angegebenen Quellen und Hilfsmittel benutzt habe.